Magnetohydrodynamic duct flow
in the presence of a magnetic dipole

Dissertation

zur Erlangung des akademischen Grades

Doktoringenieur

(Dr.-Ing.)

vorgelegt der

Fakultät für Maschinenbau der

Technischen Universität Ilmenau

von Frau

Dipl.-Math. Saskia Tympel

(geb. Aßmann)

geboren am 02.07.1983 in Berlin/Deutschland

Zusammenfassung

Die effiziente Verarbeitung von aggressiven flüssigen Werkstoffen, wie Aluminium oder Kupfer, erfordert häufig die Kenntnis von Durchflussraten und der räumlichen Verteilung des Geschwindigkeitsfeldes. Es ist das erklärte Ziel der lokalen Lorentzkraftanemometrie derartiges zu leisten. Dabei wird an einem kleinen Magneten die Lorentzkraft, die durch das in der Nähe fließende Metall induziert wird, gemessen. Jedoch nimmt diese Kraft auch auf das Fluid Einfluss und verformt das Strömungsprofil.

Von welcher Art diese Verformung ist und ob diese die messbare Kraft verändert, wurde in der vorliegenden Arbeit mittels analytischer und numerischer Methoden untersucht. Als Magnetfeld wird die einfachste räumlich variable Konfiguration gewählt, ein magnetisches Dipolfeld.

Dazu werden die magnetohydrodynamischen Gleichungen in quasistatischer Näherung, d. h. für kleine magnetische Reynoldszahlen, mittels direkter numerischer Simulation untersucht. Zwei dimensionslose Kennzahlen sind hierbei maßgebend: die Hartmannzahl Ha und die Reynoldszahl Re. Zusätzlich spielen der Abstand des Dipols zur Flüssigkeitsoberfläche und die Orientierung des magnetischen Moments eine Rolle.

Die Abhängigkeit der messbaren Lorentzkraft vom Abstand h wird durch zwei Potenzgesetze bestimmt. Für sehr kleine Abstände ist die Kraft proportional zu h^{-2}, für sehr große Abstände zu h^{-7}. Die Deformation des Strömungsprofils verursacht eine Auftriebskraft, proportional zu Ha^4, während die messbare Zugkraft sich wie Ha^2 verhält. Die Art der Verformung hängt von der Orientierung des magnetische Moments ab und kann in Regionen von Rückströmungen, also Wirbeln, und lokalen Hartmannschichten, also beschleunigter Strömung, unterteilt werden. Die Strömung bleibt zeitunabhängig für niedrige Reynoldszahlen. Für $Re \geq 2000$ wurden periodische Wirbelablösungen gefunden, falls $Ha > 80$ und der Abstand $h = 1.6$ ist sowie das Dipolmoment in Spannweitenrichtung zeigt.

Der untersuchte Parameterraum überschreitet zwar den im Laborexperiment erreichbaren, lieferte jedoch trotzdem nützliche Hinweise für die Auswertung der Messergebnisse. In der vorliegenden Studie wurden erstmalig die Einflussparameter für eine dreidimensionale Strömung unter Einwirkung eines inhomogenen, lokalen Magnetfelds untersucht. Die Untersuchungen bieten interessante Perspektiven für die Strömungsbeeinflussung und folglich auch für die Strömungskontrolle.

Abstract

In industrial applications, it is often required to measure the flow properties of hot and aggressive liquid metals such as aluminum and copper. Besides the flow rate, the spatial distribution of the velocity is of interest. Local Lorentz force velocimetry aims to resolve the spatial distribution of the flow by measuring Lorentz forces at a small permanent magnet brought into the vicinity of the liquid. In addition, these forces acts on the fluid and may deflect the flow.

The question, on the nature of this deflection and its impact on the measured forces, will be answered in the present work by means of analytical and numerical methods. The small magnet is modeled by a magnetic point dipole that acts on the laminar flow inside a square duct with insulating walls.

Direct numerical simulations are used to solve the magnetohydrodynamic equations in the quasi-static approximation for low magnetic Reynolds numbers. The system depends on two non-dimensional parameters: the Hartmann number Ha and the Reynolds number Re. Additional influence is given by the geometry, e. g. the distance of the dipole to the surface of the liquid h and the orientation of the magnetic moment of the dipole. These influences are investigated in detailed parameter studies.

Two power laws are found for the dependency of the total Lorentz force on the distance. For small distances the drag force is proportional to h^{-2} and for large distances to h^{-7}, respectively. This force is proportional to Ha^2. The deflection of the flow gives rise to a lift force that depends on Ha^4. The shape of the deflection depends on the orientation. Regions of reversed flow and local Hartmann layers are created. For low Reynolds numbers the flow stays laminar, while for $Re \geq 2000$ vortex shedding is observed for the spanwise oriented dipole if $Ha > 80$ and $h = 1.6$.

The parameter range considered here exceeds the range, that can be exploited by recent laboratory experiments. Nevertheless, the investigations may provide useful hint for the evaluation of the measured forces. The present study provides for the first time a detailed parameter study for three-dimensional flow under the influence of an inhomogeneous localized magnetic field. It opens new perspectives for the flow manipulation and thus also for flow control.

Contents

Vectors and scalars

$\boldsymbol{x} = (x, y, z)$ coordinates
$\boldsymbol{u} = (u_x, u_y, u_z)$ velocity field
$\boldsymbol{B} = (B_x, B_y, B_z)$ magnetic flux density
$\boldsymbol{m} = (k_x, k_y, k_z)$ magnetic moment
$\boldsymbol{j} = (j_x, j_y, j_z)$ electric currents
$\boldsymbol{f} = (f_x, f_y, f_z)$ Lorentz force density
$\boldsymbol{F} = (F_x, F_y, F_z)$ total Lorentz force
$\boldsymbol{T} = (T_x, T_y, T_z)$ torque
$\boldsymbol{\omega} = \nabla \times \boldsymbol{u}$ vorticity
φ electric potential
Ω enstrophy
$< \Delta u >$ deformation parameter

Material properties

symbol	meaning	characteristic value in laboratory experiments
ρ	density	6363.13 kg m^{-3}
σ	conductivity	$3.3 \cdot 10^6$ S m^{-1}
L	characteristic length, i. e. half of the duct width	0.025 m
h	distance from the dipole to the surface of the fluid	$\geq$0.01 m (based on the center of the magnet)
$\overline{u}$	mean velocity	$\leq$0.130174 m s^{-1}
B_{max}	maximal magnetic flux density inside the fluid	0.147 T
ν	kinematic viscosity	$3.4 \cdot 10^{-7}$ m^2 s^{-1}

Non-dimensional parameters

symbol	meaning	typical range in numerical study
$Re = \frac{\overline{u}L}{\nu}$	Reynolds number	$0.1 \ldots 3000$
$Ha = B_{max} L \sqrt{\frac{\sigma}{\rho\nu}}$	Hartmann number	$0 \ldots 130$
$N = \frac{Ha^2}{Re}$	interaction parameter	$1 \ldots 1000$
$Rm = \mu_0 \sigma \overline{u} L$	magnetic Reynolds number	≤ 0.015

1. Introduction

This chapter introduces the background of magnetohydrodynamic duct flow in the presence of a magnetic point dipole. Section 1.1 highlights some applications of magnetohydrodynamics and classifies this work. Then follows in section 1.2 with a review of selected works on magnetohydrodynamic duct flow that range from homogeneous and inhomogeneous magnetic fields to localized magnetic fields. The flow measurement technique that takes advantage of these physical principles – Lorentz force velocimetry – is explained in section 1.3. Finally, the scope of the thesis is presented in section 1.4.

1.1. Applications of Magnetohydrodynamics

Magnetohydrodynamics (MHD) studies the interaction of electromagnetic fields with electrically conducting fluids. The term "magnetohydrodynamics" was first recorded by Hannes Alfvén in 1945 in the context of the cosmogony of the solar system (Alfvén, 1946). In astrophysics, the considered fluid is plasma – ionized gas. The ionization is ignored in MHD calculations, which is leading to statements as "MHD is the poor cousin of plasma physics" (Schnack, 2009). Nevertheless, as the same author acknowledges, "MHD seems to work", and it plays a central role in several physical phenomena such as the dynamics in the interior and atmosphere of stars (Biskamp, 1993; Rüdiger & Hollerbach, 2004) or in nuclear fusion (Niu, 1989). In a nutshell, MHD breaks down when electron and ionic components have to be considered separately, i. e., when the different Larmor radii become essential.

The scope of applications of magnetohydrodynamics is much broader and not limited to plasma physics. In industrial applications, MHD leaves its role as the "poor cousin" and becomes the "rich uncle" of metallurgy. Magnetohydrodynamic shear flows are encountered in industrial applications involving molten metals, such as in metal processing or in the blanket of future nuclear fusion reactors (Knaepen & Moreau, 2008). MHD is also exploited in multiphysics problems, where electromagnetic forces are used to control solidification, e. g. in crystal growth (Langlois, 1985; Kirkpatrick, 1975; Lantzsch *et al.*, 2007).

Although the range of applications is wide, the underlying physical principles are the same. A key parameter, that enables to distinguish between astrophysical and metallurgical applications, is the magnetic Reynolds number. This dimensionless quantity describes the ratio of advection to diffusion of the magnetic field (Davidson, 2006; Moreau, 1990). In astrophysical applications, the magnetic Reynolds number is large, i. e. of the order 10^3 to 10^4, such that the magnetic field is almost frozen in the flow. In contrast, metallurgic applications involve magnetic Reynolds numbers between 10^{-2} and 10^{-4}. This work is

dedicated to liquid metal flow in industrial applications (Davidson, 1999), with negligible magnetic Reynolds numbers.

In this range of metallurgy, many applications are available. They are all based on use of the Lorentz force that is induced due to Lenz rule. An oscillating Lorentz force can damp the perturbations in the boundary layer of the flow over a flat plate , e. g. Tollmien-Schlichting waves (Albrecht *et al.*, 2006, 2008; Shatrov & Gerbeth, 2006). Besides damping, the Lorentz force may also accelerate the fluid. This is used for induction pumps (Khripchenko *et al.*, 2010), where an alternating magnetic field directed normally to the plane of a channel give rise to the pumping effect.

An open problem can be found in casting (Schrewe, 1989; Beddoes & Bibby, 1999), where it is desirable to control the mass flow of the liquid metals. Furthermore, it is interesting to measure the spatial velocity distribution, e. g. the velocity field in the mold during the continuous casting of steel (Timmel *et al.*, 2010; Thomas & Chaudhary, 2009). Here, the aim is to improve the quality and cleanness of the the steel (Zhang & Thomas, 2003). Although there exists a variety of methods for flow measurement in liquids and gases at room temperature or slightly above it (Baker, 2004; Nitsche & Brunn, 2006), the possibilities to measure velocities in hot, opaque and aggressive liquids like aluminum or copper melts are limited. Being in direct contact with the material, standard sensors are rapidly destroyed due to heat and chemical reactions, while contactless optical measurement systems fail due to the opaqueness.

Several efforts of the last decade aimed at overcoming this limitation, such as the magnetic induction tomography (Korjenevsky *et al.*, 2000; Stefani *et al.*, 2004) and the Lorentz Force Velocimetry (LFV) (Thess *et al.*, 2006), which provide contactless methods to measure flow velocities in melts. The two methods follow a similar approach, but induction tomography uses an oscillating magnetic field and LFV takes advantage of permanent magnets. The present state-of-the-art is however still limited to the measurement of mean velocities or volumes fluxes of the liquid metal flow. Nevertheless, it is was already possible to distinguish the different flow regimes and to detect individual bubbles with induction tomography (Terzija *et al.*, 2011). This was done in a laboratory experiment that simulates the continuous casting process. Measurements in industrial environment by Kolesnikov *et al.* (2011) demonstrate the feasibility of measuring the flow rate with LFV for open channels. Recent works investigate *local LFV* in laboratory experiments (Pulugundla *et al.*, submitted) and (Heinicke *et al.*, 2012) with the aim to resolve the spacial properties of the flow. The present work continues these studies.

1.2. Review of selected research

Early works on MHD studied the Hartmann flow, a laminar flow in a duct under a uniform magnetic field (Hartmann, 1937; Hartmann & Lazarus, 1937). The magnetic field induces electric currents in the flow. These currents form closed loops in the fluid and lead to the Lorentz force. Due to Faraday's law of induction the Lorentz force is created that deflects
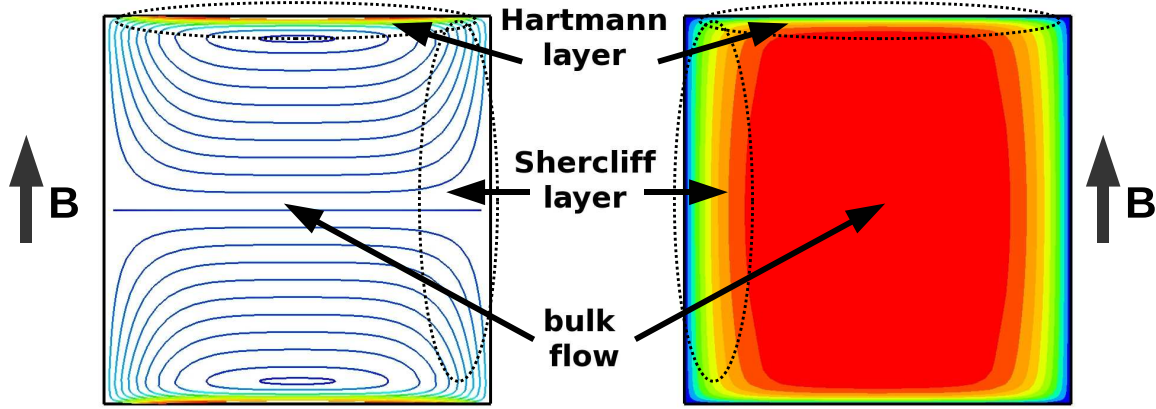
Figure 1.1.: Sketch of principle for the Hartmann flow with streamlines of electric currents (left) and velocity profile (right). Data obtained by DNS with $Re = 1000$ and $Ha = 30$.

the flow. For laminar flow, this velocity profile is known analytically (Müller & Bühler, 2001). In the turbulent case, the secondary mean flow was investigated for hydrodynamic duct flow, e. g. by Huser & Biringen (1993) and Uhlmann *et al.* (2007), and for the turbulent Hartmann flow in ducts by Shatrov & Gerbeth (2010).

The velocity profile of the Hartmann flow (cf. figure 1.1) is divided into three parts: The bulk region, the Hartmann and Shercliff layers (Hunt & Shercliff, 1971; Hunt, 1965). In the bulk flow, the velocity profile is flattened due to braking Lorentz forces. The velocity boundary layer with a magnetic field perpendicular to the wall is called the Hartmann layer. This layer has the key property that viscous friction and electromagnetic forces balance each other. Here, the fluid is accelerated due to the electromagnetic forces. The thickness of the Hartmann layer is proportional to the inverse of the Hartmann number Ha (Müller & Bühler, 2001). The Hartmann number is defined by the ratio of electromagnetic to viscous forces and is a measure for how strong the fluid flow is changed by the magnetic field. In laboratory experiments, Ha is in the range of 10 to 10^3, while in the blanket of fusion reactors it is even higher, i. e. 10^3 to 10^4 (Knaepen & Moreau, 2008). The presented work focuses on Hartmann numbers of order 10^2, which is the same range as in laboratory experiments by Heinicke (2012) that are used for the validation in section 3.3. The Shercliff layers are the side layer with a magnetic field parallel to the wall. They are less stable than the bulk and the Hartmann layers. Krasnov *et al.* (2010) computed optimal perturbations to a laminar state for a transverse uniform magnetic field in a duct with insulating walls. The stability of the Hartmann layer was a subject of several investigations (Lingwood & Alboussiere, 1999; Gerard-Varet, 2002; Moresco & Alboussiere, 2003; Kobayashi, 2008).

If the walls of the duct are conducting, a stronger damped profile of the velocity is observed (Hunt & Shercliff, 1971; Hunt & Stewartson, 1965; Kinet *et al.*, 2009). Spatial variations in the conductivity give rise to vortices and deformations of the flow (Hunt, 1966). Works

by Alpher *et al.* (1960) and Bühler (1996) describe the creation of internal shear layers by non-uniform electrical boundary conditions at the channel walls. To reduce complexity, we restrict the investigations in this work to insulating walls.

Further investigations involve variation of the geometry. A duct whose width increases linearly in the flow direction was investigated by Walker *et al.* (1972) and Walker & Picologlou (1995). Three-dimensional flow in sudden expansion has been investigated numerically for both the hydrodynamic (Mistrangelo, 2011*a*) and the magnetohydrodynamic case (Mistrangelo, 2005, 2011*b*). Experimental investigations correlated to the application in fusion reactors were performed by Bühler *et al.* (2007). On the contrary, it is the aim of this work to understand the fundamentals of the Lorentz force velocimetry (cf. section 1.3), we consider a square duct as a basic geometry.

As we keep the geometry fixed, the focus is on the variation of the shape of the magnetic field. The first step is to study the fringing magnetic field – a model in which the fluid enters the field of a huge permanent magnet. Sterl (1990) investigates the redistribution of the fluid in the region where the magnetic field changes. Large axial currents are induced leading to the "M-shaped" velocity profile, which are characteristic for MHD flows in inhomogeneous magnetic fields.

Besides the fringing magnetic fields, recent research considered the so-called magnetic obstacles. This term is originated in the fact that a localized magnetic field influences the fluid in a similar way as a solid obstacle. The basic effects of this interaction were shown by Shercliff (1965) in an educational film. In this experiment, a magnet system was moved along an open channel filled with mercury. The movement led to creation of vortices in the liquid. Some early experiments and numerical investigations were done for two-dimensional creeping flow by Gelfgat & Olshanskii (1978) and Gelfgat *et al.* (1978). UDV measurements[1] in channel flow, performed by Andreev *et al.* (2006), show that the incoming flow transforms into an M-shaped profile, in the region were the magnetic field is strongest. The flow is further characterized by large-scale vortical structures downstream of the magnetic field. A detailed study of the vortex structures in the liquid is given by Votyakov *et al.* (2007). These numerical results were recently validated by Kenjeres *et al.* (2010) and ten Cate (2009). A numerical study on the influence of the size of the magnet on the flow distribution is given in Votyakov *et al.* (2008) for three-dimensional stationary flow. The number of attached vortices decrease with decreasing magnetic size. The case of quasi two-dimensional time-dependent flow is studied in Cuevas *et al.* (2006*b*). Here, the magnetic field induces a vortex shedding similar to the von Karman vortex street behind a solid cylinder. It is possible to give analytic solutions for the two-dimensional creeping flow (Cuevas *et al.*, 2006*a*), when the permanent magnet is approximated with a magnetic point dipole.

In general, it is impossible to find an analytical solution for the electromagnetic force acting on the fluid, even when the motion of the conducting liquid is very simple as for the laminar flow. Only a few cases which replace the real magnet system by a magnetic dipole

---

[1]UDV = Ultrasonic Doppler Velocimetry.

or simple coil are known to have analytical solutions (Reitz, 1970; Palmer, 2004; Thess *et al.*, 2007; Priede *et al.*, 2009, 2011*b*). These simplified problems are of great importance for the theory of Lorentz force velocimetry because they allow a deeper understanding of the involved processes and provide reference data for complex numerical simulations.

1.3. Lorentz force velocimetry

Lorentz force velocimetry (LFV) is a contactless technique for measuring flow rates and velocities of moving conducting liquids (Thess *et al.*, 2006, 2007). It can be used in situations where mechanical contact of a sensor with the flowing medium must be avoided due to environmental conditions (high temperatures, radioactivity) and chemical reactions. Possible applications include flow measurement during the continuous casting of steel (Schrewe, 1989), in ducts and open channel flows of liquid aluminum alloys in aluminum production (Kolesnikov *et al.*, 2011), and in other metallurgical processes where hot liquid metal or glass flows are involved (Davidson, 1999).

Besides LFV, other techniques exist for flow rate measurements in opaque conducting liquids (Argyropoulos, 2000). However, none of the known techniques have found commercial application in metallurgy. Invasive probes, such as the Vives probe (Ricou & Vives, 1982) or mechanical reaction probes (Szekely *et al.*, 1977), are not very suitable for flow rate measurements at high temperatures because they require direct contact between the sensor and the often aggressive liquid metal. Ultrasound sensors (Takeda, 1987) have similar problems, but can be used for hot melts with temperatures up to 800°C (Eckert *et al.*, 2003). Commercially available electromagnetic flowmeters (Shercliff, 1962; Bevir, 1970) are often not usable either, since rough operating conditions are typical for metallurgical applications. Inductive flow tomography (Stefani *et al.*, 2004) can be used sometimes for reconstruction of the melt flow structure in closed ducts. This technique, however, is too complex to be applied for simple flow metering and requires solution of inverse problems. So its adaption to industrial processes seems to be overly complicated.

LFV belongs to the group of electromagnetic flow measurement methods (Shercliff, 1962). Let us briefly review these techniques before defining the problem to be considered in the present work. In all methods, the flow of an electrically conducting fluid is exposed to a magnetic field leading to a Lorentz force that deflects the paths of the charge carriers inside the fluid, where the magnitude of the resulting eddy currents depends on the fluid velocity. The first to use this effect was Michael Faraday, when he attempted to determine the velocity of the river Thames flowing through Earth's magnetic field by measuring the induced voltage in two electrodes placed on either side of the river (Faraday, 1832). The first successful implementation of an inductive flowmeter was then done by Wollaston in 1851 (Wollaston, 1881).
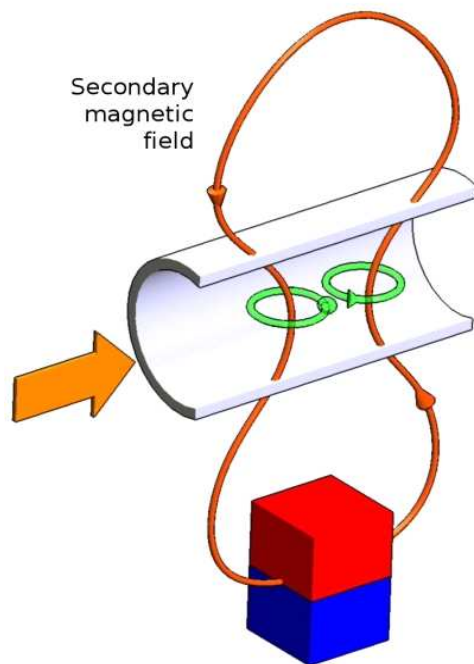
A slightly different method is used in the eddy current flowmeter as proposed by Feng *et al.* (1975). It consists of a system of driver and pickup coils that induce and detect eddy currents, respectively. By applying an AC magnetic field, a phase-shift flowmeter can
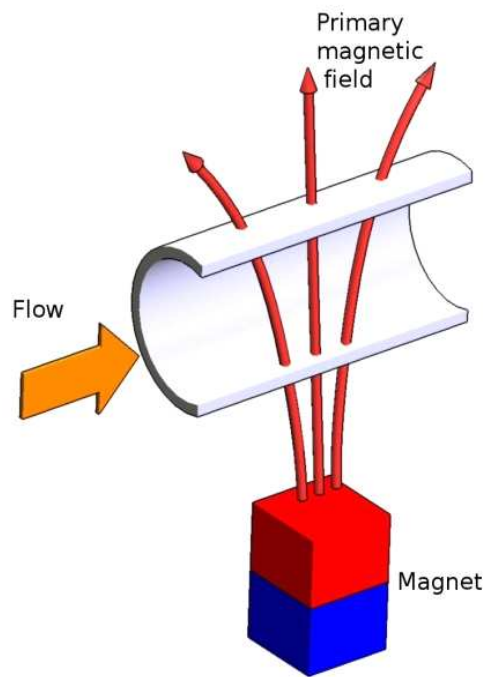
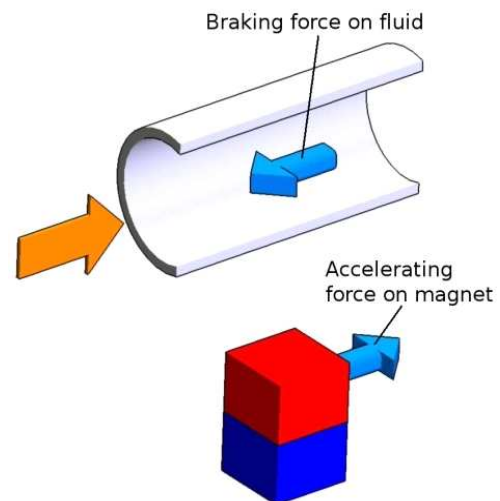(a) A permanent magnet is brought close to the conduit.
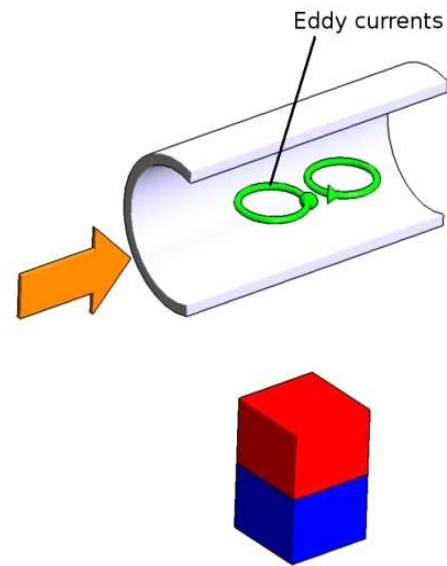
(b) Eddy currents are induced in the conducting liquid.

(c) The eddy currents induce a weak secondary magnetic field.

(d) The resulting Lorentz force brakes the fluid and its counter force can be measured at the magnet.

Figure 1.2.: Principle of Lorentz force velocimetry. Courtesy to the Institute of Thermodynamics and Fluid Mechanics of TU Ilmenau.

measure velocities via phase disturbances in the surrounding electromagnetic field that are caused by the flow field (Priede *et al.*, 2011*a*). A step towards spatial resolution in a bulk flow is represented by the contactless inductive flow tomography (Baumgartl *et al.*, 1993; Stefani *et al.*, 2004). This method exposes a melt to a weak magnetic field and then reconstructs the velocity field from the secondary magnetic field outside the melt. Closely related to LFV are the rotary flowmeters that have the advantage of being independent of the electrical conductivity and thus of the temperature of the melt. These flowmeters employ permanent magnets which are set in rotation by the torque generated by the interaction of the magnetic field with the moving fluid (Bucenieks, 2000; Thess *et al.*, 2006; Priede *et al.*, 2009). In addition to the torque, there acts an accelerating force on the magnet system which is the counterpart of the braking Lorentz force inside the fluid.

Estimates show that the Lorentz force density follows to $F \sim \sigma \overline{u} B^2$, where σ is the electrical conductivity of the moving conductor, $\overline{u}$ is the magnitude of the velocity and B is the magnitude of the magnetic induction. Measuring this force, which acts on the magnetic system, allows to determine the mean velocity of the moving conductor. Since the drag force is proportional to the square of the magnetic induction, it is possible to improve the sensitivity of the measurement technique by increasing the magnetic field intensity. The method, therefore, can be applied to poorly conducting substances like electrolytes or glass melts. Recently, Wegfraß *et al.* (2012) proved the feasibility of LFV in electrolyte pipe flow. However, this still requires further optimization of the design of the magnetic system as well as further improvement of the force measurement system (Wegfraß, 2012).

LFV has the potential to be extended to the use of a small permanent magnet, possibly allowing for not only global flow measurement such as the determination of the flux through a pipe or channel, but also for local flow measurement. The specific goal of the present work is to characterize the interaction between the utilized small magnet and the flow.

The principle of LFV is shown in figure 1.2. Inside the pipe, a laminar pressure-driven flow of an electrically conducting liquid exists, $\boldsymbol{u} = u_x(y, z)\boldsymbol{e}_x$ (cf. figure 1.2a). When a magnetic dipole is brought close to the flow, the magnetic field induces electric currents inside the flow in accordance to Ohm's law (cf. figure 1.2b). These currents remain inside the flow when the side walls are insulating. This is accompanied by two effects. First, the presence of electric currents in the moving liquid induces a secondary magnetic field (cf. figure 1.2c). This secondary magnetic field will be much weaker than the primary field of the point dipole. In many applications in metallurgy, one can assume that the secondary magnetic field is negligible relative to the primary field. This idea coincides with the assumption that the *magnetic* Reynolds number Rm (Davidson, 2006; Moreau, 1990) is very small. In the present simulation, we neglect the secondary field and apply the quasistatic approximation. Physically, this means that the flow is unable to deform the field lines of the magnetic dipole. Second, the currents induced by the primary magnetic field of the dipole generate a Lorentz force $\boldsymbol{F}$ which acts back on the liquid and changes the structures of the flow (cf. figure 1.2d). We will observe that this Lorentz force gives rise to a deformation of the velocity profiles (see chapter 5) and is even able to trigger a transition to turbulence (see chapter 6). Due to Newtons third law, a counter force $-\boldsymbol{F}$

acts on the magnetic dipole which is of same magnitude as the total Lorentz force in the conduit, but has opposite sign.

The first part of this work is focused on the determination of this force and the derivation of mean flow properties from its magnitude. Hereafter, we will zoom in and focus to the particular impact of the Lorentz force on the velocity field and the resulting flow transformation.

1.4. Scope of the Thesis

The aim of this work is to study the influence of localized and inhomogeneous magnetic fields on a three-dimensional shear flow. For the magnetic field the natural choice is a point dipole – as it has the advantage of being described by an analytical expression (Jackson, 1998). Such a point dipole was also considered by Cuevas *et al.* (2006*a,b*) for a two-dimensional flow. The present work focuses on the flow in a square duct. This is one of the most investigated shear flows and known to be linearly stable (Tatsumi & Yoshimura, 1990). In addition, the structures for the turbulent regime are well investigated (Gavrilakis, 1992; Uhlmann *et al.*, 2007).

Accurate laboratory measurements in MHD flows are difficult and expensive. The choice of the used liquid metal is here for example between an expensive GaInSn alloy that is liquid at room temperature or a cheaper metal that requires higher temperatures to melt. Moreover, technical limitations can restrict the experiment to a defined range of parameters, e.g. a fixed strength of the permanent magnet.

Direct numerical simulations (DNS) can fill this gap in parts by providing the fully resolved space-time evolution of three-dimensional velocity fields and Lorentz force components that affect the motion. On the one hand, cases of transient or turbulent fluid motion will then remain limited to a moderate range of dimensionless parameters, which will be the Reynolds and Hartmann numbers.[2] On the other hand, DNS is the only method to study the local impact of the magnetic field and to investigate related parameter dependencies systematically. The last point sets the main motivation for the present analysis.

In the framework of the Lorentz force velocimetry, it is desired to obtain as much information as possible about the measured forces that are influenced by the flow. However, the approach of the present work is to investigate the behavior of the flow itself. As a matter of fact, the force that is measured at the magnet will influence the structures in the liquid. This influence might lead to unknown or even unwanted effects and thereby changes the measured force. To identify the principles of these effects, we investigate the influence of a magnetic point dipole on liquid metal flow in a square duct.

Several questions arise in this investigation. Before considering the reaction of the flow in

---

[2]The Reynolds number is defined as the ratio of inertial forces to viscous forces inside the fluid and the Hartmann number as the ratio of electromagnetic to viscous forces. Both parameters are defined in section 2.1 on page 11.

detail, it is reasonable to consider an unperturbed profile and to ask:

1. How strong is the total force that acts on this system? The answer definitely depends on several parameters. Thus, the question can be divided into:

   a) What is the influence of the strength and the shape of the magnetic field? This can be quantified with the Hartmann number and the position of the dipole.

   b) What is the influence of the state of the flow on the total force, i.e., is there a different behavior for laminar and turbulent flow? The answer can be found by investigating the force as a function of the Reynolds number.

Having obtained some information on the total force, one may proceed to the investigation of the Lorentz force density and its local effects. The acting force leads to a certain deflection of the flow, as was found in the magnetic obstacle study (Votyakov *et al.*, 2008).

2. What kind of deflection occurs? What is the physical mechanism driving such a phenomenon?

3. What is the difference in the total force between the case of an undeflected and a deflected flow? Is there a certain range within which the flow can be approximated by an unaffected hydrodynamic profile?

An interesting regime for hydrodynamic investigations is the transitional regime, i.e. the state, where the flow is still laminar, but likely to become turbulent. Considering this regime gives rise to more questions, such as:

4. How are the forces affected when the flow changes from the creeping to the transitional regime?

5. Can the dipole trigger turbulence in the originally laminar flow? Is there a threshold in the strength of the magnetic field for the transition to occur?

In order to answer these questions, several numerical calculations are performed. Based on this framework, this thesis is organized as follows. In this introduction, we give a short review of previous research that is related to the subject and the basic principles of Lorentz force velocimetry. The geometry and setting of the problem under consideration are discussed in section 2.1. The numerical method of the DNS code is described in sections 2.2 and 2.3. In chapter 3, the focus is on the detailed verification and validation of the results. Chapter 4 is devoted to the investigation of the kinematic problem. In this regime, the flow is not influenced by the magnetic field. Thus, it is possible to derive analytic correlations and to investigate the questions 1a) and 1b). The results for low Reynolds numbers describe the basic deformations of the flow field in section 5 for the stationary regime. This regime exists for lower Reynolds numbers and persists when both, Hartmann and Reynolds number, are increased to a certain point. The three sections on the basic principles of the deformation (section 5.1), the Hartmann (section 5.2) and the Reynolds dependence (section 5.3) are each devoted to the corresponding question 2, 3 and 4, respectively. The last question will be answered in chapter 6, where the transition to turbulence is discussed for the case of increasing Reynolds number. The conclusion and a brief outlook is given in chapter 7.

Contributions to this work

Chapter 4 is based on Heinicke *et al.* (2012) and Kirpo *et al.* (2011). Only results that were contributed by the author to these articles are repeated in the present work.

Thomas Boeck gave the derivation for the semianalytic presentation for small distances, that is presented in this chapter and published in Heinicke *et al.* (2012).

The derivation of the power law for large distances was already published in Kirpo *et al.* (2011) and is based on an idea of André Thess for a vertically oriented dipole.

2. Methods

Several questions were posed in section 1.4. In this chapter, the methods are presented that are applied to solve the tasks of section 1.4. In the beginning, we explain the setup and the equations of motions that are solved by direct numerical simulations. This is followed by the numerical algorithm and a detailed description of the relaminarisation zone that is used for calculations in the regime of high Reynolds numbers.

2.1. Equations of motion and setup

We consider the flow of an electrically conducting fluid in a square duct exposed to an inhomogeneous magnetic field. The magnetic field is provided by a point dipole, that is placed above the top surface of the duct in a certain distance h. A sketch of the setup is shown in figure 2.1. We use Cartesian coordinates, where the streamwise direction is denoted as x, spanwise as y and vertical wall-normal as z. The origin is chosen to be at the centerline of the duct. Thus, the duct extents in y and z-direction from -1 to 1. The position of the dipole is then given by $\boldsymbol{r}_0 = (0, 0, h + 1)$, symmetrically above the vertical center plane.

The analytic expression of the magnetic flux density for the dipole is given by (Jackson, 1998)

$$\boldsymbol{B}(\boldsymbol{x}) = \frac{1}{\sqrt{k_x^2 + k_y^2 + 4k_z^2}} \left(\frac{3\boldsymbol{m} \cdot \boldsymbol{r}}{r^5} \boldsymbol{r} - \frac{\boldsymbol{m}}{r^3} \right), \tag{2.1}$$

where $\boldsymbol{m} = k_x \boldsymbol{e}_x + k_y \boldsymbol{e}_y + k_z \boldsymbol{e}_z$ is the orientation of the magnetic moment with $k_x^2 + k_y^2 + k_z^2 = 1$ and $\boldsymbol{r} = \boldsymbol{x} - \boldsymbol{r}_0$. The magnetic flux density in equation (2.1) is normalized such that the maximal magnitude inside the liquid equals one.

The orientation of the magnetic moment of the point dipole, or shorter the dipole orientation, is one of the key parameters in the following study. We will call the orientation streamwise if $\boldsymbol{m} = \boldsymbol{e}_x$, spanwise if $\boldsymbol{m} = \boldsymbol{e}_y$ and vertical if $\boldsymbol{m} = \boldsymbol{e}_z$. We restrict our study to these three main orientations, but preliminary studies have shown, that oblique orientations lead to more complex structures in the flow.

In addition to the geometry parameters, we have the two dimensionless parameters, Re and Ha. The Reynolds number Re is defined as

$$Re \equiv \frac{\overline{u}L}{\nu}, \tag{2.2}$$
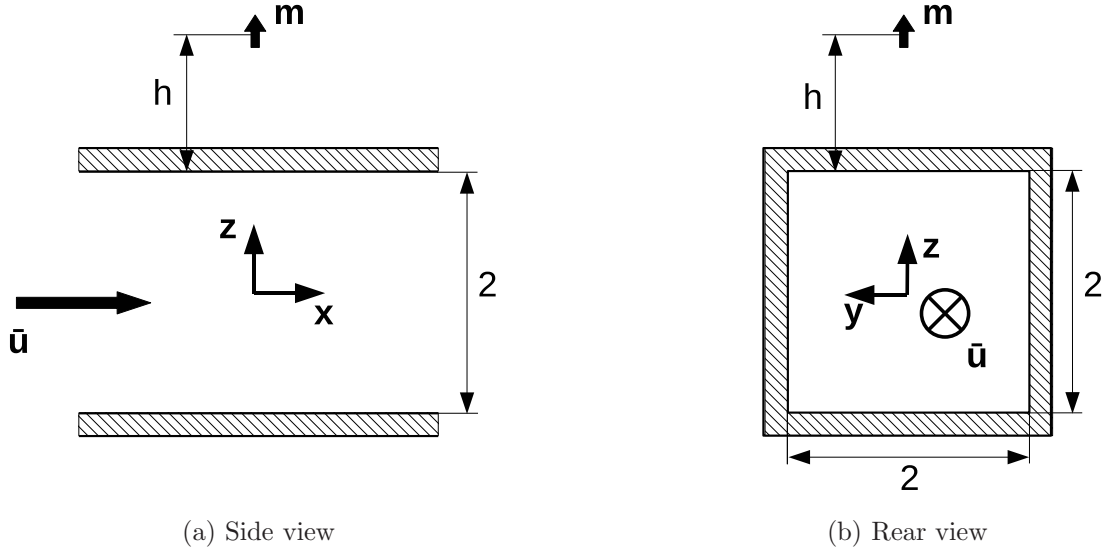
(a) Side view   (b) Rear view

Figure 2.1.: Setup of the problem. The mean velocity $\overline{u}$ of the duct flow points in positive x-direction. The center of the coordinate system is placed at the center of the duct. The distance between magnetic point dipole and fluid surface is denoted as h. The orientation of the magnetic moment of the point dipole is labeled as $\boldsymbol{m}$. The characteristic length scale of this setup is chosen to be the half-width of the duct. All lengths are expressed in this unit.

where $\overline{u}$ is mean streamwise velocity, L is the characteristic length scale, which is for the present case the duct half width, and ν denotes the kinematic viscosity. The strength of the magnetic field can be quantified by the Hartmann number which is given by

$$Ha \equiv B_{max}L\sqrt{\frac{\sigma}{\rho\nu}}, \tag{2.3}$$

where B_{max} is the maximal magnetic field flux density inside the liquid, ρ the mass density and σ the conductivity. While there is a unique definition of the Hartmann number in the case of a uniform magnetic field, the definition of Ha in the present case of a non-uniform field involves an ambiguity related to the choice of the magnetic flux density. Here, we define Ha based on the maximum of the magnetic flux density B_{max} which occurs at the upper boundary of the duct right below the dipole at point $x = y = 0$ and $z = 1$. It should be noted that in general B_{max} is a complicated function of $\boldsymbol{m}$ and h. For the sake of generality, we define Ha in terms of B_{max} rather than in terms of $\boldsymbol{m}$ and h.

With the given parameters $\boldsymbol{m}$, h, Ha and Re, several numerical simulations are presented in this work. These can be classified in the two-dimensional parameter-subspace spanned by the Reynolds number Re and the Hartmann number Ha depicted in figure 2.2. Each point in the graph denotes a simulation. The distance h from the dipole to the surface of
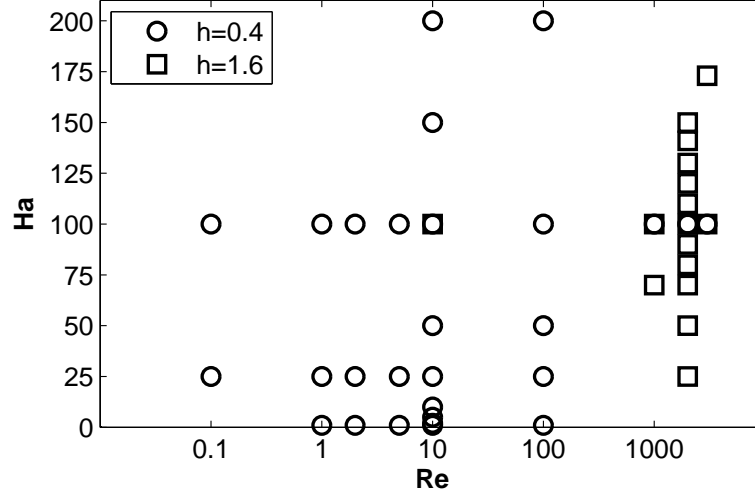
Figure 2.2.: Range of Hartmann and Reynolds numbers, Ha and Re, as presented in the work. Each point denotes a separate direct numerical simulation. The distances h of the dipole from the top surface of the duct is $h = 0.4$ (circles) or $h = 1.6$ (squares), measured in units of the half width of the duct.

the liquid is set to $h = 0.4$ for low Reynolds numbers and kinematic simulations. Thereby, one reaches the regime that can be investigated in laboratory experiments (Heinicke *et al.*, 2012). As the focus is on the integral values in this regime, the orientation of the magnet plays a minor role. For higher Reynolds numbers $h = 1.6$ is used, because in this setting, time-dependent flow structures are observed. In this distance, the orientation of the dipole is important as it influences the deflection and thus the obtained structures in the flow.

In the calculations, the fluid is assumed to be in a laminar state before it interacts with the dipole field. The velocity profile matches the approximation $\boldsymbol{u} = \frac{v}{|v|}\boldsymbol{e}_x$, with

$$v = \sum_{n,m=0}^{8} \frac{(-1)^{n+m}}{(\beta_n^2 + \beta_m^2)\beta_n\beta_m} \cos(\beta_n y) \cdot \cos(\beta_m z). \tag{2.4}$$

with $\beta_m = \frac{2m+1}{2}\pi$. This is an approximation to the analytic formula for the laminar flow profile (Pozrikidis, 1997). In the simulations, the velocity is normalized such that the flux equals one.

The laminar profile also represents the initial state of the flow. As stated in section 1.3, the magnetic field induces electric currents $\boldsymbol{j}$ in the flow, that can be determined with the help of Ohm's law,

$$\boldsymbol{j} = -\nabla\varphi + \boldsymbol{u} \times \boldsymbol{B}.$$

Here, φ denotes the electric potential. The currents give rise to the Lorentz force density

$$\boldsymbol{f} = \frac{Ha^2}{Re}(\boldsymbol{j} \times \boldsymbol{B})$$

inside the fluid. The fluid deflects due to this forces and reaches an equilibrium state after a certain settling time. To model the interaction between the Lorentz force and the conducting liquid, we solve the Navier-Stokes equations

$$\partial_t \boldsymbol{u} + (\boldsymbol{u} \cdot \nabla)\boldsymbol{u} = -\nabla p + \frac{1}{Re}\nabla^2 \boldsymbol{u} + \frac{Ha^2}{Re}(-\nabla \varphi + \boldsymbol{u} \times \boldsymbol{B}) \times \boldsymbol{B} \tag{2.5}$$

for an incompressible fluid, i. e.

$$\nabla \cdot \boldsymbol{u} = 0. \tag{2.6}$$

The electric potential is calculated with the Poisson equation

$$\Delta \varphi = \nabla \cdot (\boldsymbol{u} \times \boldsymbol{B}). \tag{2.7}$$

We use no-slip boundary conditions for the velocity, i.e.,

$$\boldsymbol{u} = 0\,, \tag{2.8}$$

at all walls. Furthermore all walls are insulating and thus we apply

$$\frac{\partial \varphi}{\partial n} = 0\,, \tag{2.9}$$

where n denotes the corresponding normal direction perpendicular to the walls. In the streamwise direction we apply periodic boundary conditions in our simulations. For higher Reynolds numbers we model inflow/outflow conditions with the help of the so-called fringe force as described in the following chapter 3.

2.2. Numerical method

In computational magnetohydrodynamics several numerical methods are used to solve the Navier Stokes equations. Before deciding on a model to use, we have to determine the level of approximation that is needed to provide the required resolution for the considered problem (Sagaut, 1998). The more details one intents to obtain the more effort one has to put in. This is shown in the conceptional graph in figure 2.3. Here, three common methods are compared according to needed effort and the received completeness: Reynolds averaged Navier-Stokes (RANS), Large Eddy Simulations (LES) and Direct Numerical Simulations (DNS).

In RANS simulations and LES, an additional modeling is applied to minimize the computational costs (cf. Widlund (2000)). Both methods are used in computational MHD (Knaepen & Moreau, 2008). RANS simulations are frequently applied in research of complex systems, e. g. MHD dynamo (Kenjeres & Hanjalić, 2007*b*; Stefani *et al.*, 2009), blood flow (Kenjeres, 2008) or magnetoconvection (Cierpka *et al.*, 2007). In scientific research with focus on flow structures in turbulence the method of choice is LES (Knaepen *et al.* (2005), Kawai & Larsson (2012), Viré & Knaepen (2009)) due to its ability to show time
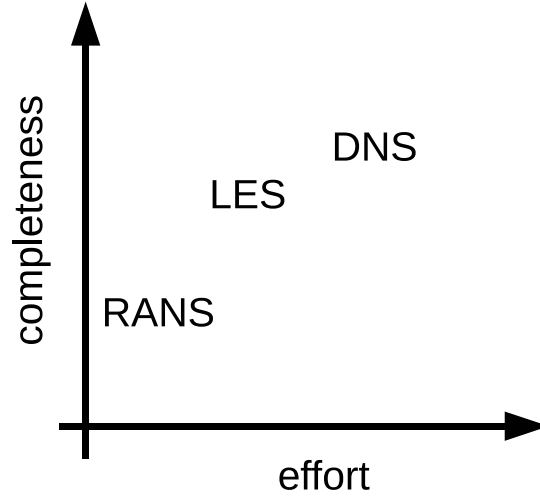
Figure 2.3.: Conceptional comparison of Reynolds averaged Navier-Stokes (RANS) simulations, Large Eddy Simulations (LES) and Direct Numerical Simulations (DNS).

dependent evolution of vortical structures. Combinations of both methods, so-called hybrid RANS-LES, are used for simulations in plane channel flow (Bhushan & Walters, 2012). The verification of these models is usually done with fully resolved DNS, e. g. Kenjeres & Hanjalić (2007a) and Viré *et al.* (2011). Such a fully resolved DNS solves the discretized equations on a very fine mesh down to the viscous scale. Due to its high accuracy, DNS need huge computational resources, but provide detailed information of the flow structures, e. g. turbulence.

As the aim of the present work is to understand the underlying principles of the interaction between the magnetic field and the flow, DNS is appropriate to reveal time-dependent and small scale structures in the velocity field. This advantage over RANS simulations and LES motivates the use of DNS in the present work.

The here presented direct numerical simulations are performed using an in-house code *Ducat*[1] (<u>D</u>uct <u>ca</u>nal <u>t</u>urbulence), that has been verified for Hartmann flow in channels and ducts by Krasnov *et al.* (2011). The finite difference code uses a second order scheme on a collocated grid arrangement. The Navier-Stokes equations are discretized in time with an explicit Adam-Bashforth/Backward Differentiation scheme. With this, the equation

$$\partial_t \boldsymbol{u} = -\nabla p - (\boldsymbol{u} \cdot \nabla)\boldsymbol{u} + \frac{1}{Re}\Delta \boldsymbol{u} + \frac{Ha^2}{Re}(\boldsymbol{j} \times \boldsymbol{B}) \tag{2.10}$$

becomes

$$\frac{3\boldsymbol{u}^{n+1} - 4\boldsymbol{u}^n + \boldsymbol{u}^{n-1}}{2\delta t} = 2\boldsymbol{R}^n - \boldsymbol{R}^{n-1}$$

---

[1]The main part of the code was written by Dmitry Krasnov. The author adjusted several routines in the code to solve the given problem.

with $\boldsymbol{R}$ being the right-hand side of equation (2.10). The superscript, e. g. n, denotes the time step and δt the time step size. The used algorithm takes advantage of the projection method. This method is based on a time-splitting discretization which decouples the computation of velocity and pressure. Here, an auxiliary field $\boldsymbol{u}^{\star}$ is obtained from the momentum equation with the incompressibility constraint and the pressure gradient ignored and is used in a second step to solve the Poisson equation for the pressure. This provides the correction of the velocity field for the next time step. Thus, the obtained velocity $\boldsymbol{u}^{n+1}$ automatically satisfies the incompressibility constraint. The convergence of this method was first proved by Chorin (1968) and Temam (1969), independently. First applications were given by Chorin (1969) for Bénard convection. The accuracy of the projection method was investigated by E & Liu (1995, 1996, 2001), who focused on influence of the boundary conditions on the convergence of the scheme.

In detail, the algorithm for proceeding from time step n to $n+1$ with a time step size δt reads as follows (Krasnov *et al.*, 2011).

1. Solve electric potential equation $\Delta\varphi^{n} = \nabla \cdot (\boldsymbol{u}^{n} \times \boldsymbol{B})$.
2. Compute electric current $\boldsymbol{j}^{n} = -\nabla\varphi^{n} + (\boldsymbol{u}^{n} \times \boldsymbol{B})$.
3. Compute $\boldsymbol{R}^{n} = -(\boldsymbol{u}^{n} \cdot \nabla)\boldsymbol{u}^{n} + \frac{1}{Re}\Delta\boldsymbol{u}^{n} + \frac{Ha^2}{Re}(\boldsymbol{j}^{n} \times \boldsymbol{B})$.
4. Compute auxiliary velocity field $\frac{3\boldsymbol{u}^{\star}-4\boldsymbol{u}^{n}+\boldsymbol{u}^{n-1}}{2\delta t} = 2\boldsymbol{R}^{n} - \boldsymbol{R}^{n-1}$.
5. Solve pressure equation $\Delta p^{n+1} = \frac{3}{2\delta t}\nabla \cdot \boldsymbol{u}^{\star}$ with the boundary conditions
   $\frac{\partial p^{n+1}}{\partial \boldsymbol{n}} = \frac{3}{2\delta t}\boldsymbol{u}_n^{\star}$ at the walls and $\boldsymbol{n}$ being the vector normal to the wall.
6. Update velocity field $\boldsymbol{u}^{n+1} = \boldsymbol{u}^{\star} - \frac{2}{3}\delta t \nabla p^{n+1}$.

For the projection method, a wide range of numerical schemes are available (Brown *et al.*, 2001). To obtain physical results, it is desirable to conserve properties like kinetic energy, mass and momentum. Systematic studies provide such schemes for hydrodynamics (Morinishi *et al.*, 1998; Vasilyev, 1998) and magnetohydrodynamics (Ni *et al.*, 2007). The code Ducat takes advantage of such highly conservatives scheme. We like to emphasize here the usage of a collocated grid arrangement, that allows to calculate velocity and current fluxes in the half-integer points in addition to the usual variables in the staggered grid positions. A skillful application of this grid provides the highly conservative scheme as used in Ducat. For more details on the algorithm and the scheme, we refer the interested reader to the work of Krasnov *et al.* (2011).

2.3. Relaminarisation of the velocity profile

About 90% of the computational time is needed to solve the Poisson equations in our problem (cf. steps 1 and 5 in the alogorithm above). Therefore, it is reasonable to chose a fast Poisson solver and accept the necessity of additional modeling. The subsequent paragraphs are devoted to this problem and answer the questions how we model a laminar inflow for Reynolds numbers at which the flow become turbulent.
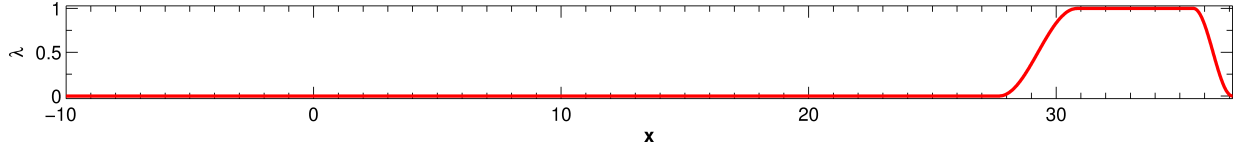
Figure 2.4.: Example for a function $\lambda(x)$ used as a prefactor in the fringe force.

Our aim is to reduce the computational costs by solving the Poisson equations with the 2D-Poisson solver FishPack (Adams *et al.*, 1999). FishPack is a collection of subroutines for solving separable partial differential equations by means of the cyclic reduction algorithm (Bini & Meini, 2009). To use this Poisson solver, we have to use periodic boundary conditions and a uniform grid in streamwise direction to apply Fast Fourier Transform (FFT). By this, we obtain for each wave coefficient a 2D Poisson problem that is solved by FishPack and retransform it into physical space. Despite the additional FFTs, the solution is calculated much faster than with the 3D multigrid solver MudPack (Adams, 1991).

The resulting drawback is the need to ensure that a laminar unperturbed duct flow profile is maintained upstream of the magnetic dipole. Thus, the computational domain has to be increased with increasing Reynolds number, when the flow is below the threshold to transition to turbulence. For $Re = 100$, a duct length of 20π was found to be sufficiently long such that the perturbations decay downstream and the laminar duct profile is completely reestablished at the end of the domain. This procedure increases the computational costs rapidly when Re is enhanced.

For higher Reynolds numbers, e.g. $Re = 2000$, the flow may become turbulent and this strategy breaks down completely. The conflict with the periodic boundary conditions is circumvented by application of an additional fringe force which acts in the final downstream section of the duct and relaminarises the partially or fully turbulent flow. This fringe method (Nordström *et al.*, 1999), sometimes also called sponge method, is a common numerical approach for relaminarisation of velocity fields and is mostly used in simulations of turbulent boundary layers (Schlatter & Örlü, 2010; Albrecht *et al.*, 2006). Our simulations show that it can also be applied for magnetohydrodynamic duct flows. This way we can take advantage of the faster Poisson solver.

The fringe method applies an artificial body force $\boldsymbol{F}_{Fringe} = \lambda(\boldsymbol{u}_{laminar} - \boldsymbol{u})$ to the right hand side of the Navier Stokes equation (2.5). It only influences the flow when the prefactor $\lambda(x)$ is non-zero. The shape of the prefactor is in our case given by the stepwise defined function

$$\lambda(\boldsymbol{x}) = \lambda_{max} \left[S\left(\frac{x - x_{start}}{\Delta_{rise}} \right) - S\left(\frac{x - x_{end}}{\Delta_{fall}} + 1 \right) \right]$$

with

$$S(x) = \begin{cases} 0, & x \leq 0, \\ 0.5 - 0.5\cos(x\pi), & 0 < x < 1, \\ 1, & x \geq 1. \end{cases}$$
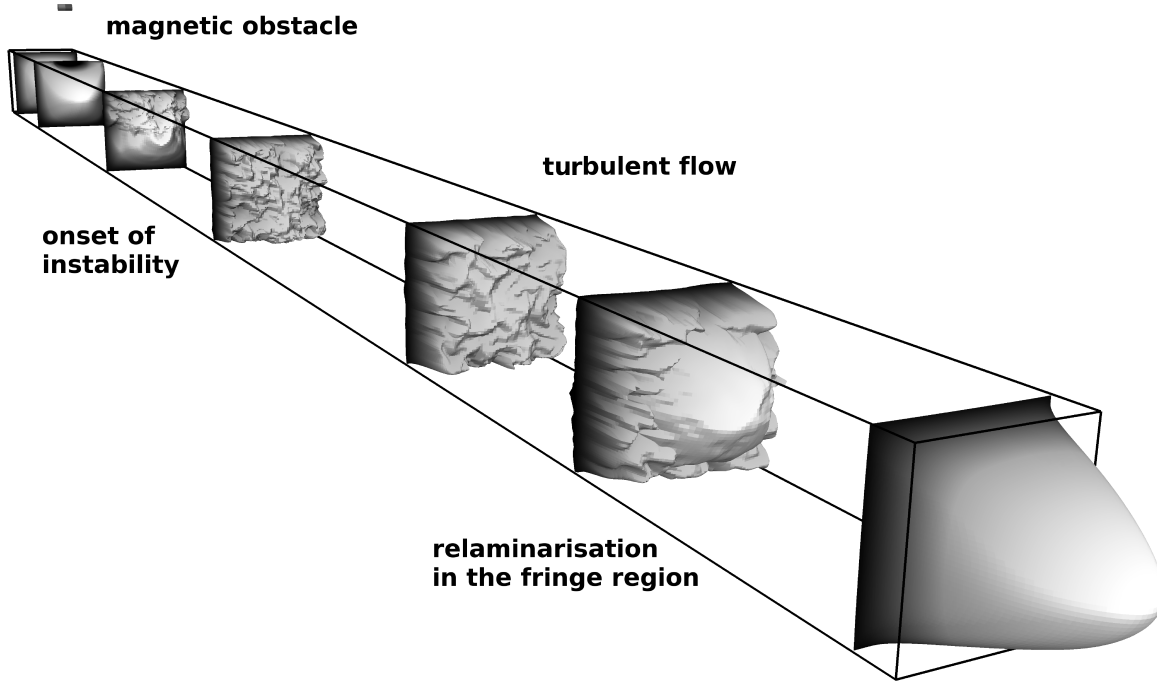
Figure 2.5.: Sketch of principle of the fringe method. The laminar flow is deflected by the dipole that acts as a magnetic obstacle. The wake is strongly deformed and may become turbulent. In the region close to the end of the duct, the fringe force relaminarise the flow. At the end of the domain, the profile is laminar again. This method allows to use periodic boundary conditions in the streamwise direction.

This function was used by Albrecht *et al.* (2006) and is shown in figure 2.4. In preliminary investigations, we studied the influence of the parameters, i.e. the maximal amplitude λ_{max}, steepness of the curve in the beginning Δ_{rise} and in the end Δ_{fall} as well as the total length $|x_{end} - x_{start}|$ of the fringe zone. The higher λ_{max} the stronger is the damping. In our calculations, $\lambda_{max} = 1$ is suitable to relaminarise the flow. Some additional tests are done with an alternative function

$$S_{\text{alter}}(x) = \begin{cases} 0, & x \leq 0, \\ 1/[1 + \exp(\frac{1}{x-1} + \frac{1}{x})], & 0 < x < 1, \\ 1, & x \geq 1, \end{cases}$$

but no advantages are detected in comparison to the original function.

An example for the resulting velocity profiles is shown in figure 2.5. Here, the transformation of the flow by the magnetic dipole for $h = 1.6$, $Re = 3000$ and $Ha = 100$ is illustrated. This computation is performed with 8192×256^2 grid points (in x, y, z) and a duct length of 30π. Before verifying the applied fringe method in section 3.2, we provide some details on the used meshes in the following section.

3. Verification and Validation

This chapter is devoted to the verification and validation of the numerical code. In the first section, we provide a grid sensitivity study. This is followed by a detailed verification of the DNS code with three other numerical methods. We prove that the relaminarisation zone introduced in section 2.3 correctly models the inflow/outflow conditions. Last, the turbulent mean velocity profile and Lorentz forces obtained from the DNS are validated with experimental results.

3.1. Grid sensitivity studies

There are three challenges that need to be captured for a proper resolution in a DNS: the boundary layers, small scales in turbulent flow and the steep gradient of the magnetic field of the point dipole. They become increasingly important for higher Hartmann and Reynolds numbers, where strong gradients of velocity and magnetic flux have to be resolved in thin boundary layers, which leads to a transition to turbulence in the wake.

Two approaches to solve this problem are employed here. The first and most simple approach is to increase the number of grid points. This naturally increases the computational cost, i. e. the random accessible memory and single CPU time. Therefore, as a second approach, a grid stretching is applied that increases the number of points in the boundaries. The stretching functions are given by (Krasnov *et al.*, 2011)

$$y = \frac{\tanh(\alpha_y \eta)}{\tanh(\alpha_y)} \tag{3.1}$$

based on the hyperbolic tangent and

$$y = \beta_y \sin(\eta \frac{\pi}{2}) + (1 - \beta_y)\eta$$

for a Chebychev based stretching. Here, η is the coordinate on a uniform grid, y denotes the transformed coordinate, while α_y and β_y are the stretching coefficients. The stretching in z-direction is given analogously. This grid refinement at the walls provides a better resolution in the boundary layer while keeping the total number of grid points unchanged. Both approaches, the grid refinement and the stretching give rise to an increase in the total computational time of the present explicit numerical scheme. According to the Courant-Friedrichs-Lewy condition (Ferziger & Peric, 2002),

$$\Delta t < \overline{u}\Delta x,$$

the minimal separation between two grid points Δx gives a constraint on the maximal time step Δt. This may increase the real calculation time drastically. A refinement of the grid by factor two in every spacial direction will result in a factor of 16 for the computational time. The parallelization of the code (MPI + OpenMP) can compensate this if the computing capacity is available.

For each regime, that is considered in the investigation, a characteristic setting is chosen. Then, we provide for these examples a grid study with maximal grid refinement. The definition of "maximal" is hereby determined by constraints on the computing capacities. With this study we select a resolution and a stretching coefficient that is assumed to provide physical results and at the same time reduces the computational costs. This resolution is then used for the parameter studies.

The consecutive paragraphs give the details of the grid studies that are relevant to the three following chapters. We consider first the kinematic regime and meet the challenge of proper resolution in the study on the distance of the magnetic point dipole. Second, we have to resolve strong gradients in velocity and magnetic field for the regime of low Reynolds numbers. Finally, transitional Reynolds numbers require resolution of time dependent flow structures combined with the need for a longer computational domain (for investigations of the wake).

Parameter studies in the kinematic regime have one big advantage. As the velocity field is not influenced by the magnetic field, only one time step is necessary to compute the currents and the Lorentz force. The total Lorentz force F_x is highly dependent on the velocity and the magnetic field. It is also the main output quantity in the kinematic studies. Therefore, F_x is an appropriate characteristic value to determine whether the resolution is sufficient or not. For strong variations in the dipole distance, as considered in chapter 4, it is found that the force highly depends on the chosen grid. Therefore, the maximal possible number of grid points is used throughout the parameter study in the kinematic regime. The number of grid points is hereby limited by the computer resources. The main technical constraint is the random access memory (RAM), which is restricted to $256\,\mathrm{GB}$.[1]

The study for large dipole distances with h between 50 and 500 requires a long duct to resolve the physical effects. Here, the duct length is increased to $7.5\pi(h+1)$ while 10240×256^2 grid points are used. A different grid is needed in the case of a magnetic point dipole at a very small distance to the surface of the liquid. Here, the magnetic field possesses strong gradients in the boundary layer. The parameter study for dipole distances with h between 10^{-3} and $5 \cdot 10^{-1}$ in chapter 4 need very fine grids up to 1024×640^2 grid points on a geometry of $4 \times 2 \times 2$ and a tanh-stretching with $\alpha_y = \alpha_z = 2.0$ to provide a proper resolution.

At low Reynolds numbers the flow stays laminar. Nevertheless, the gradients of velocity and magnetic field demand a sufficient fine grid in the boundary layers. The calculations for the resolution are done for $Re = 10$, $Ha = 100$, $h = 0.4$ and a vertical oriented dipole,

---

[1]This study was done in 2010 at the computer center of TU Ilmenau. By this time the code was not yet parallelized with MPI. The calculations were therefore performed on a single node with $256\,\mathrm{GB}$ RAM.

	domain size	grid points	stretching
Gavrilakis (1992)	$20\pi \times 2 \times 2$	$1000 \times 127 \times 127$	$\alpha = 1.8417$
Huser & Biringen (1993)	$6.4 \times 1 \times 1$	$97 \times 101 \times 101$	algebraic stretching
Kinet *et al.* (2009)	$4\pi \times 2 \times 2$	$512 \times 100 \times 100$	not specified
Votyakov *et al.* (2008)	$50 \times 10 \times 2$	$64 \times 64 \times 64$	varies in all directions
present work low Re	$5\pi \times 2 \times 2$	$1024 \times 96 \times 96$	$\alpha = 1.5$
present work transient Re	$15\pi \times 2 \times 2$	$2048 \times 96 \times 96$	$\alpha = 2.0$
present work turbulent flow	$80 \times 2 \times 2$	$5120 \times 128 \times 128$	$\beta = 0.95$

Table 3.1.: Comparison of resolution in literature and the present work.

which represents the basic setting in chapter 5. The finest grid is 4096×256^2 grid points on a geometry of $5\pi \times 2 \times 2$ and a tanh-stretching with $\alpha_y = \alpha_z = 1.5$. In the presented calculations for low Reynolds numbers, we use a structured grid with 1024×96^2 grid points on the same geometry. The difference between the resulting Lorentz forces is less than 2%.

The third regime of interest is the transient flow at high Reynolds numbers, where the wake behind the magnetic obstacle may become turbulent. Therefore, it is desirable to resolve the small vortices in the turbulent flow. This is possible for resolutions like in Gavrilakis (1992) or Huser & Biringen (1993) (see table 3.1). We study the grid sensitivity for $Re = 2000$, $Ha = 100$ and a spanwise oriented dipole in distance of $h = 1.6$ with the duct length of 30π (see chapter 6). This setting is chosen as it results in time dependent flow structures and a wake that transforms into turbulent flow. The size of the grid is increased up to 8192×256^2 with stretching coefficients $\alpha = 1.5$ and 1.75. Also smaller grid sizes with similar refinement at the boundary are considered, e. g. 4096×128^2 with stretching coefficient of 2.0. The obtained Lorentz forces are equal for the finest grids 8192×256^2 and 4096×128^2. Due to the explicit scheme of the code, it is not possible to use a finer mesh in the grid study[2]. Having already reached the technical limitations in the very fine grids, we focus on coarser grids in order to investigate how effectively the computational costs can be minimized. The grid study shows that the same physical effects (e. g. the vortex shedding that is described in chapter 6) are still obtained with a resolution of 1024×48^2.

In order to reduce the computational costs, the length of the duct is reduced to 15π. This reduction of the duct length has two effects. First, half of the grid points are necessary for the same resolution in streamwise direction, which is required to resolve the wake. Second, this reduces the calculation time, because the equilibrium state is obtained quicker. The parameter studies in section 6 are performed with 2048×96^2 grid points. The accuracy of the code was again determined with the total Lorentz force. It is found that the force for the finest grids, i. e. 8192×256^2 and 4096×128^2, differs by 0.5% from the values for 2048×96^2.

---

[2]This calculations for the finest grid were performed in Jülich Scientific Computing Center on 1024 CPUs of JUROPA and took about 200 000 CPU hours.

With the chosen grids, we operate within the technical constraints and use resolutions that are similar to other DNS as shown in table 3.1. We therefore are convinced that the simulations provide physically reasonable results. To that end, the following sections present the verification (in section 3.2) and validation (in section 3.3).

3.2. Verification with other numerical codes

In the course of this PhD work, two verifications were performed for the code. The first test with kinematic setting only checks the electromagnetic part of the solver. This comparison is performed with two commercial softwares: Fluent and Comsol. The second verification is conducted with YALES, a finite volume DNS code and mainly used to verify the relaminarisation zone. To distinguish clearly between the two DNS codes, the code used in this thesis is referred to as Ducat.

The results of the first test are displayed in figure 3.1. The Fluent simulations are provided by Pulugundla (2012), while the Comsol simulations are taken from Kirpo *et al.* (2011). FLuent uses the finite volume method (FVM) while Comsol applies the finite element method (FEM). In these calculations, the kinematic approximation is applied, i. e. the velocity is given by an unperturbed laminar profile. The magnetic point dipole is positioned at a distance of $h = 0.4$, producing a magnetic field with $Ha = 185.4$. The Reynolds number is set to 2000.

The comparison in figure 3.1 shows the force, the induced currents and the electric potential along two lines: the top line at $x = 0$, $z = 1$ and a mid line at $x = 0$, $y = 0$. The figures reveal a slight underprediction of the Lorentz force and of the current directly below the dipole (at $x = 0$, $y = 0$, $z = 1$) from the Fluent simulations. This is caused by interpolation error in Fluent. The Comsol simulation used a refined mesh below the dipole to avoid this effect. The values for the electric potential, and thus the comparison of the Poisson solvers, show a very good agreement.

The comparison with the Comsol code is continued in Kirpo *et al.* (2011). In the study on the dependence of Lorentz force on distance variation with h between 2 and 80, it is found that the largest relative error between the results obtained with the two different codes was not greater than 2%.

The second verification is done through a set of calculations with YALES.[3] The Fortran90 code YALES is used for calculation of MHD problems with homogeneous fields by Vantieghem *et al.* (2009). Although there is a detailed description on YALES available (Vantieghem, 2011), we provide some facts in the following paragraph to familiarize the reader with this finite volume code. YALES applies the Crank-Nicolson scheme for the time discretization and solves the obtained algebraic equation by Jacobi method. For the subsequent verifications, the magnetic flux density is modified by inserting the analytic expression for the inhomogeneous magnetic fields in YALES. The Lorentz force term is

---

[3]Courtesy to Bernard Knaepen and Stijn Vantieghem for providing the code and support.
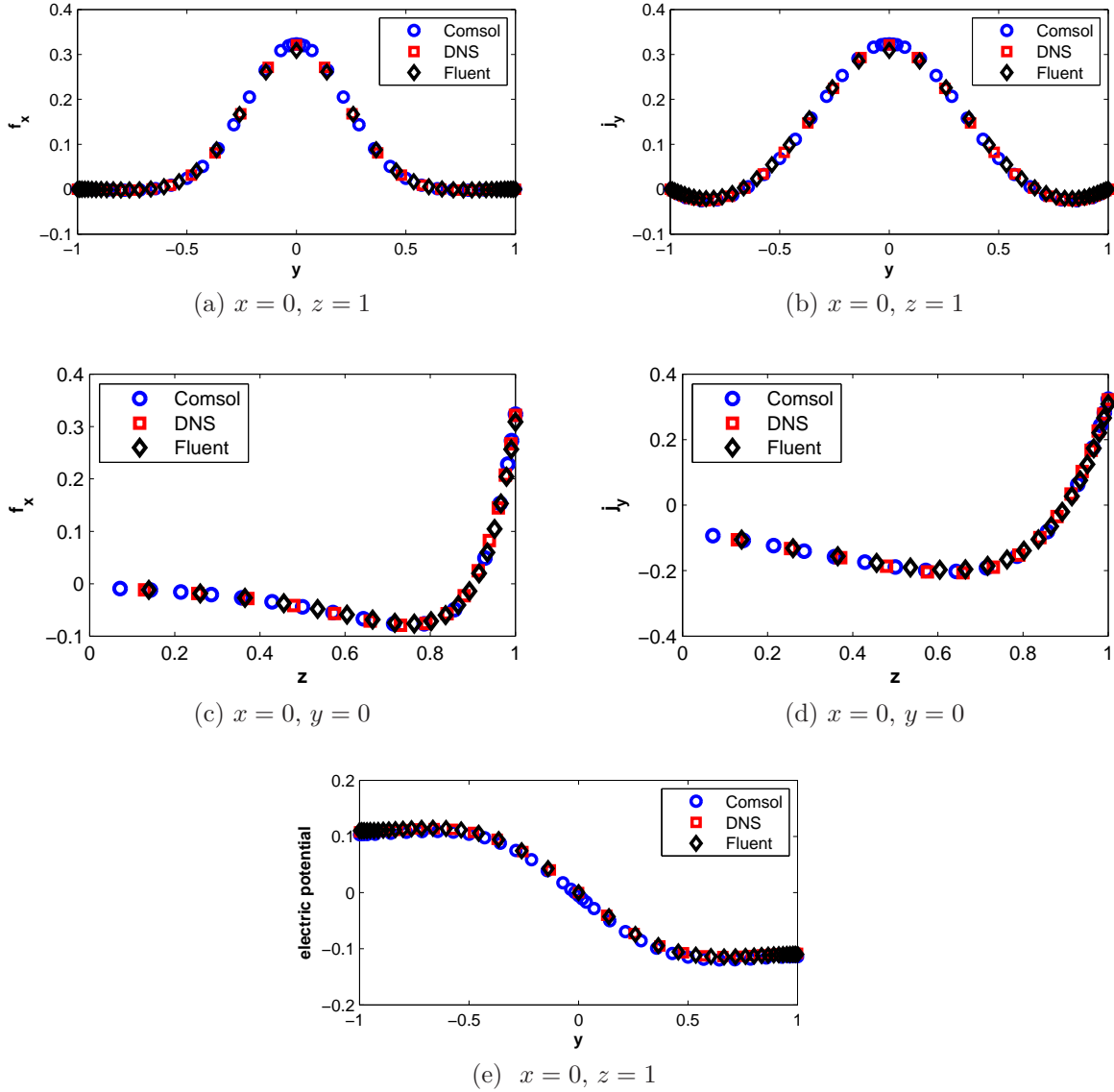
Figure 3.1.: Comparison of (a,c) Lorentz force, (b,d) currents and (e) electric potential along (a,b,e) top line with $x = 0$, $z = 1$ and (c,d) mid line with $x = 0$, $y = 0$ as obtained from Comsol by (Kirpo *et al.*, 2011), Fluent by (Pulugundla, 2012) and DNS as used in the presented work.

treated explicit in YALES and Ducat. This leads to a restriction of the time step, i. e.

$$\Delta t \leq \frac{2\rho}{\sigma B_{max}}.$$

For details of this constraint and its derivation, we refer the reader to the thesis of Stijn Vantieghem (2011) page 57. The Poisson equation is solved in YALES with an algebraic
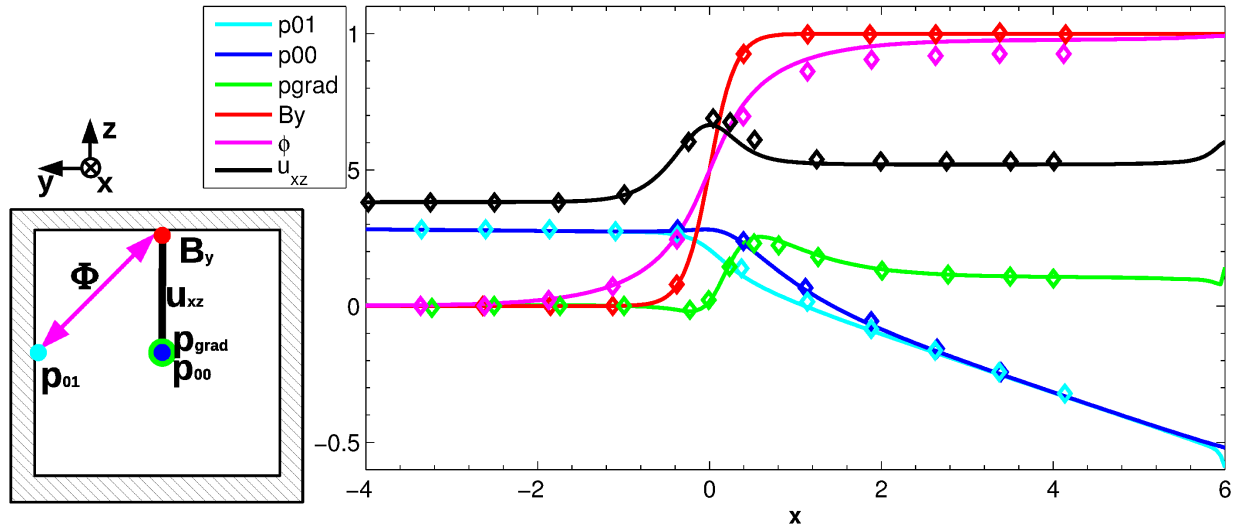
Figure 3.2.: Characteristic properties along the duct for fringing magnetic field. The comparison between simulations of Sterl (1990) (diamonds) and YALES (line) for the case of $Re = 2.5$, $Ha = 50$ and $a = 0.3$ shows a good agreement. This verification was done for conducting walls with conductivity coefficient of 0.1. Along the streamwise direction of the duct the following values are given: (By) magnetic field, (p00) pressure at the centerline, (p01) pressure at the sidewall, (pgrad) streamwise pressure gradient, (Φ) transverse potential difference, (u_{xz}) center of velocity distribution;

multigrid solver (AMG). Thus it is possible to choose the grid to be structured but non-equidistant in every direction. For the wall-normal direction a boundary layer of a certain thickness and with a certain number of cells is defined. In the bulk of the domain the grid is stretched with a hyperbolic tangent function, cf. equation (3.1) with a factor of $\alpha = 1.5674$. In streamwise direction a refinement of the grid in the middle of the duct was achieved by the stretching function $x \mapsto (x + \alpha_x x^3)/(\alpha_x + 1)$. In the presented calculations, a stretching coefficient of $\alpha_x = 2.0$ is used.

Unlike Ducat, YALES is capable of using inflow-outflow-conditions. The inlet is chosen to match the approximation for laminar flow as given in equation (2.4). At the outflow, convective boundary conditions are used for the velocity, i.e.

$$\partial_t \boldsymbol{u} + U_{conv}\partial_n \boldsymbol{u} = 0.$$

Here, U_{conv} is a characteristic velocity of the flow, as determined in the code. For the electric potential and the pressure, homogeneous Neumann boundary conditions are applied at inlet and outlet. This boundary condition is equivalent to the divergence-free constraint $\nabla \cdot \boldsymbol{u} = 0$ (Gresho & Sani, 1987; Sani *et al.*, 2006).

In YALES, Shercliff's thin wall-condition (Shercliff, 1956) is applied to simulate conducting walls. For the electric potential, the boundary conditions are specified with help of the

	Sterl(1990)	Ducat	YALES
maximum of velocity distribution	0.7339	0.7038	0.7059
velocity distribution in homogeneous magnetic field	0.4327	0.4471	0.4511
maximal pressure difference, i.e. $\max_x \lvert p(x,0,0) - p(x,0,1)\rvert$	0.0976	0.1313	0.1314
maximal potential difference, i.e. $\max_x \lvert \varphi(x,1,0) - \varphi(x,0,1)\rvert$	1.0390	1.0078	1.0158

Table 3.2.: Comparison between the codes YALES and Ducat with the reference article Sterl(1990) of some characteristic values for the case of insulating walls with $Ha = 50$, $Re = 2.5$ and $a = 0.3$.

wall conductivity coefficient c by

$$\pm \partial_y \varphi(\pm 1, z) = \partial_z [c \partial_z \varphi(\pm 1, z)],$$
$$\pm \partial_y \varphi(y, \pm 1) = \partial_z [c \partial_z \varphi(y, \pm 1)].$$

The case $c = 0$ stands for insulating walls, while $c \to \infty$ emerges as the perfect conducting walls. Details on this implementation can be found in Vantieghem (2011).

For the first comparison, we choose a simplified setting with an inhomogeneous but non-physical magnetic field, i.e. $\boldsymbol{B} = B_y \boldsymbol{e}_y$ with

$$B_y(x) = \frac{1}{1 + e^{xa/2}} = 0.5 + 0.5 \tanh(ax). \tag{3.2}$$

This field is not curl free, i.e. $\nabla \times \boldsymbol{B} \neq 0$. The shape of the field is such that it is zero in the beginning of the duct and increases to $\lvert \boldsymbol{B} \rvert = 1$ in the end. The coefficient a describes the steepness of the field in the transition zone and is chosen as $a = 1$ and $a = 0.3$. The shape of this fringing magnetic field models the entrance of a magnet.

Several simulations are done with both codes for Hartmann number of $Ha = 50$ and two Reynolds numbers: $Re = 2.5$ and $Re = 250$. One calculation with parameters $Ha = 50$, $Re = 2.5$, $a = 0.3$ and conducting walls with $c = 0.1$ serves for the verification of YALES with the results from Sterl (1990).

We compare the following characteristic curves along the streamwise direction as suggested in Sterl (1990).

(By)	magnetic field B_y at $y = 0$ and $z = 1$
(p00)	pressure at the centerline, p at $y = 0$ and $z = 0$
(p01)	pressure at the sidewall, p at $y = 0$ and $z = 1$
(pgrad)	streamwise pressure gradient $\partial_x p$ at $y = 0$ and $z = 0$
(Φ)	transverse potential difference $\lvert \varphi(x,1,0) - \varphi(x,0,1)\rvert$
(u_{xy})	center of velocity distribution at $z = 0$, $\dfrac{\int_0^1 y u_x(x,y,0)\, \mathrm{d}y}{\int_0^1 u_x(x,y,0)\, \mathrm{d}y}$
(u_{xz})	center of velocity distribution at $y = 0$, $\dfrac{\int_0^1 z u_x(x,0,z)\, \mathrm{d}z}{\int_0^1 u_x(x,0,z)\, \mathrm{d}z}$
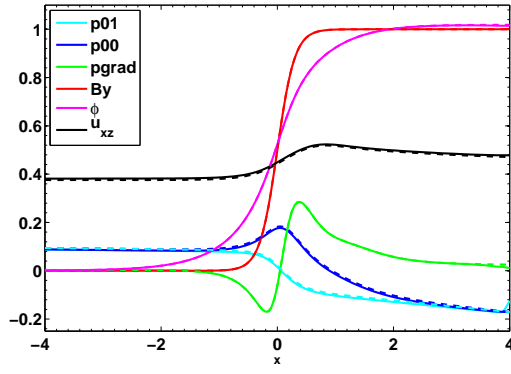
(a) fringing magnetic field for
$Ha = 50$, $Re = 250$, $a = 0.3$
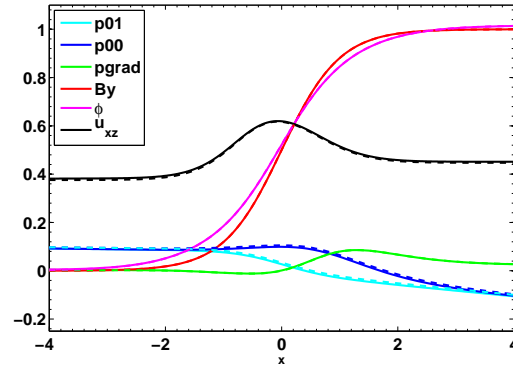
(b) fringing magnetic field for
$Ha = 50$, $Re = 2.5$, $a = 1$
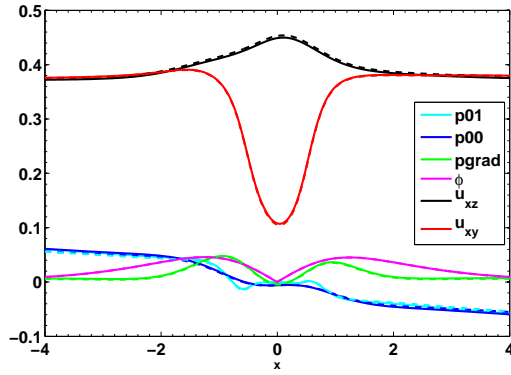
(c) streamwise oriented dipole with
$Ha = 100$, $Re = 10$ and $h = 0.8$
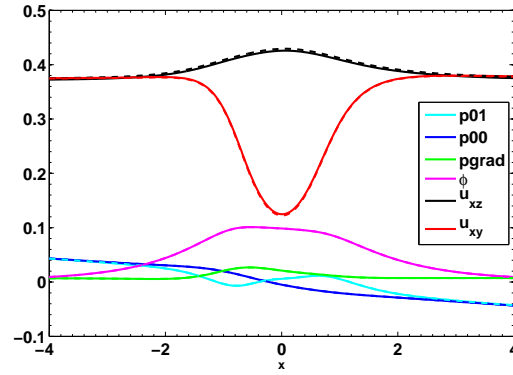
(d) spanwise oriented dipole with
$Ha = 100$, $Re = 10$ and $h = 0.8$
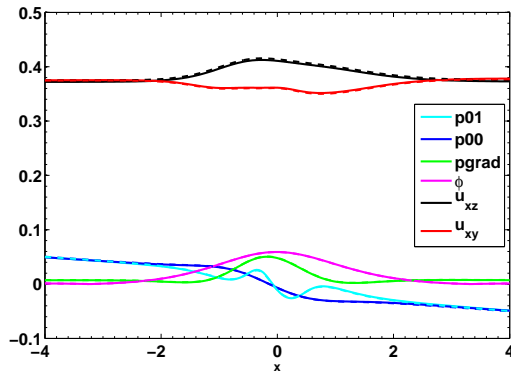
(e) vertical oriented dipole with
$Ha = 100$, $Re = 10$ and $h = 0.8$
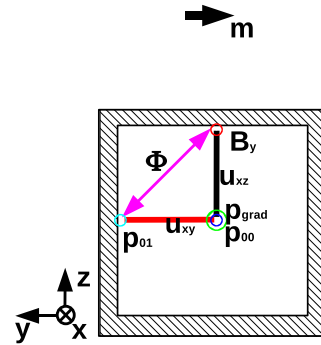
(f) sketch of used values

Figure 3.3.: Characteristic properties along the duct for fringing magnetic field (a,b) and for magnetic field of point dipole in the 3 main orientations (c,d,e). Curves along x-direction with values as indicated in (f): (By) magnetic field, (p00) pressure at the centerline, (p01) pressure at the sidewall, (pgrad) streamwise pressure gradient, (Φ) transverse potential difference, (u_{xz}, u_{xy}) center of velocity distribution in $y = 0$ and $z = 0$, respectively; YALES: continuous lines and Ducat: dashed lines.
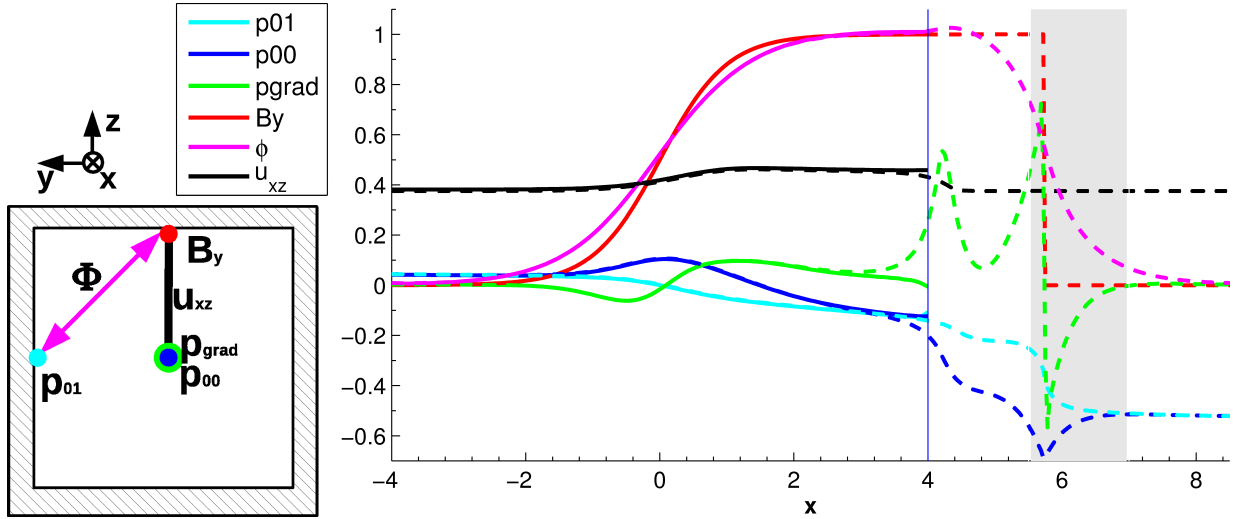
Figure 3.4.: Verification of the relaminarisation zone for fringing magnetic field. Values as shown in the sketch on the left with same notation as in 3.3. YALES: continuous lines and Ducat: dashed lines. The blue line at $x = 4$ marks the position, where YALES has the outflow and the relaminarisation zone starts for Ducat. The gray area resembles the range with maximal fringe force, i.e. $\lambda(x) = 1$.

In the beginning, the code YALES is verified with the data from Sterl (1990) as shown in figure 3.2. A very good agreement is achieved for the pressure and pressure gradient. The calculated potential difference is higher than the reference data. This is also the case for the comparison of Mistrangelo (2005) with Sterl (1990). One reason may be the lower resolution in the calculations of Sterl (1990). In almost the same manner the velocity distribution is higher, which might also be a side effect of the lower resolution. It was stated by Sterl (1990) that "calculations done with 32^3 points and $22 \times 40 \times 40$ points at $Ha = 10^2$ show differences of less than 5 %." Following this argument, we consider the verification with this reference data as acceptable as the physical behavior is qualitatively the same.

A comparison for the characteristic curves between Ducat and Sterl (1990) suffers from a lack of data for insulating walls in the reference. We restrict ourselves here to given maximal values for insulating walls with $Ha = 50$, $Re = 2.5$ and $a = 0.3$. In table 3.2 these values are compared with both codes. These values show a better agreement between YALES and Ducat than with the given reference. This may be caused by the coarse grid that was used in Sterl (1990). In the reference the resolution was $24 \times 40 \times 40$ and $32 \times 32 \times 32$ on a duct of size $8 \times 2 \times 2$, while the simulations with YALES had $1000 \times 100 \times 100$ grid points and the one with Ducat had $384 \times 96 \times 96$, respectively. Additionally YALES and Ducat use grid stretching to refine the boundaries.

Figure 3.3 shows the comparison for the fringing magnetic field (3.2). Both codes give identical results in the physically relevant part of the computational domain. The relaminarisation zone and the region of the outlet are not plotted here.

As a second setting we use the liquid metal duct flow with the magnetic field of a point dipole (2.1) as considered in the present work. Similar to chapter 5, we consider a low Reynolds number flow (at $Re = 10$) that is deflected by a strong magnetic field with Hartmann number of 100 and a dipole distance of $h = 0.8$ to the surface. This leads to a well pronounced deflection of the velocity profile as shown in figure 5.1 on page 44. Both codes give equivalent results (see figure 3.3).

To verify the vortex shedding observed for higher Reynolds number in chapter 6, a qualitative calculation with coarse grid of $652 \times 48 \times 48$ grid points and duct with a geometry of $60L \times 2L \times 2L$ was done in YALES. The result is qualitatively the same as with Ducat, i.e., the flow shows the same time dependent behavior.

Finally, we analyze the end of the domain and focus on the relaminarisation zone in the Ducat code. Due to the deformation of the flow by the Lorentz force, small scale structures are advected downstream and may reflect at the outlet or the relaminarisation zone. Both methods, the outlet boundary conditions in YALES and the relaminarisation zone in Ducat, are supposed to prevent such reflections, but show peculiarities in the end of the domain. To quantify these in size and magnitude, we compare the effect of the outlet in YALES with the one in Ducat in figure 3.4. This calculation for Reynolds number $Re = 250$ is done on the same calculation geometry of $2 \times 2 \times 8$, i.e. the relaminarisation zone is placed behind the computational domain with an additional length of 4.566. In the YALES calculation, small scale oscillations are amplified at the outlet. One possible reason for this is assumed to be the combination of strong grid stretching in streamwise direction and the multigrid solver. These instabilities may appear at inlet and outlet where the grid size is highest and are less pronounced in tests with uniform grids.

The influence of the relaminarisation region in Ducat is much higher than the influence of the outlet in YALES. As shown in figure 3.4, the pressure gradient (pgrad) is affected for about 2 characteristic length units. However, nor unusual effects are found in the velocity field which is also indicated by the center of velocity distribution (u_{xz}). In all calculations, the observed unphysical effects never increases or moved into the computational domain. This confirms the reports by Albrecht (2010) on the good properties and the reliability of the relaminarisation zone. Nevertheless, it is ensured that the presented results in this thesis are obtained from flow structures sufficiently far from the relaminarisation zone. The artificial example in figure 3.4 shows also that the relaminarisation zone is only efficient if the computational domain is appropriately long.

The given verifications in this section show that the results of the code agree very well with commercial software as well as with YALES, a second DNS code. Calculations were presented for a well known case of a fringing magnetic field and the case of a point dipole. As the latter is not often considered in literature, we provide an additional validation in the following section. This will complete the proof of having obtained physical results.
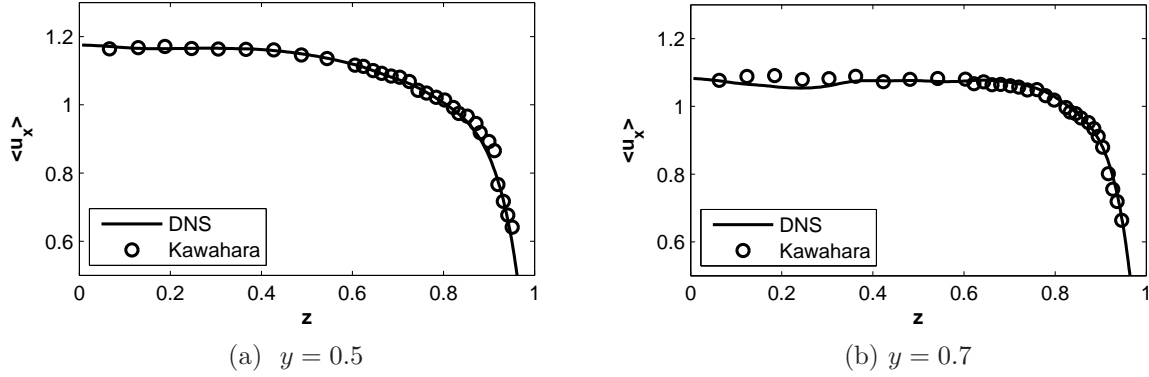
(a) $y = 0.5$ (b) $y = 0.7$

Figure 3.5.: Validation of the mean velocity profile for turbulent flow. Experimental data is given by Kawahara *et al.* (2000) at $Re = 3535$. Numerical data is calculated at $Re = 3500$, by taking the spatial mean values for fully developed turbulent flow. Values for the mean streamwise velocity are given along two lines: (a) at $y = 0.5$ and (b) at $y = 0.7$. The curves show a good agreement, especially at the boundary.

3.3. Validation with experimental data

Though the chosen setting is quite far from reality, we attempt a validation of two aspects in our calculations. The first part of the validation concerns the hydrodynamic velocity profile, while the second part focuses on the electromagnetic force.

The parameter study in section 4.3 considers the Lorentz force for turbulent mean profile. Thus the subsequent paragraphs refer to the task of how a proper mean profile for the turbulent flow is obtained. For one of the profiles a validation is provided with the experimental data by Kawahara *et al.* (2000).

The hydrodynamic velocity profile is well known for the laminar duct flow (Pozrikidis, 1997). Using the first eight terms of the analytic solution (2.4) provides a proper laminar profile in the relaminarisation zone. For turbulent mean flow no analytic formula is known so far. Reference data is mostly provided by numerical simulations (Gavrilakis, 1992; Huser & Biringen, 1993). The main challenge is to resolve the secondary flow. Several works focused on this problem, e.g. Kawahara & Kamada (2000); Petterson Reif & Andersson (2002); Bottaro *et al.* (2006); Uhlmann & Pinelli (2007); Uhlmann *et al.* (2007); Wedin *et al.* (2008); Biau *et al.* (2008); Uhlmann *et al.* (2010) and Pinelli *et al.* (2010).

The investigation of the dependence of the Lorentz force on the profile of the velocity field in section 4.3 (cf. figure 4.4 on page 40) is based on mean profiles. These profiles are obtained as spatial mean values of fully developed turbulent flow in a duct of size $80 \times 2 \times 2$ on $5120 \times 128 \times 128$ grid points. It has to be noted here that used spatial average is not appropriate to obtain the statistical values with same accuracy as in the literature above. In the presented benchmark, only the primary flow has an influence on the resulting Lorentz force. This is an effect of the symmetry of the setting. Hence, the probably underresolved

secondary flow will not enter the results. Thus the following validation is only concerned with the primary flow, i. e. the mean of the streamwise velocity component.

The mean profiles for turbulent flow are validated with experimental data from Kawahara *et al.* (2000).[4] Figure 3.5 gives the validation for the turbulent profiles that are used for kinematic calculations in section 4.3. The experimental data by Kawahara *et al.* (2000) are given for Reynolds number 3535, while the numerical simulation used 3500. Nevertheless, the comparison shows a very good agreement (see figure 3.5). A slight mismatch is observed in the bulk in figure 3.5b. For the later calculation the profile close to the boundary plays an important role. It is the boundary where the Lorentz force reaches its highest value. The agreement between the experiment and numerical data is therefore sufficient for our investigations.

The second validation case concerns the laboratory experiments by Heinicke (2012). A sketch of the experimental setup is given in figure 3.6a. A small magnet (depicted in green in the figure) is mounted on a measurement system that is positioned at a certain distance h from the square duct. The duct is filled with Galinstan, a Gallium-Indium-Tin-alloy that is liquid at room temperature. A electromagnetic pump (not shown in the picture) drives the fluid with the adjusted velocity.

Before attempting the comparison of the measured Lorentz forces, the following question arises: How strong is the disagreement in the magnetic flux density between a magnetic point dipole and a permanent magnet as used in the experiment? Figure 3.6b compares the magnetic field of a dipole and of a permanent magnet of $1\,\mathrm{cm}^3$ as used in the experiments. The comparison considers the strongest component of the magnetic field along the line of magnetization. The data are normalized such that both magnet systems have a Hartmann number of $Ha = 165$ at a distance of $h = 0.4$. This distance is the smallest where Lorentz forces can be measured in the experiment. The decay of the field is stronger in short distance for a point dipole than for a cube magnet. For high distances, both magnetic fields coincide as the permant magnet corresponds more to the model of a point dipole.

A comparison of the total Lorentz force is shown in figure 3.6c for laminar flow and in figure 3.6d for a turbulent case. The measured Lorentz forces and the simulated values show a good agreement. The numerical simulations are done in the kinematic setting (cf. section 4). The choice of this simplified setting can be justified by the drastic increase of computational costs for a parameter study with the full equations solved. Here, the laminar velocity field for simulations at $Re = 754$ in figure 3.6c is given by the analytic formula (2.4). The simulations for the turbulent case with $Re = 9279$ are done with a spatially averaged velocity profile that was obtained numerically by spatial averaging as in the validation above (cf. figure 3.5). A benchmark with turbulent flow plus the deflection due to the Lorentz forces would demand not only long time averaging, but also the use of inflow/outflow conditions. With the present periodic boundary conditions in streamwise direction, the distortion due to the Lorentz forces may built up and artificially amplify. Therefore, the validation for the high Reynolds numbers had to be done with the kinematic

---

[4]Courtesy to Markus Uhlmann for providing these data.

(a) sketch of the experiment

(b) magnetic fields

(c) Lorentz force for laminar case
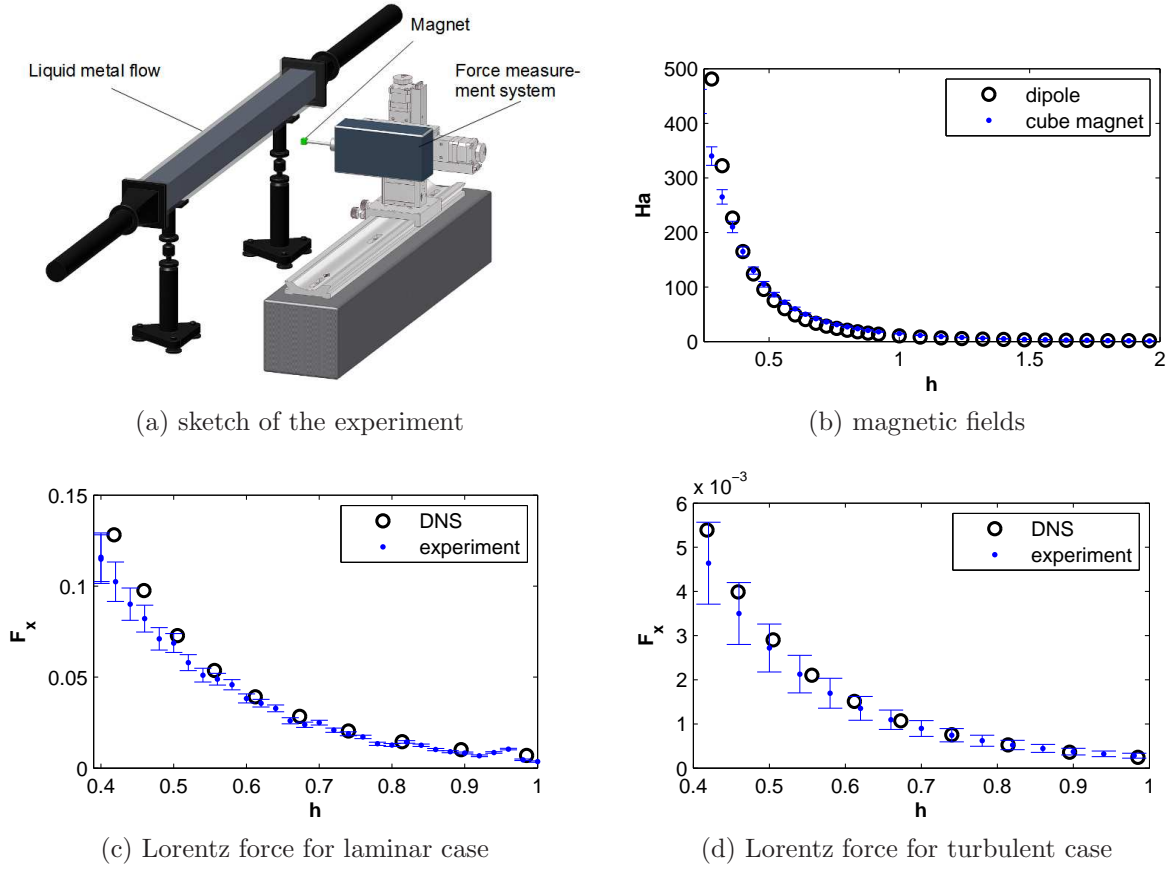
(d) Lorentz force for turbulent case

Figure 3.6.: Comparison with experimental data provided by Heinicke (2012). (a) Sketch of the experimental setup (courtesy of Heinicke (2012)) (b) Hartmann numbers in dependence on the distance for a $1\,\mathrm{cm}^3$ cube permanent magnet with a point dipole of same Hartmann number at $h = 0.4$. (c) Lorentz force for laminar flow at $Re = 754$ and d) for turbulent flow at $Re = 9279$.

approximation.

For both Reynolds numbers the numerical simulation in figures 3.6c and 3.6d overpredicts the measured values. A simple reason for this mismatch may lie in the kinematic approximation. When the deflection of the liquid inside the duct is ignored, the resulting Lorentz force increases. This effect is strongest for high Hartmann numbers (cf. figure 5.5d) that correspond to small distances. A second source of errors would be the use of different magnetic fields. As shown in figure 3.6b, the magnetic point dipole underpredicts the strength of the magnetic field of the permanent magnet. As the different shapes of the magnetic fields would lead to an underprediction of the total force, this effect must be much weaker than the effect of the flow distortion.

Nevertheless, the validation showed that the simplified setting of a point dipole is able to

predict the qualitative behavior of the total Lorentz force in the duct. For high Reynolds numbers (cf. figure 3.6d), the calculated values are within the range of the error bars of the measurement values. The good agreement between our kinematic DNS and the laboratory experiment shall motivate some detailed investigations in the following chapter which is dedicated to the kinematic simulations. However, as the overpredicted forces at small distances show that the deflection of the flow is not negligible, we then proceed to the investigation of the flow deflection in chapter 5.

4. Kinematic regime

We start our investigation with the case when the Lorentz force is too weak to influence the flow. This kinematic regime is of considerable practical importance since in most metallurgical applications the influence of the Lorentz forces is indeed weak. Typically, the influence is describes by the electromagnetic interaction parameter $N = Ha^2/Re$. More specifically, with Reynolds numbers of the order 10^5 and Hartmann numbers of the order 10^2 one obtains $N \approx 0.1$ which demonstrates that the inertial forces dominate over the Lorentz forces in metallurgical flows.

4.1. General properties

Our general procedure to obtain $F_x(h, \boldsymbol{m}, Re, Ha)$ is to calculate the velocity of the liquid metal from the Navier-Stokes equation (2.5) without the Lorentz force in which case the computation becomes a purely hydrodynamic problem. The determined velocity field and the given magnetic field are then used to compute the right-hand side of the Poisson equation (2.7). Once this equation has been solved, the eddy currents are obtained from Ohm's law. i.e. $\boldsymbol{j} = -\nabla\varphi + \boldsymbol{u} \times \boldsymbol{B}$. Together with the imposed magnetic field this current distribution is subsequently used to determine the total Lorentz force on the flow and the magnet, i.e.

$$\boldsymbol{F} = \frac{Ha^2}{Re} \int \boldsymbol{j} \times \boldsymbol{B} \, dV. \tag{4.1}$$

Hence, the computation of $F_x(h, \boldsymbol{m}, Re, Ha)$ can be regarded as a post-processing procedure applied to a purely hydrodynamic velocity field.

In the framework of the kinematic approximation, several properties of $F_x(h, \boldsymbol{m}, Re, Ha)$ can be derived without any numerical computation. Since the flow is unaffected by the magnetic field, the integral in equation (4.1) depends only on the Reynolds number and on the geometry of the magnetic field which is in turn determined by the distance parameter and the orientation of the dipole. Hence, F_x is a product of a prefactor Ha^2/Re and a function that depends only on $\boldsymbol{m}$, h and Re – through the shape of the velocity profile. This shows, that the magnitude of the electromagnetic drag is primarily controlled by the electromagnetic interaction parameter $N = Ha^2/Re$. This property of F_x together with the fact that N is independent of the viscosity of the liquid leads to the useful conclusion that F_x of our fluid can be directly compared with F_x of a solid electrically conducting bar that has been comprehensively studied by Kirpo *et al.* (2011).

The comparison of electromagnetic drag forces between the fluid and a moving solid body is particularly convenient if we consider a situation in which the magnetic moment $\boldsymbol{m}$ of the dipole is fixed, whereas its distance h from the fluid can be changed. In this case the magnetic field at $x = y = 0$, $z = 1$ depends on the distance through the relation $B_{max} = \mu_0|\boldsymbol{m}|/(2\pi\kappa h^3)$ with $\kappa = \sqrt{k_x^2 + k_y^2 + 4k_z^2}$ which can be derived from the magnetic field distribution around a point dipole (cf. equation 2.1). Then the Hartmann number varies as

$$Ha = \frac{M}{2\pi h^3}. \tag{4.2}$$

Here, the parameter

$$M = \frac{\mu_0 m}{L^2}\sqrt{\frac{\sigma}{\rho\nu}} \tag{4.3}$$

can be regarded as an intrinsic Hartmann number for a magnetic dipole that is independent of its distance from the fluid. M represents the Hartmann number which a magnetic dipole with dipole moment $\boldsymbol{m}$ would create in a fluid if it were located at a distance L from it. With this step done, the electromagnetic drag force can be rewritten in the form

$$F_x = \frac{M^2}{Re}c_{Re}(\boldsymbol{m}, h). \tag{4.4}$$

The function $c_{Re}(\boldsymbol{m}, h)$ depends only on the Reynolds number (through the shape of the mean velocity profile) and on the distance parameter plus the dipole orientation (through the shape of the magnetic field). Notice that M^2/Re is independent of the viscosity as is the case with Ha^2/Re.

The velocity profile of a laminar flow in a square duct can be expressed analytically (Pozrikidis, 1997). Its shape is independent of the Reynolds number and it is linearly stable for arbitrary values of Re (Tatsumi & Yoshimura, 1990). Hence, $c_{Re}(\boldsymbol{m}, h)$ is independent of Re for the laminar flow. This value will be denoted as $c_0(\boldsymbol{m}, h)$ and will be discussed in the next section. By contrast, if the flow is turbulent, the profile of its mean velocity depends on Re and F_x is governed by the dependence of c_{Re} on Re. This function will be discussed in section 4.3. The case of a translating solid body (Kirpo et al. 2011) can be formally considered as a flow with $Re \to \infty$ and is hence described by c_∞. The scaling of the electromagnetic drag force in the kinematic case can thus be summarized as follows:

$$F_x = \frac{M^2}{Re}c_0(\boldsymbol{m}, h) \quad \text{for laminar flow} \tag{4.5}$$

$$F_x = \frac{M^2}{Re}c_{Re}(\boldsymbol{m}, h) \quad \text{for turbulent flow} \tag{4.6}$$

$$F_x = \frac{M^2}{Re}c_\infty(\boldsymbol{m}, h) \quad \text{for solid body translation} \tag{4.7}$$
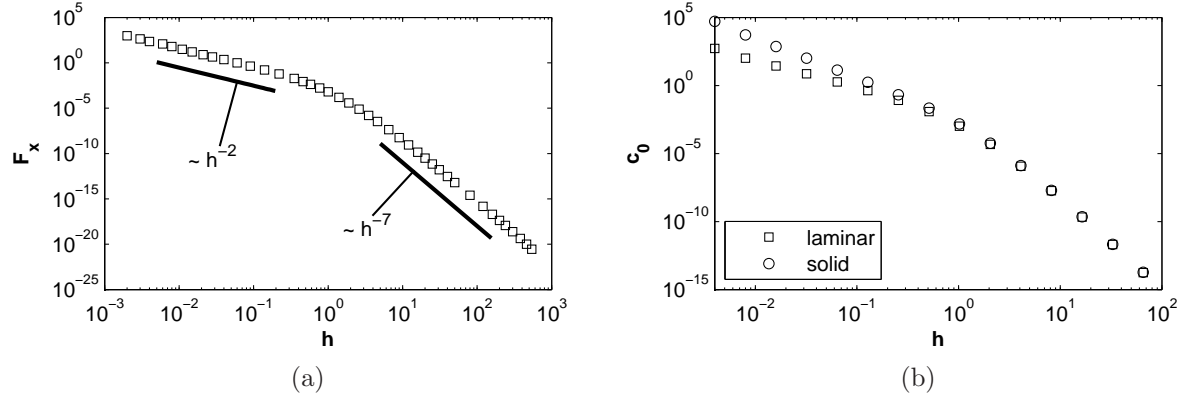
Figure 4.1.: Scaling of the electromagnetic drag force in the kinematic regime for a vertical oriented dipole: (a) F_x as a function of h for an arbitrarily chosen $Re=2000$ and $M = 461.052$ as obtained from DNS. (b) $c_0(\boldsymbol{e}_z, h)$ as defined by equation (4.5) together with c_∞. For $h \ll 1$ a power law of the form $c_0(\boldsymbol{m}, h) \sim h^{-2}$ has been found. The scaling for large distances ($h \gg 1$) can best be estimated by a $F_x \sim h^{-7}$ dependence. For distances roughly equal to the characteristic length scale – the regime covered by experiments (cf. section 3.3)– the scaling can be described by a Batchelor fit as discussed in the text.

4.2. Laminar flow

Figure 4.1a shows the electromagnetic drag force F_x as a function of the distance parameter h as computed for the arbitrarily chosen values $Re = 2000$ and $M = 461.052$ from the laminar velocity profile. For convenience, the computation is performed using the DNS-code rather than the analytic formula for the laminar profile because the computation of F_x is already integrated into the DNS-code. As one would intuitively expect, the electromagnetic drag is a monotonically decreasing function of the distance between the liquid metal and the magnetic dipole. A closer inspection of the curve reveals that there are three regions, namely the short-distance region $h \ll 1$, the long-distance region $h \gg 1$ and the transition region $h \sim 1$.

In the short distance region, we find a scaling according to $F_x \sim h^{-2}$ whereas the long-distance region is characterized by $F_x \sim h^{-7}$. To understand these scaling laws, we refer to figure 4.1b where $c_0(\boldsymbol{m}, h)$ is compared to the solid-body case described by $c_\infty(\boldsymbol{m}, h)$. Notice that F_x and c_{Re} have the same h-dependence. The h^{-7}-scaling in the long-distance range is the same as the scaling in the case of the solid bar. From this agreement we conclude that for large distances the small-scale changes of the velocity over the cross section of the duct are not important and the fluid interacts with the dipole as if it were a solid bar moving with the mean velocity. The following derivation[1] of the -7-power law is therefore given for the simpler case of a solid body motion.

The decay of the Lorentz force with the power h^{-7} at large distances is more rapid than

---

[1]The derivation is based on an idea by André Thess and was completed by Thomas Boeck and the author.

one would expect from a simple estimate. The straightforward estimation would involve $F_x \sim B_0^2 V$ based on a characteristic value B_0 of the magnetic field and an effective volume V of the bar affected by the magnetic field. With the dipole field decaying according to $B_0 \sim h^{-3}$ and $V \sim 4h$ one would obtain $F_x \sim h^{-5}$. The decay with h^{-7} is therefore not obvious. It can be explained with the help of asymptotic expansions in the small parameter $\varepsilon := 1/h$. Alternatively, the asymptotic approach can be regarded as a long-wave expansion along the length of the bar.

The goal of our asymptotic approach is to estimate the Lorenz force F_x for $h \gg 1$ acting on the dipole with an arbitrary orientation. The solution is based on the rescaled coordinates $x = h\hat{x}$, $y = \hat{y}$, $z = \hat{z}$, whereby one can exploit the slow variation in x when the parameter ε tends to zero. The quantities of interest, i. e. $\boldsymbol{B}$, φ, $\boldsymbol{j}$, $\boldsymbol{F}$, are then represented as regular perturbation expansions in the small parameter ε, e. g. for the magnetic field

$$\boldsymbol{B}(\hat{x}, \hat{y}, \hat{z}) = \boldsymbol{B}^0(\hat{x}) + \varepsilon \boldsymbol{B}^1(\hat{x}, \hat{y}, \hat{z}) + \varepsilon^2 \boldsymbol{B}^2(\hat{x}, \hat{y}, \hat{z}) + \ldots . \tag{4.8}$$

The superscripts denote the order of approximation for every term. The expressions for $\boldsymbol{B}^0$ are given in the appendix A. The velocity field is constant and therefore independent of ε.

The drag component of the Lorentz force is then given by

$$F_x(\hat{x}, \hat{y}, \hat{z}) = F_x^0(\hat{x}, \hat{y}, \hat{z}) + \varepsilon F_x^1(\hat{x}, \hat{y}, \hat{z}) + \varepsilon^2 F_x^2(\hat{x}, \hat{y}, \hat{z}) + \ldots .$$

We would like to limit ourselves by three leading terms of the Lorentz force F_x series expansion:

$$F_x^0 = \frac{Ha^2}{Re} \int \left(\boldsymbol{j}^0 \times \boldsymbol{B}^0 \right)_x dV, \tag{4.9}$$

$$F_x^1 = \frac{Ha^2}{Re} \int \left(\boldsymbol{j}^1 \times \boldsymbol{B}^0 + \boldsymbol{j}^0 \times \boldsymbol{B}^1 \right)_x dV, \tag{4.10}$$

$$F_x^2 = \frac{Ha^2}{Re} \int \left(\boldsymbol{j}^2 \times \boldsymbol{B}^0 + \boldsymbol{j}^1 \times \boldsymbol{B}^1 + \boldsymbol{j}^0 \times \boldsymbol{B}^2 \right)_x dV. \tag{4.11}$$

Thus, the evaluation of F_x requires computation of these six integrals. Each of them is considered in detail in the appendix. We only present the key steps of the procedure at this point.

The Laplace equation, $\Delta\varphi = 0$, reduces to

$$\frac{\partial^2 \varphi^0}{\partial \hat{y}^2} + \frac{\partial^2 \varphi^0}{\partial \hat{z}^2} = 0$$

for the leading term φ^0 of the electrical potential. This is easily solved by $\varphi^0 = zB_y^0 - yB_z^0 + const$. Therefore $\boldsymbol{j}^0 = 0$ and all integrals containing the current $\boldsymbol{j}^0$ vanish. The first-order term $\boldsymbol{j}^1$ of the current does not vanish. We can determine its components in the yz-plane by a stream function representation. There is no contribution to the Lorentz
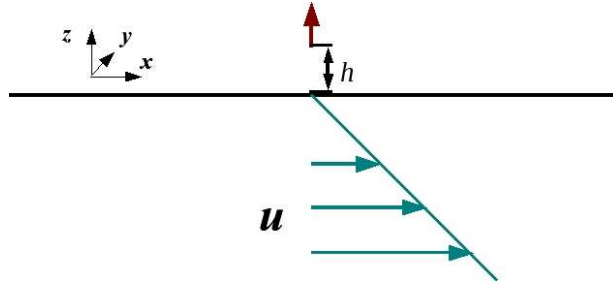
Figure 4.2.: Sketch of the Couette flow with magnetic point dipole in distance h of the surface, as considered for the derivation of the h^{-2}-power law for short distances.

force from such a planar current distribution interacting with a field $\boldsymbol{B}^0$ that is constant on each yz-plane, i. e. $\int \left(\boldsymbol{j}^1 \times \boldsymbol{B}^0\right)_x dV = 0$. However, there is a contribution from the interaction with $\boldsymbol{B}^1$ by

$$\varepsilon^2 \int \left(\boldsymbol{j}^1 \times \boldsymbol{B}^1\right)_x dV = -\frac{15^2 \cdot 2.253}{2^{20}\pi h^7}(5k_x^2 + 7k_z^2). \tag{4.12}$$

For the last remaining integral, we use the continuity equation, $\nabla \cdot \boldsymbol{j} = 0$, and the result for φ^0 to get

$$\varepsilon^2 \int \left(\boldsymbol{j}^2 \times \boldsymbol{B}^0\right)_x dV = -\frac{15}{2^{16}\pi h^7}(35k_x^2 + 8k_y^2 + 57k_z^2). \tag{4.13}$$

By combining all evaluated integrals, we see that the leading term of the Lorentz force is given by

$$F_x = -\frac{Ha^2}{Re}\frac{15}{2^{16}\pi h^7}\left(45.561k_x^2 + 8k_y^2 + 71.785k_z^2\right). \tag{4.14}$$

We have thereby demonstrated that $F_x \sim h^{-7}$ when $h \gg 1$. The asymptotic theory agrees with the values obtained numerically for large h. The observed differences are less then 2% for all orientations of the dipole.

In the short distance region ($h \ll 1$), the scaling behavior $c_0 \sim h^{-2}$ is in contrast to the scaling $c_\infty \sim h^{-3}$ for the solid bar and for a moving unbounded electrically conducting plate (Thess *et al.*, 2007; Votyakov & Thess, 2012). This result implies that a dipole interacts stronger with a solid body than with a flow. This is the case because the magnet is influenced by the metal flow on the magnet side of the duct significantly stronger than by metal on the opposite site. Immediately adjacent to the wall, the velocity is zero and increases approximately linearly in the vicinity of the wall in contrast to the moving bar where the velocity is non-zero at the boundary. We found that the scaling of the electromagnetic drag on the magnet for very small distances can be estimated by investigating the force on a magnet beside a plane Couette flow in a semi-infinite space.[2] We sketch the analysis below, referring the interested readers to the mathematical details in the appendix B.

---

[2]The given derivation was done by Thomas Boeck. It is stated here for completeness as the corresponding DNS were done by the author.

We describe the plane Couette flow by the velocity profile $\boldsymbol{u} = -z\boldsymbol{e}_x$ for $z < 0$ (cf. figure 4.2). In dimensional variables, this means that the shear rate Ω of the Couette flow is given by $\Omega = \overline{u}/L$. The Couette flow extends infinitely into the xy-plane and has its top surface at $z = 0$. The dipole position is given by $\boldsymbol{r}_0 = (0, 0, h)$. It is straightforward to show that the Poisson equation for the electric potential (2.7) then becomes

$$\Delta\varphi = -B_y(x, y, z),$$

where B_y is the spanwise component of the magnetic flux density $\boldsymbol{B}$ of a magnetic dipole given by the non-dimensional expression (2.1). As demonstrated in the appendix B, the Poisson equation (2.7) can be solved using the idea of the mirror charge and the Green's function $G(\boldsymbol{x}, \boldsymbol{x}') = (4\pi|\boldsymbol{x} - \boldsymbol{x}'|)^{-1}$. A lengthy but straightforward calculation yields

$$F_x = -\frac{\kappa}{(4\pi)^2} \frac{M^2}{Re} \frac{\alpha_\varphi + \alpha_u}{h^2} \tag{4.15}$$

with

$$\alpha_\varphi = \int\int\left(\int_{\mathbb{R}^3} G(x, y, 0, x', y', z')B_y(x', y', -|z'|)\,dV' - B_y(x, y, 0)\right)dxdy, \tag{4.16}$$

and

$$\alpha_u = -\int_{z<0} z(B_z^2 + B_y^2)\,dV. \tag{4.17}$$

The coefficients α_φ and α_u reflect the contributions to the Lorentz force from the electric potential and the velocity field, respectively. Their numerically calculated values have been compared to the ones obtained from the numerical solution and found to differ by less than 1% (compare table B.1 in the appendix B). These coeffecient are dependent on the orientation of the dipole. For a vertical oriented dipole equation (4.15) implies $c_{Couette}(\boldsymbol{e}_z, h) = -0.195/h^2$ and is in excellent agreement with the asymptotic behaviour $c_0(\boldsymbol{e}_z, h) \approx -0.192/h^2$ of our numerical solution for the case $h \ll 1$.

We finally note that the behavior in the intermediate range $h \sim 1$ can be described by a Batchelor interpolation formula (Batchelor, 1951) of the form

$$c_0(h) \approx \frac{0.0084 \cdot h^{-2}}{\left(1 + \left(\frac{h}{1.63}\right)^{1.2}\right)^{5/1.2}},$$

which provides a crossover from the short distances to the large distance regime.

4.3. Turbulent flow

Although the laminar velocity profile in a square duct is linearly stable for all Reynolds numbers (Tatsumi & Yoshimura, 1990), finite-amplitude perturbations render the flow
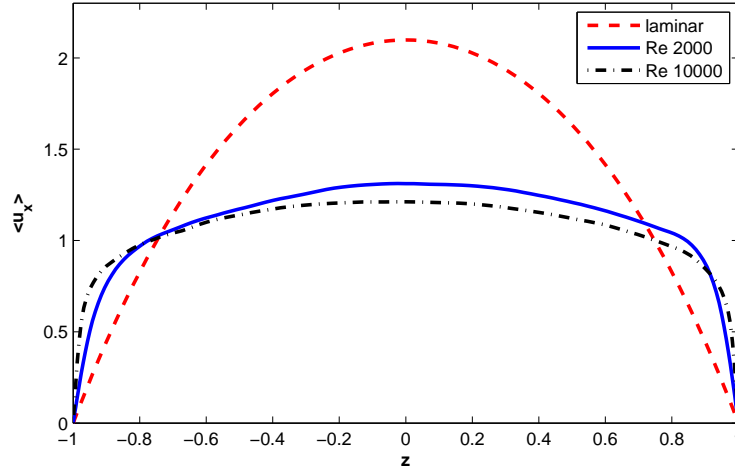
Figure 4.3.: Velocity profile in the middle of the duct at $y = 0$ for laminar and turbulent flow. The gradient at the wall increases with increasing Reynolds number.

turbulent for Reynolds numbers exceeding values of the order of 2000. In the turbulent regime, the Lorentz force acting upon the magnetic dipole is time-dependent. In addition, the interaction paramater $N = Ha^2/Re$ becomes small. Thus, the influence of the magnetic field on the flow is weak which justifies the use of the kinematic approximation. Due to the linearity of the dependence of F_x on the velocity distribution apparent from equation (5.4) the mean Lorentz force and thereby $c_{Re}(\boldsymbol{m}, h)$ is determined by the profile of the mean longitudinal velocity.

The derived analytic formula (4.15) shows a linear dependence of the Lorentz force on the slope of the velocity profile for small distances. One consequence is that the force on the dipole is higher for turbulent than for laminar flow. This is also true for intermediate distances, i.e. $h \sim 1$. A magnetic point dipole has a very localized magnetic field in the sense that it is strongly decaying and thus the total Lorentz force is mostly influenced by fluid motion close to them. When a flow becomes turbulent, while the mean velocity and therefore the Reynolds number are kept constant, the velocities in the vicinity of the wall become higher at the expense of the maximum velocity. Figure 4.3 shows this for $Re = 2000$. Higher velocities in the area of strong magnetic field lead to an increase in the Lorentz force on the dipole, the decrease in force contribution due to a reduced velocity further away from the dipole being negligible. The increase in force solely due to the change in flow behavior is determined by DNS to be between 30% and 60% depending on the Reynolds number.

Figure 4.4a shows the dependence of c_{Re} on the distance parameter h for different Reynolds numbers for the vertical dipole. The profiles for the turbulent flow are obtained as spatial mean from turbulent snapshots as described and validated in section 3.3. As expected, the drag force for the turbulent flow is higher than for the laminar flow. However, it obeys the same scaling laws for the limiting cases $h \ll 1$ and $h \gg 1$. It is also seen that the drag for
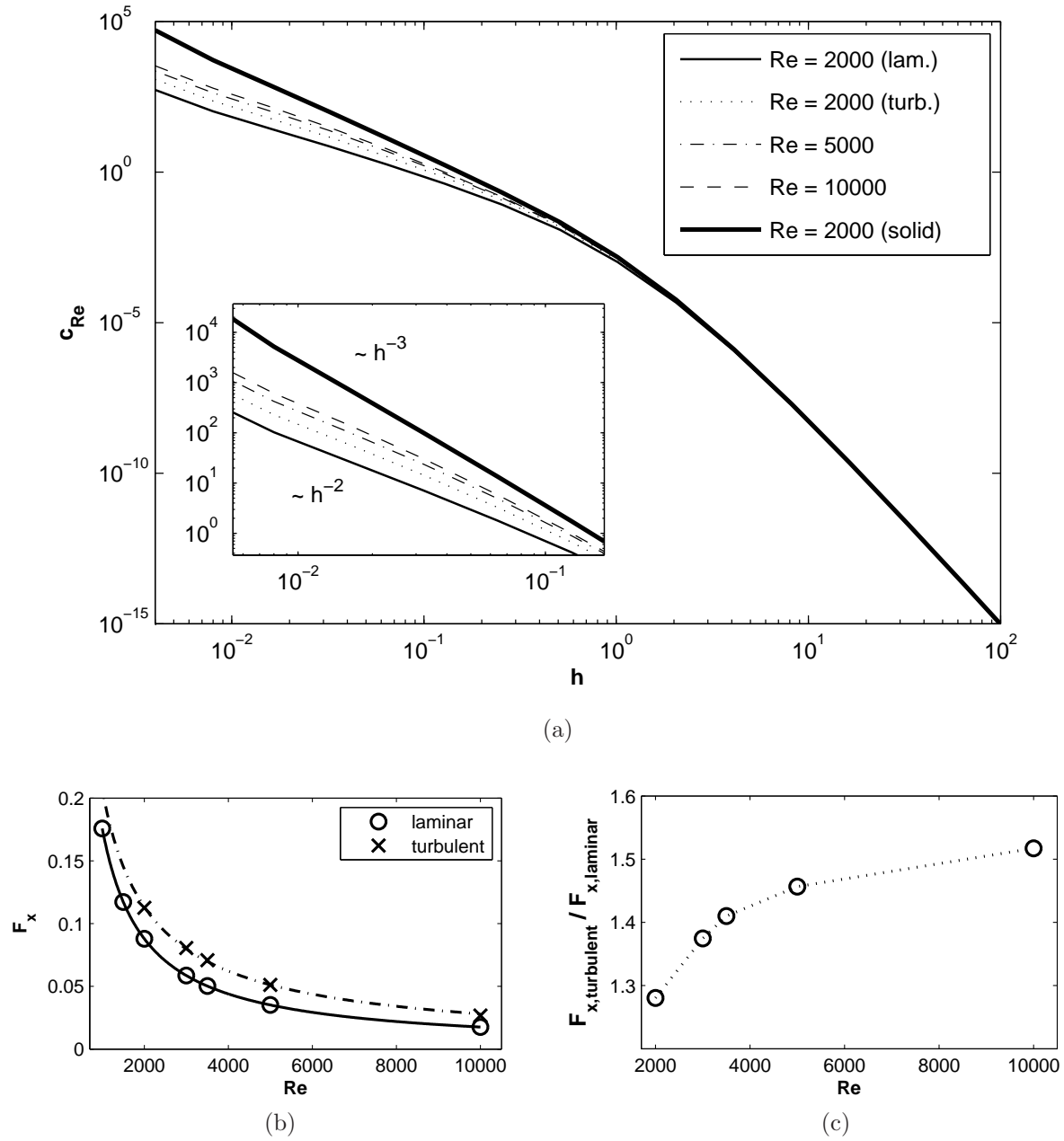
(a)

(b)

(c)

Figure 4.4.: Electromagnetic drag for turbulent flow; (a) $c_{Re}(\boldsymbol{e}_z, h)$ as obtained from DNS for $Re = 2000, 5000, 10000$ in comparison with the curve $c_0(\boldsymbol{e}_z, h)$ for the laminar flow and with $c_\infty(\boldsymbol{e}_z, h)$ for the solid body for a vertical dipole. Inset shows same curves magnified at small distances. (b) F_x for $Ha = 147$ as a function of the Reynolds number at $h = 0.4$, (c) ratio of F_x with turbulent and laminar profile, same data as in 4.4b.

the turbulent flows is always smaller than the drag for the solid body translation.

In figures 4.4b and 4.4c we show the drag force in dependence on the Reynolds number. The forces for turbulent flow are higher than for laminar flow (see figure 4.4b) as could already be seen in figure 4.4a. The obtained factor between the Lorentz forces of laminar and turbulent flows is changing depending on the Reynolds number (figure 4.4c). This change can be explained partly by the differences in the mean velocity profile for turbulent flow. The higher the Reynolds number, the steeper the velocity gradient Ω at the wall becomes (cf. figure 4.3). As pointed out above, this gradient Ω is a linear factor to the Lorentz force in case of small distances. In the presented data in figure 4.4, the distance of the dipole is chosen in the intermediate regime, with $h = 0.4$. Thus the factor does not undergo the same strong rise as the velocity gradients, but is also influenced by the bulk region of the flow profile. These dependencies of the Lorentz force on the flow profile and thus, on the Reynolds number as well as on the distance, complicates the estimation of the Lorentz force for $h \sim 1$.

Before proceeding further to include the effect of the magnetic field on the flow profile in the next chapter, we shortly summaries the findings in this chapter. At close distances, the Lorentz force on a magnetic dipole that is placed beside a laminar liquid metal flow will decrease with increasing distance by $F_x \sim h^{-2}$. At large distances, this behavior changes to $F_x \sim h^{-7}$, with a transition region around $h = 1$. The change from laminar to turbulent flow behavior increases the drag force on the dipole by a factor that is dependent on the Reynolds number and the distance h.

5. Stationary flow at lower Reynolds numbers

In chapter 4, we investigated the behavior of the Lorentz force in the kinematic regime when the flow is not altered by the magnetic field. But it is well known since the pioneering works of Hartmann (1937) and Hartmann & Lazarus (1937) that the Lorentz force modifies the flow field of a liquid metal. This impact of the Lorentz force on flow dynamics must be taken into account if striving for a profound understanding of LFV. Therefore, in the following sections, we will discuss the effect of the Lorentz force on the flow dynamics. As a fundamental case, we start the discussion for flows where fluid inertia is negligible, i.e. at very low Reynolds numbers.

5.1. Mechanisms of flow profile deformation

In the following, we discuss the behavior of the flow in case of low Reynolds numbers. As a first step, we take a closer look at the particular deformation of the velocity profile for Reynolds number 10 and Hartmann number 100 and observe the differences in the deflection depending on the orientation of the magnetic moment of the dipole.

Although being the simplest case, the magnetic field of a dipole is already quite inhomogeneous, obeying a full three-dimensional dependence. This aspect is very important in order to understand the reported effects for a given dipole orientation. Let us consider first the case of a magnetic field, that is directed vertically, i.e. $\boldsymbol{B}||\boldsymbol{e}_z$, and thus perpendicular to the flow direction and perpendicular to the top wall. For this case, the situation is similar to the one in a Hartmann flow (Hartmann, 1937; Hartmann & Lazarus, 1937) where a nearly homogeneous magnetic field is considered. In the Hartmann flow, the electric currents form closed loops inside the duct. This leads to an accelerating Lorentz force at the top and bottom walls and a braking force in the bulk of the flow (cf. figure 1.1 on page 3). For the same reasons, one observes a local Hartmann layer positioned directly below a vertical dipole. Contrary to the classical Hartmann flow configuration, the local Hartmann layer is present on the top wall and practically absent in the rest of the duct cross section. In fact, there are also local Hartmann layers for the other dipole orientations. They will appear whenever a vertical component of the magnetic field is sufficiently strong at a wall. These layers can be observed in figures 5.1 (bottom) and 5.2a. For a spanwise orientation of the dipole they are at each side wall close to the edges of the duct. In case of a streamwise dipole orientation, strong Hartmann layers are found at the centerline right
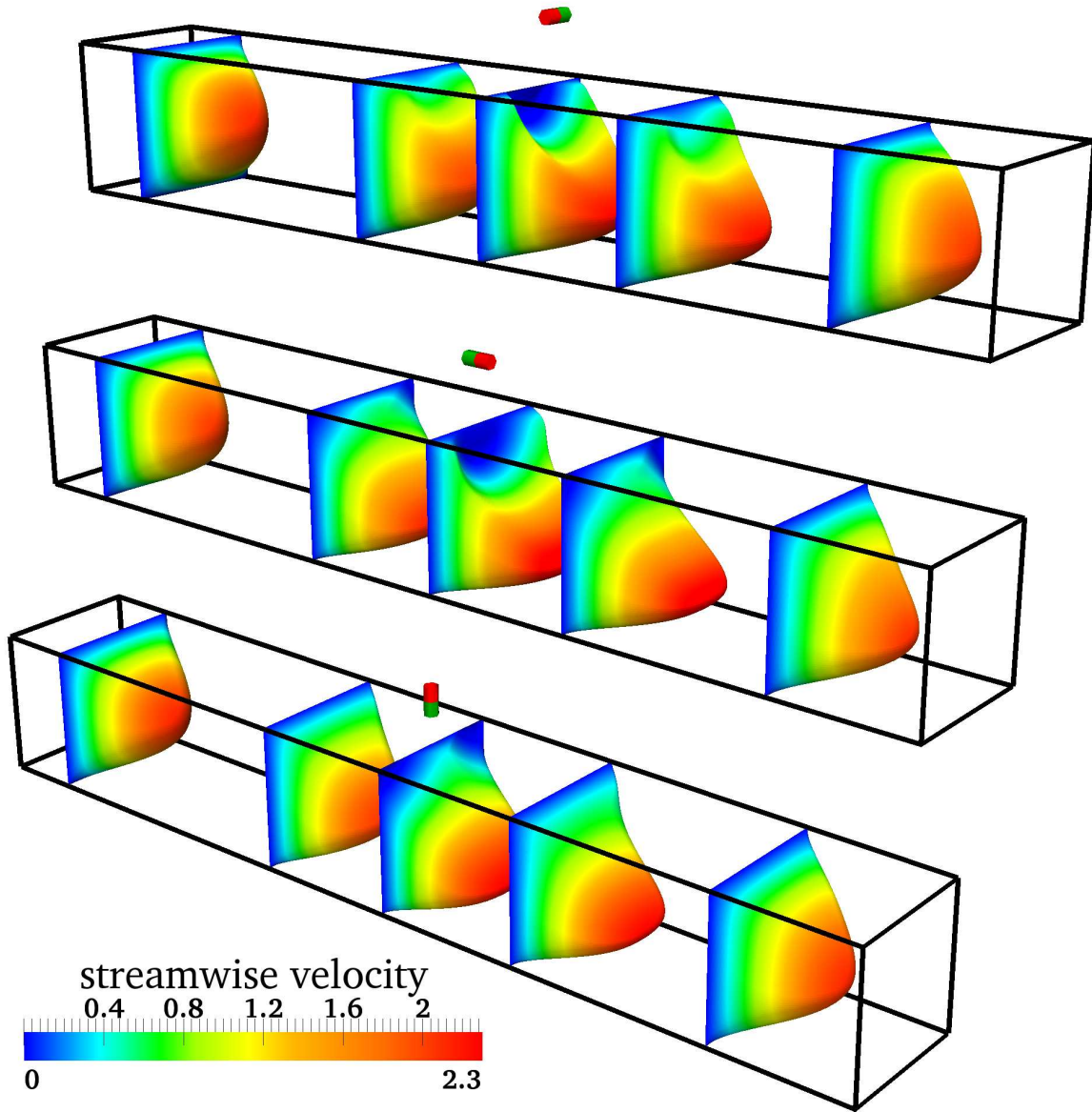
Figure 5.1.: The point dipole as a magnetic obstacle: Contours of streamwise velocity at various positions along the duct illustrate the effect of a point dipole on the duct flow dynamics. From left to right: $x = -0.4, -0.1, 0, 0.1, 0.4$. Total duct length is $5\pi L$ and $Re = 10$, $Ha = 100$, $h = 1.6$. Three different orientations of the dipole are presented: top – spanwise, middle – streamwise and bottom – vertical magnetic moment
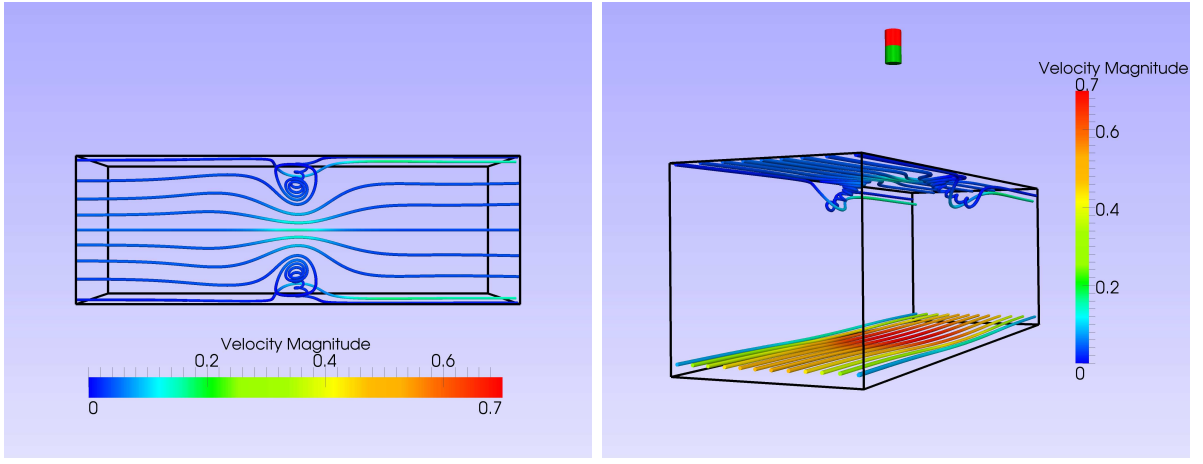
(a) vertical oriented dipole
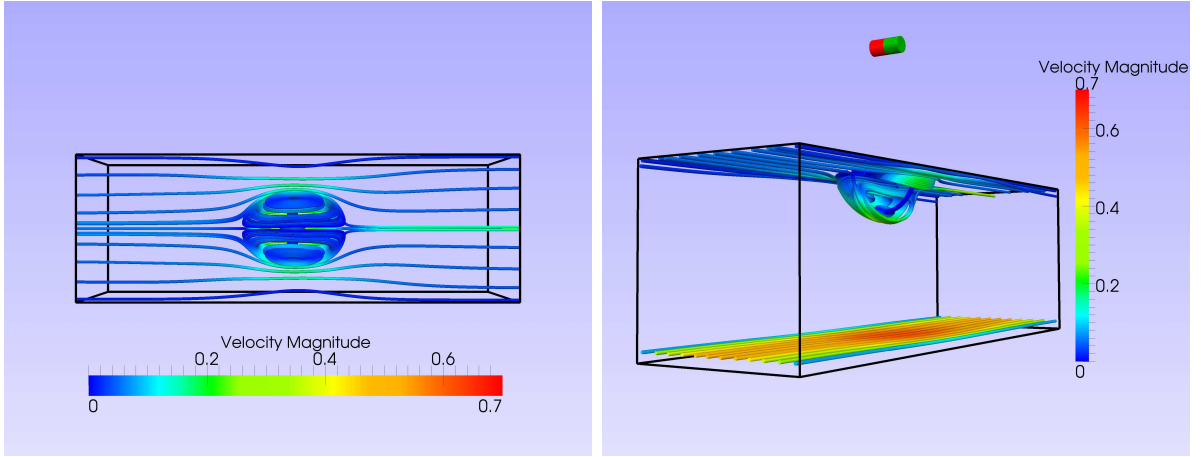
(b) spanwise oriented dipole
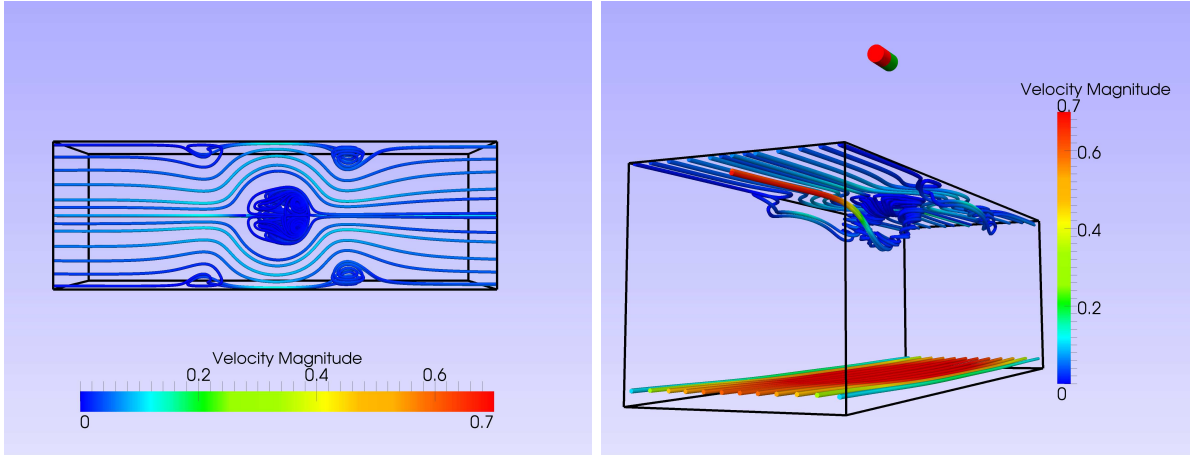
(c) streamwise oriented dipole

Figure 5.2.: Velocity field streamlines for different orientations of the dipole at $Re = 10$, $Ha = 100$, $h = 1.6$. The local Hartmann layer is visible due to higher velocities at the top surface. Vortices and flow structures are three-dimensional. All three configurations are shown from two different perspectives in each case: left is a top view and right a side view.

before and right after the dipole position. Weaker layers are also found at the sides.

Another interesting, but not unexpected, effect is the appearance of a reversed flow in the case of spanwise oriented dipole, i.e. $\boldsymbol{B}||\boldsymbol{e}_y$. The magnetic field is perpendicular to the flow direction and parallel to the top wall. This results in a similar situation as in the so-called Shercliff layers (Shercliff, 1962). Here, the Lorentz force is directed in the opposite direction of the mean flow. If this force is strong enough which is the case when the Hartmann number is sufficiently large, a local flow reversal is observed in figures 5.1 (top) and 5.2b. The resulting vortices in figure 5.2 mark now the areas with strong spanwise magnetic field. This is in fact true for all but one of these vortices.

In the case of streamwise magnetic moment, one may observes five well pronounced vortices at the top as shown in figure 5.2c. The four small vortices in figure 5.2c are produced by Lorentz forces due to the spanwise component of the magnetic field. The bigger central vortex has a different origin. The strongly pronounced vortex directly below the dipole is not generated by the magnetic field in the first place. The main component of the magnetic field in this area is a streamwise component, i.e. $\boldsymbol{B}||\boldsymbol{e}_x$ and thus parallel to the mean flow direction and the top wall. A streamwise magnetic field cannot produce an electric current and therefore the action of the Lorentz force vanishes right below the streamwise oriented dipole. Nevertheless, vortices like the one just discussed were observed for the streamwise oriented dipole at several Reynolds numbers and strong Hartmann numbers. The origin of this vortex may be found in the local Hartmann layers that surround it. The Lorentz forces affect the liquid at the top as follows. The flow is first accelerated at the centerline, then pushed aside to the two Hartmann layers close to the edges and finally again accelerated at the centerline. This forcing leaves the liquid right below the dipole no other possibility, but to swirl as vortex. One has to mention here, that this explanation is more or less descriptive one and that the flow is three-dimensional. Thus, there may be other reasons, that lead to this vortex structure. The three-dimensional nature of the flow, is again revealed in figure 5.2c.

So far, we reported the velocity profiles and the streamlines of the flow. These plots give us information on the flow structures, but not the Lorentz force components in the flow volume. In order to do so, we suggest to quantify the influence of the dipole on the flow with an integral criterion for the balance of Lorentz force, pressure gradient and wall stresses. A balance equation is obtained directly from the Navier-Stokes equation (2.5). We integrate the x-component of (2.5) with respect to y and z and apply the assumptions that the velocity field is smooth, as given in laminar flow and that the flux is normalized and therefore constant. The balance equation follows to

$$\iint_A \partial_x p \, dy \, dz = - \iint_A \partial_x(u_x^2) \, dy \, dz + \iint_A f_x \, dy \, dz \tag{5.1}$$
$$+ \frac{1}{Re} \left(\int_{-1}^1 [\partial_y u_x]_{y=\pm 1} \, dz + \int_{-1}^1 [\partial_z u_x]_{z=\pm 1} \, dy \right),$$

where A is the area of the square duct cross section. It contains on the right hand side a nonlinear advection term (denoted nlt), followed by a Lorentz force term and the contribu-

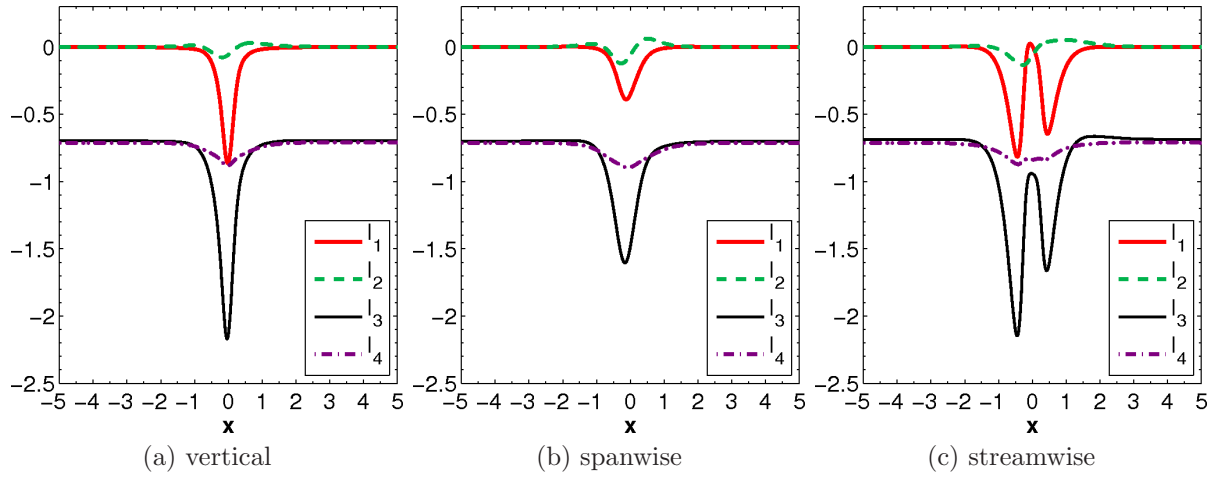(a) vertical   (b) spanwise   (c) streamwise

Figure 5.3.: Terms of the integrated momentum balance as given by equation (5.1) at $Re = 10$, $Ha = 100$, $h = 0.4$. Streamwise profiles for different dipole orientations are shown. The pressure gradient term ($dpdx$) balances the wall shear stresses (τ_w), the nonlinear term (nlt) and the Lorentz force term (f_x).

tion from the wall shear stresses τ_w. The pressure gradient term is found on the left hand side and denoted by $dpdx$. For a homogeneous magnetic field, the integral of the Lorentz force per cross section vanishes. In case of a laminar flow, wall stresses are balanced by the pressure gradient. With an inhomogeneous magnetic field present, the question arises, which hydrodynamic forces balance the appearing Lorentz forces. Figure 5.3 shows all terms of the balance equation for the three dipole orientations.

We can see that the contribution of the Lorentz force is mainly based on the presence of the local Hartmann layers. Therefore, the forces are much stronger for the vertical case than for the spanwise one. The strongest contribution of the Lorentz force comes from the streamwise oriented dipole. Here, two Hartmann layers are clearly visible, ahead and behind the dipole position at $x = 0$. It also becomes clear that it is mainly the pressure gradient which balances the Lorentz force. The nonlinear term is small due to the low Reynolds number of $Re = 10$. In chapter 6, we will come back to this point and will see that the nonlinear term has stronger influences for higher Reynolds numbers. Before increasing the Reynolds number, we shall study the influence of the Hartmann number in the subsequent section.

5.2. Hartmann number dependence

In this section, we want to quantify the effect of the Hartmann number at given Reynolds number. The following scalar integral measure for the quantification of the distortion effect
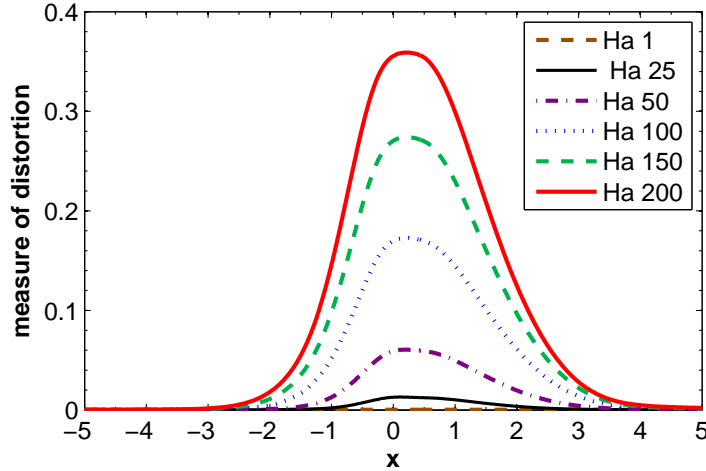
Figure 5.4.: Distortion of the laminar duct flow as a function of the Hartmann number for a low Reynolds number duct flow at $Re = 10$. Deflection of the flow in dependence of Hartmann number as quantified by Δu.

of the laminar profile $\boldsymbol{u}_{laminar}$ (cf. equation (2.4))is suggested:

$$\Delta u(x) = \frac{\iint |\boldsymbol{u} - \boldsymbol{u}_{laminar}| \, dy \, dz}{\iint |\boldsymbol{u}_{laminar}| \, dy \, dz}. \tag{5.2}$$

The quantity $\Delta u(x)$ is a local measure of the deviation of the longitudinal velocity profile from its unperturbed shape. This quantity is confined to the interval $0 \leq \Delta u \leq 2$. The lower bound corresponds to an undeformed velocity profile whereas the upper bound corresponds to a (unphysical) situation where the velocity distribution is an infinitesimally thin jet with infinite velocity located at the wall of the duct.

An example for the distortion is shown in figure 5.4 for Reynolds number of 10 and a wall-normal oriented dipole in a distance $h = 0.4$. The graphs compare the distortion for several Hartmann numbers which are indicated in the legend. Two effects are observed. First, there is almost no distortion of the flow for $Ha < 25$. In this range the flow and the resulting forces behave to a good approximation as a kinematic and thus unperturbed flow. Second, the maximal amplitude of Δu increases approximately linearly with the Hartmann number for $Ha > 25$. Nevertheless, one can assume a saturation of this deformation for very high Hartmann numbers due to the limitation of the geometry. The curves become slightly more symmetric for higher Hartmann numbers, while the total length[1] of the distorted area increases from $Ha = 25$ to $Ha = 200$ only by 10%.

Integrating $\Delta u(x)$ over the length of the duct according to

$$\langle \Delta u \rangle = \int_{inlet}^{outlet} \Delta u(x) \, dx \tag{5.3}$$

---

[1]This length is defined by the distance of the two point with 5% Δu.
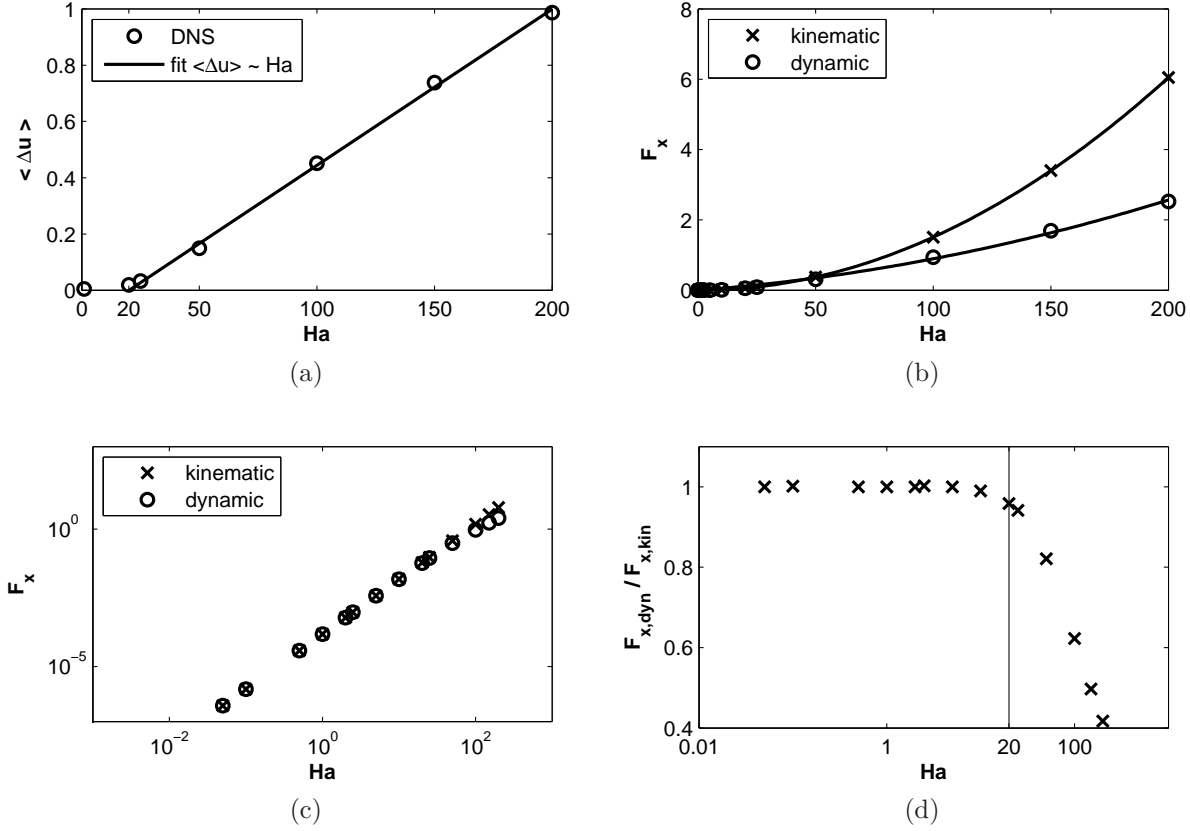
Figure 5.5.: Effect of Ha on the flow dynamics for a point dipole at $Re = 10$ and $h = 0.4$ for a vertical oriented dipole. (a) Deformation parameter as defined by equation (5.3) as a function of Ha. The deformation is negligible for $Ha < 20$ and varies approximately linear with Ha for higher Hartmann numbers. (b) F_x versus Ha in a linear-linear representation for both kinematic and dynamic numerical simulations, (c) same data but in a double-logarithmic representation, (d) ratio of kinematic drag force to dynamic drag force versus Hartmann number. At $Ha = 20$ the ratio becomes less than 0.99.

provides a single non-dimensional number which we call the deformation parameter and use to characterize the flow.

The variation of the deformation parameter with Hartmann number is shown in figure 5.5a. For Hartmann numbers up to approximately $Ha = 20$ the deformation parameter remains virtually unchanged. For higher Hartmann numbers, the flow profile is increasingly modified by the Lorentz force. Recall that the integral forces and torques are defined by

$$\boldsymbol{F} = \int_V \boldsymbol{f} \, dV = \int_V \frac{Ha^2}{Re}(-\nabla\varphi + \boldsymbol{u} \times \boldsymbol{B}) \times \boldsymbol{B} \, dV \,, \tag{5.4}$$

and

$$\boldsymbol{T} = \int_V \boldsymbol{r} \times \boldsymbol{f} \, dV \,. \tag{5.5}$$

(a) wall-normal orientation of the dipole

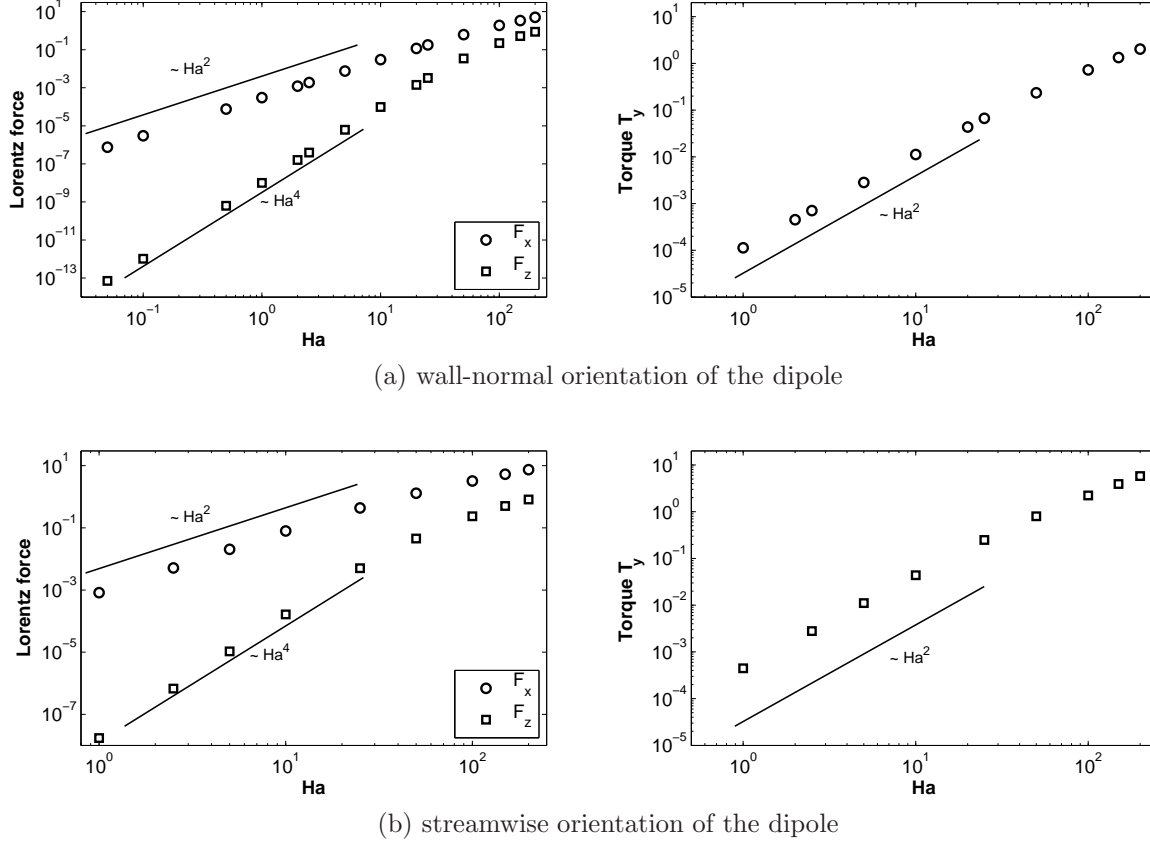(b) streamwise orientation of the dipole

Figure 5.6.: Drag and lift forces and resulting torque as a function of the Hartmann number for (a) wall-normal and (b) streamwise orientation of the dipole.

Figure 5.5b shows the difference between the kinematic and dynamic simulations. The drag force for the dynamic case is higher than for the kinematic. This reflects the fact that in the dynamic case the magnet acts similar to a magnetic obstacle (Votyakov *et al.*, 2007, 2008) thereby increasing the drag. As explained in the previous section, the drag force increases like Ha^2 in the kinematic case. At first glance it may seem that the same Ha^2-scaling applies to the dynamic case since both curves in figure 5.5b seem to increase as the square of the Hartmann number. A more detailed inspection of the curves shows that the latter is not true because in the dynamic case the integral in the definition of F_x also depends on the Hartmann number through the changing velocity profile. Figure 5.5c displays the same result as figure 5.5b but in double-logarithmic representation. It shows that the slope of the curve for the dynamic case becomes slightly lower than Ha^2 for Hartmann numbers exceeding 20. In figure 5.5d, we plot the ratio between the kinematic and the dynamic electromagnetic drag coefficient. In the creeping flow regime the difference between the two approaches becomes relevant for Hartmann numbers of the order 20.

The dependence of the integral forces on Reynolds and Hartmann number was found to be practically the same for all orientations (since directional differences are removed by

the integrals). More interestingly, the absolute values of the forces were found to differ at the same values of Hartmann and Reynolds numbers. The streamwise oriented dipole gave always stronger forces than the wall-normal vertical one. It has to be recalled that the Hartmann number is based on B_{max}, the maximal value of the magnetic field inside the duct, and not on the magnetic moment of the dipole. Thus, in an experiment using a real magnet it will always be found that turning the magnet from vertical to streamwise orientation decreases the forces simply because this rotation will decrease the Hartmann number by a factor of two (see equation (2.1)). In all cases, the spanwise oriented dipole will give the weakest force. The integral torque component behaves in the same way as the forces. Except that the torque is zero for the spanwise dipole due to the symmetry of the problem.

In figure 5.6, we compare the total drag force, the total lift force and the total torque for the wall-normal and the streamwise dipole. We observe that the drag force is higher than the lift force. The data in figure 5.6 reveal two additional power laws which seem to be valid up to $Ha \approx 25$. For higher Hartmann number values, the forces reach a saturation. As expected, one finds that the torque component $T_y \sim Ha^2$. This power law is caused by the fact, that Ha^2/Re is a prefactor of the Lorentz force term in the equations (5.4) and (5.5). The power law for the lift force is found as $F_z \sim Ha^4$. This behavior of the lift force is not obvious. We try to reveal its nature in the following paragraphs.

Let $\boldsymbol{u}$ be a solution to the Navier Stokes equation (2.5) for a given Hartmann and Reynolds number. Similar to a perturbative expansion in weakly nonlinear flows, we divide the velocity field in three parts,

$$\boldsymbol{u} = \boldsymbol{u}_0 + \boldsymbol{u}_1 + \boldsymbol{u}_2 \, . \tag{5.6}$$

Here, $\boldsymbol{u}_0$ is the base flow, $\boldsymbol{u}_1$ describes the distortion of the base flow and $\boldsymbol{u}_2$ stands for the higher-order nonlinear term. The base flow $\boldsymbol{u}_0$ describes to a good approximation the flow with a small interaction parameter Ha^2/Re and at a low Reynolds number. It is supposed to be a steady flow driven solely by the pressure gradient. Thus $\boldsymbol{u}_0$ is the solution of

$$0 = -\nabla p + \frac{1}{Re}\nabla^2 \boldsymbol{u}_0. \tag{5.7}$$

The solution to (5.7) is the laminar flow $\boldsymbol{u}_{lam}$. As it was shown above, the Lorentz forces for a given laminar profile and for the full Navier Stokes equation (2.5) are the same in case of Hartmann and Reynolds numbers below certain thresholds. The present case of $Ha = 25$ and $Re = 10$ satisfies these thresholds and the approximation with a laminar profile $\boldsymbol{u}_{lam}$ gives a good agreement for the drag component of the Lorentz force. However, the lift force is zero for a laminar velocity profile as it was in the kinematic case.

The second term $\boldsymbol{u}_1$ describes the deflection due to the dipole. It is an approximation which holds for small Reynolds numbers. Again, this flow is steady and viscous forces are balanced by the Lorentz force.

$$\frac{1}{Re}\nabla^2 \boldsymbol{u}_1 = -\frac{Ha^2}{Re}(-\nabla \varphi_0 + \boldsymbol{u}_0 \times \boldsymbol{B}) \times \boldsymbol{B} \, . \tag{5.8}$$

It is clear from this equation that the amplitude $u_1 \sim Ha^2$. Again, this contribution of the velocity is not causing a contribution to the lift force which can be shown with the following argumentation based on Stokes flow. Assume that there is a lift force F_z. Then equation (5.8) for $-\boldsymbol{u}_1$ and $-p$ would have to result in an opposite lift force of $-F_z$. Here, F_z will follow and hence the lift force has to vanish. Consequently, the second term of the expansion (5.6) can also not cause the observed lift force. As a further verification, figure 5.7b will show the dependence of the lift force on the Reynolds number. For the creeping flow regime, the lift force is independent of the Reynolds number and the velocity field is completely described by $\boldsymbol{u}_0 + \boldsymbol{u}_1$.

The third part of the decomposition, $\boldsymbol{u}_2$, is the nonlinear part which mainly reflects effects of inertia. This term is an approximation, but presents the realistic flow pattern for moderate Reynolds numbers. Rewriting equation (5.6) to $\boldsymbol{u}_2 = \boldsymbol{u} - \boldsymbol{u}_0 - \boldsymbol{u}_1$ in the Navier-Stokes equation (2.5) for the steady flow case and neglecting all terms of order $O(Ha^4)$ leads to

$$\nabla^2 \boldsymbol{u}_2 = Re \left((\boldsymbol{u}_1 \cdot \nabla)\boldsymbol{u}_0 + (\boldsymbol{u}_0 \cdot \nabla)\boldsymbol{u}_1 \right) . \tag{5.9}$$

From this equation one can estimate, that $u_2/L^2 \approx Re\, u_1 u_0/L \approx Re\, Ha^2\, u_0^2 L$. Thus, $u_2 \approx Re\, Ha^2\, u_0^2 L^3$ which gives rise to the lift force $F_z \approx (Ha^2/Re)u_2$ and thus the expected Hartmann number dependence of Ha^4 for the lift force. We denote in this estimate by L the characteristic gradient variation scale given in units of the duct half width. It is also numerically verified that the lift force vanishes, if the nonlinear term $(\boldsymbol{u} \cdot \nabla)\boldsymbol{u}$ is artificially set to zero. In this case, the flow is symmetric in streamwise direction. This numerical test confirms that the nonlinear term is responsible for non-symmetric pattern in the flow and thus, for the lift force.

5.3. Reynolds number dependence

Beside the Hartmann number, the second control parameter Re will affect the structures of the flow. Following directly from the definition of the Lorentz force (5.4; 5.5), we verify the dependencies $F_x \sim 1/Re$ and $T_y \sim 1/Re$, respectively, in figure 5.7 for several Hartmann numbers. Furthermore, we see that the lift force F_z is constant in the creeping flow regime for $Re < 1$ as already discussed above. In case of higher Reynolds numbers, the lift force decays steeper than $1/Re$.

With increasing Reynolds number the contributions of the nonlinear advection term will increase and manifest in an increasing distortion of the flow. We observe that the distortion in the wake, Δu, measured by equation (5.2) decays as an exponential function $\exp(-\lambda x)$ with respect to the streamwise direction obeying a spatial decay rate λ. This is demonstrated in figure 5.8 for a Hartmann number of $Ha = 100$. The first observation is that the maximum of the distortion is decreasing with the Reynolds number – an effect of the decaying interaction parameter Ha^2/Re. The decay of the maximal value may also be considered as an effect of the nonlinear term. A numeric test case shows, that the values are not decreasing if the nonlinear term is artificially switched off. If the data is presented in a

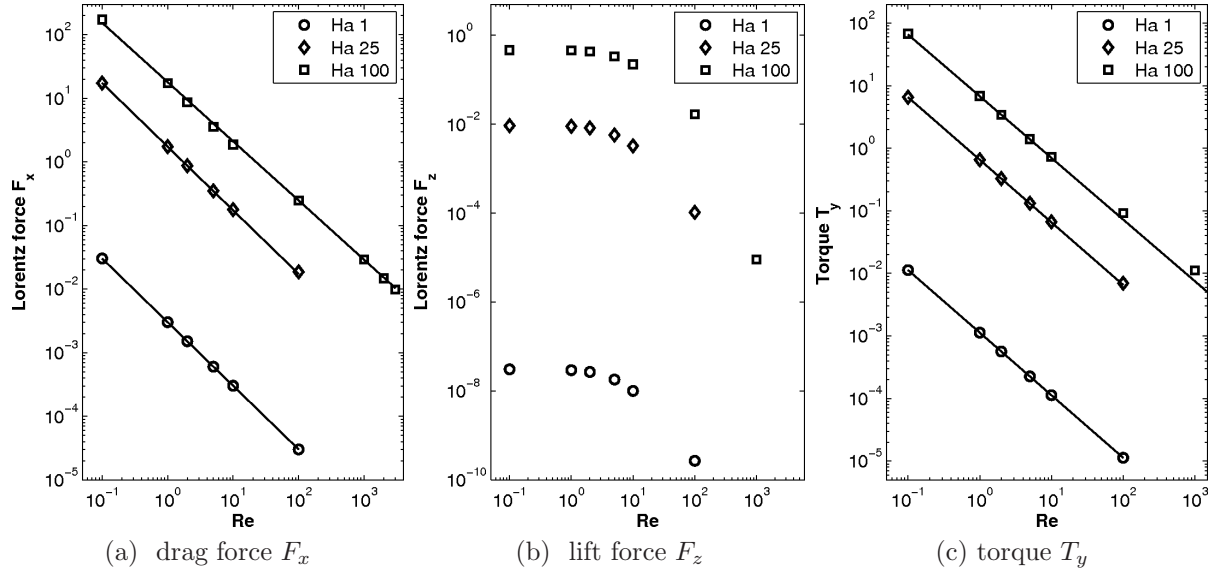(a) drag force F_x (b) lift force F_z (c) torque T_y

Figure 5.7.: Reynolds number dependence of the force components and the torque. Data are for a wall-normal magnetic point dipole at a distance of $h = 0.4$. The dependence $1/Re$ is indicated for the drag component of the Lorentz force and the torque. It can also be seen that the lift component of the Lorentz force is independent of Re for very small values. Data are obtained for several Hartmann numbers as indicated in the legend.

logarithmic scale as in figures 5.8b and 5.8d, the exponential decay is clearly pronounced. When fitting these data with an exponential function, it becomes clearly visible that the spatial decay rate is indirectly proportional to the Reynolds number.

The Reynolds number dependence of the decay rate can be rationalized from the following consideration for steady flow. The Lorentz force term $(Ha^2/Re)(\boldsymbol{j} \times \boldsymbol{B})$ is a localized force term and will not affect the decay in the wake sufficiently far downstream from the dipole position, i.e., we can drop it in the wake. The Navier-Stokes equations therefore simplify to

$$(\boldsymbol{u} \cdot \nabla)\boldsymbol{u} = \frac{1}{Re}\Delta\boldsymbol{u} - \nabla p. \tag{5.10}$$

We now represent the distortion as $\boldsymbol{v} = \boldsymbol{u} - \boldsymbol{u}_{lam}$. It we use this representation, then the dominant term on the left hand side becomes $u_{lam}\partial_x\boldsymbol{v}$. On subtracting the equation for the laminar flow itself we obtain

$$u_{lam}\partial_x\boldsymbol{v} = \frac{1}{Re}\Delta\boldsymbol{v} - \nabla p', \tag{5.11}$$

where the pressure contribution p' serves to maintain incompressibility. If we further approximate the laminar velocity distribution by its mean value $\overline{u}$ we eventually have

$$\overline{u}\partial_x\boldsymbol{v} = \frac{1}{Re}\Delta\boldsymbol{v} - \nabla p'. \tag{5.12}$$
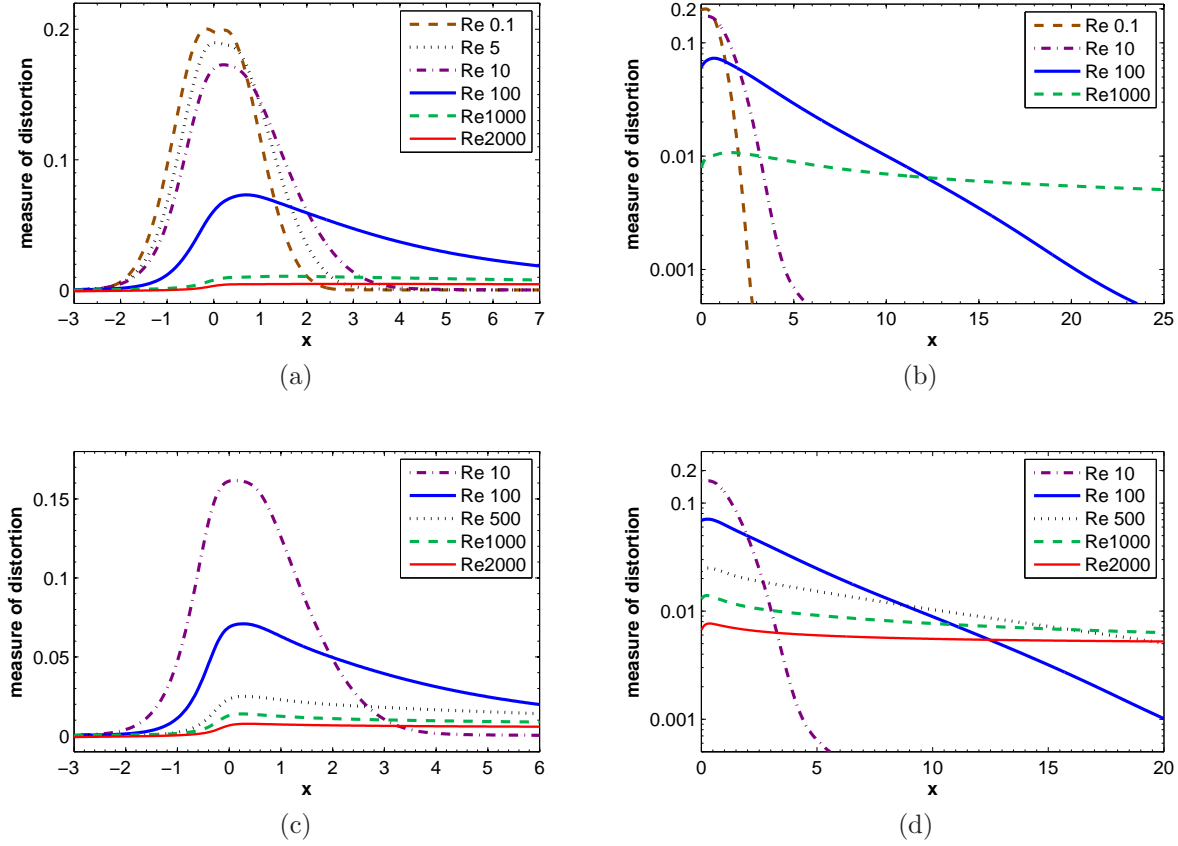
Figure 5.8.: Flow distortion as quantified by equation (5.2) for several Reynolds numbers. In all cases, $Ha = 100$ and $h = 0.4$. Dipole is located at $x = 0$ with (a) wall-normal magnetic moment and (c) spanwise magnetic moment, respectively. Panels (b) and (d) replot the same data on logarithmic-linear axes.

Following usual boundary-layer approximation ideas based on $Re \gg 1$ one can further neglect the second derivative with respect to x in the Laplacian. The problem then effectively reduces to a diffusion problem

$$\partial_t \boldsymbol{v} = \frac{1}{Re} \left(\frac{\partial^2}{\partial y^2} + \frac{\partial^2}{\partial z^2} \right) \boldsymbol{v} \tag{5.13}$$

where we have introduced $t = x/\overline{u}$. Using separation of variables, it is clear that the decay of $|\boldsymbol{v}|$ with t is determined by the largest eigenvalue $-\alpha_1$ of the two-dimensional Laplacian, i. e.,

$$|\boldsymbol{v}| \sim \exp(-\alpha_1 t/Re) = \exp(-\alpha_1 x/Re\overline{u}). \tag{5.14}$$

Therefore, the measure of distortion has to decay similar to $\exp(-x/Re)$. The last steps of the derivation are more heuristic because we eventually had to disregard the remaining pressure term. Justification of this step may be not straightforward, but we suppose that

it is justified because it amounts to a projection on the space of solenoidal functions, which should not interfere with the gist of the argument. We also note that the spatial decay is independent of the orientation of the magnetic dipole. The numerical simulations show that this is the case for $Ha = 100$ and Re reaching from 10 up to 2000 with a accuracy of $\approx 5\%$.

To summaries the results for the lower Reynolds numbers, we explained how different impacts on the flow are observed for different dipole orientations leading to the formation of local Hartmann layers and areas of reversed flow due to strong Lorentz forces. The strength of the forces and their effect on the deflection of the flow in dependence on the Hartmann number was analyzed. The total drag force is found to be proportional to Ha^2 and the total lift force is proportional to Ha^4 in the present Reynolds number regime. When the Reynolds number is increased, we observe that the length of wake is increased. It was also shown why the spatial decay rate is proportional to $1/Re$. In the next chapter we will see how the vortex formation process changes when the dipole triggers a transition to turbulence as the Reynolds number is increased.

6. Time-dependent flow at higher Reynolds numbers

In this chapter, we study time-dependent flow structures which start to appear at Reynolds numbers of about 2000 and higher and for Hartmann numbers above 80. We will observe vortex shedding for cases when the dipole is positioned sufficiently far in at distance of $h = 1.6$ from the top surface of the liquid. For distances smaller than $h = 1.0$ and $Re \leq 3000$, the flow is always stationary. Therefore, we will restrict our study in this chapter to the case of $h = 1.6$ which generates qualitatively new features compared to the last chapter.

6.1. Deformation of the flow

The analysis of the different contributions to the momentum balance (5.1) is shown in figure 6.1 for $Re = 2000$ and $Ha = 100$ for the three dipole orientations: streamwise, spanwise and wall-normal vertical. The deformations of the flow field show a qualitatively similar behavior as the low Reynolds number case from chapter 5. Since the Reynolds number is higher, the nonlinear term contributes now stronger to the momentum balance as visible by the larger magnitude in the figure. The terms of the momentum balance (5.1) reveal that the Lorentz force obeys a qualitatively similar behavior as in the low Reynolds number cases (see also figure 5.3). It is again the pressure gradient, that balances the additional forces which are now produced by the nonlinear term.

The velocity field streamlines for the three cases are shown in figure 6.2. We observe again the formation of local Hartmann layers and vortices as described for low Reynolds numbers in chapter 5. In case of the spanwise oriented dipole a strong vortex in the center of the duct is formed which now becomes time-dependent, i. e., a vortex shedding is initiated. For streamwise and wall-normal oriented dipoles the flow in the wake remains stationary. This could be caused by the local Hartmann layers that stabilize the flow in the range of Reynolds numbers accessible here[1].

It is quite complicated to investigate the criteria for stability as the base flow is dependent on the Hartmann number. The origin of the vortex shedding can hardly be fully described. Thus, a simplified criterion for two-dimensional flow is applied. A possible explanation for the instability and transition to a time-dependent flow is shown in figure 6.2. In the right

---

[1]Maximal Reynolds number is 3000.

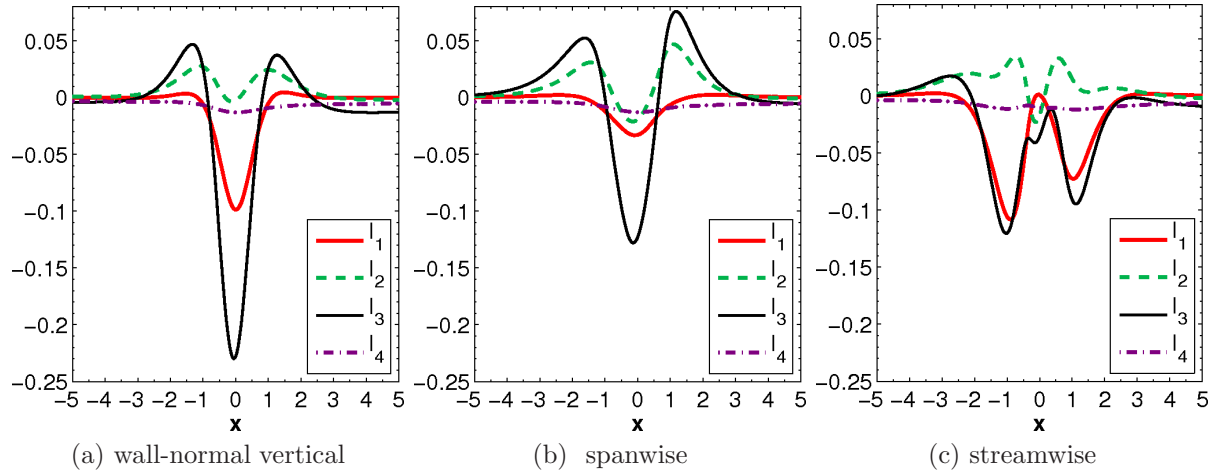(a) wall-normal vertical   (b) spanwise   (c) streamwise

Figure 6.1.: Streamwise variation of the different terms of the cross-section averaged momentum balance (5.1) at $Re = 2000$, $Ha = 100$, $h = 1.6$ for three different orientations of the dipole. The streamwise pressure gradient $dpdx$ balances the walls stresses τ_w, the nonlinear term nlt and the Lorentz force f_x. Since the spanwise case in the mid panel is time-dependent, data are time-averaged over one period.

column of the figure we show five cross sections that contain the magnitude cross-stream gradient of the streamwise velocity which is determined by $\nabla_2 u_x$ where ∇_2 denotes the gradient with respect to y and z directions. Furthermore, the inflection point criterion (Uhlmann & Nagata, 2006) follows with the definition

$$\boldsymbol{n} = \frac{\nabla_2 u_x}{|\nabla_2 u_x|} \tag{6.1}$$

to

$$\nabla_n^2 u_x = 0 \, . \tag{6.2}$$

This criterion was suggested to decide whether a flow may become unstable or not. Contour lines which satisfy (6.2) are added to each of the five cross section plots in figure 6.2. We observe that in case of a spanwise oriented dipole the magnitude of the gradient close to the inflection line is higher compared to the other cases. Thus, the probability of an instability increases. As a consequence, we will restrict our observations and the parameter studies in this chapter to the spanwise oriented dipole, the most relevant case in view of the transition to turbulence.

6.2. Mechanisms of vortex creation

Although the basic mechanism of the deformation were already explained in section 5.1, it is indicated to intensify the understanding for the recent case of interest – the spanwise oriented dipole. The aim of this estimation is to evaluate the resulting main direction

(a) wall-normal vertical dipole

(b) spanwise oriented dipole
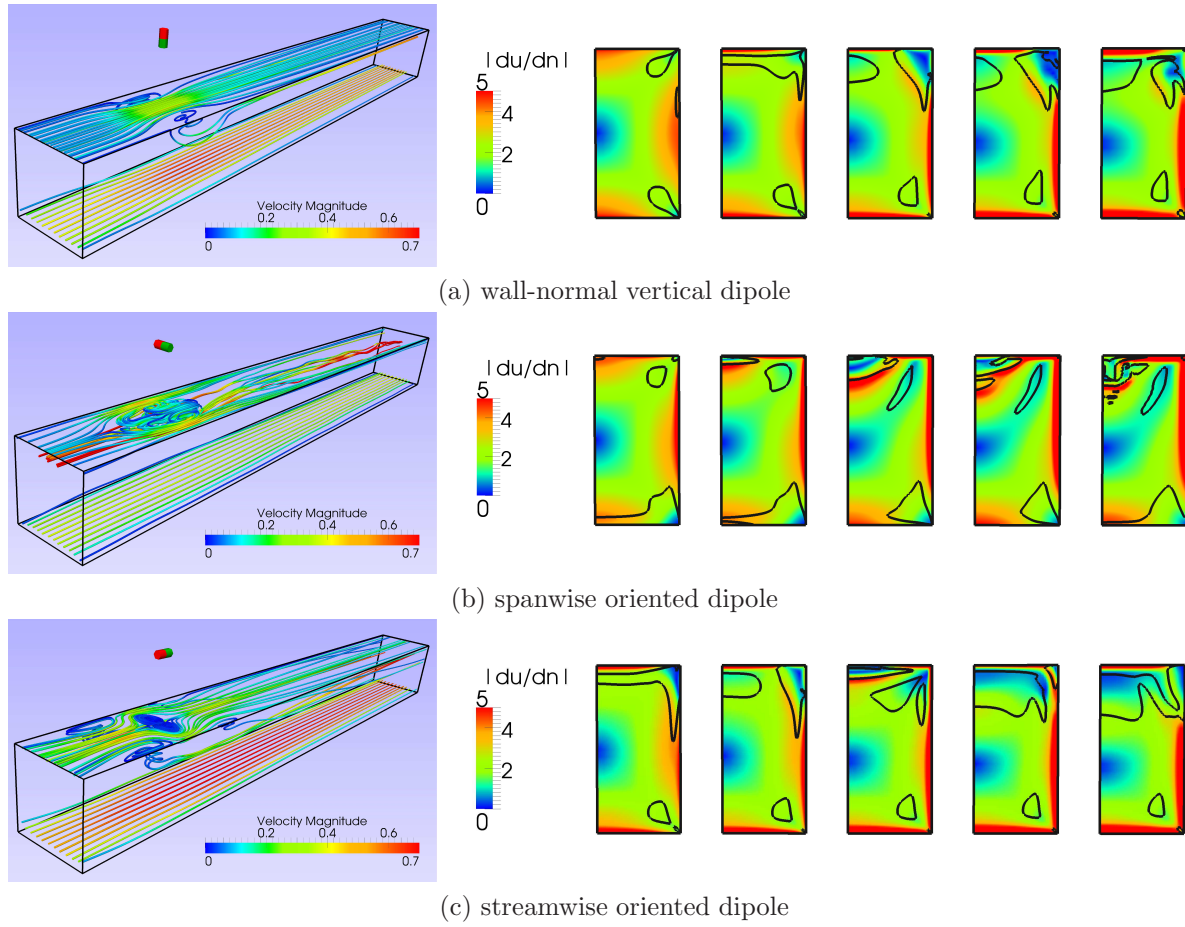

(c) streamwise oriented dipole

Figure 6.2.: Streamlines (left column) and inflection lines (right column) at $Re = 2000$, $Ha = 100$ and $h = 1.6$ for different orientations. Streamlines are shown along top and bottom walls. Color indicates the velocity magnitude. The panels to the right show the corresponding cross sections at streamwise positions $x = -2, -1, 0, 1$ and 2. Due to symmetry only half plane is displayed. The background colours show the magnitude of cross-stream gradient $\nabla_{y,z} u_x$. Black solid lines are the inflection lines as defined in equation (6.2).

of the Lorentz force by means of the right-hand rule. We recall, that the Lorentz force density, i.e. the source of the deflection, is given by

$$\boldsymbol{f} = \frac{Ha^2}{Re}(-\nabla\varphi + \boldsymbol{u} \times \boldsymbol{B}) \times \boldsymbol{B}.$$

The magnetic field is of high magnitude and strongly inhomogeneous in the cross-section directly below the dipole, i.e. at $x = 0$ (figure 6.3). The electric currents can be obtained in a first approximation from the right-hand rule by $\boldsymbol{j} \sim \boldsymbol{u} \times \boldsymbol{B}$. This estimate would not take into account the insulating walls and the continuity equation $\nabla \cdot \boldsymbol{j} = 0$. These constraints force the currents to close inside the duct. Figure 6.3 shows therefore streamlines of the
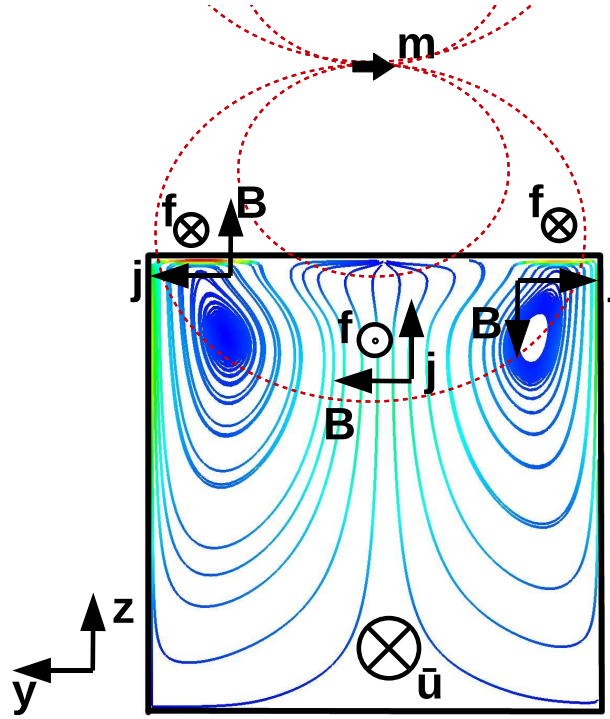
Figure 6.3.: Sketch of principle for vortex shedding in case of spanwise oriented dipole. Streamlines (solid) represent the electric currents in the cross-section with $x = 0$ for Reynolds number $Re = 2000$, Hartmann number $Ha = 100$ and dipole distance of $h = 1.6$. Red dashed lines indicate the magnetic field lines. Arrows denote the local main direction of the magnetic field and the currents. In the Hartmann layers (top corners of the duct) the resulting Lorentz force points then in the same direction as the mean velocity. In the centerline the Lorentz force brakes the fluid and – if strong enough – drives the vortex formation.

currents as obtained form a numerical simulation with $Re = 2000$ and $Ha = 100$. Note, that the currents do not have to close inside a single cross-section. What may look like a sink or a source in figure 6.3 may be explained as a result of the projection on the two-dimensional cross-section. Nevertheless, this snapshot shows that there are two regions where the currents oppose the right-hand rule in order to close the currents loop. These regions are the two top corners. In the rest of the fluid, the currents are largely conform to the right-hand rule.

With the obtained currents, one may now estimate the resulting Lorentz force distribution in the duct. Here the right-hand rule gives a braking force in the bulk of the flow. It should be emphasized that this force is also present in the region directly below the dipole. Here, the magnetic field is most pronounced. For a sufficient high Hartmann number, the resulting Lorentz force may not only brake the fluid but also cause a back flow – the origin of the vortex. In the top corners, the situation is slightly different. As the current
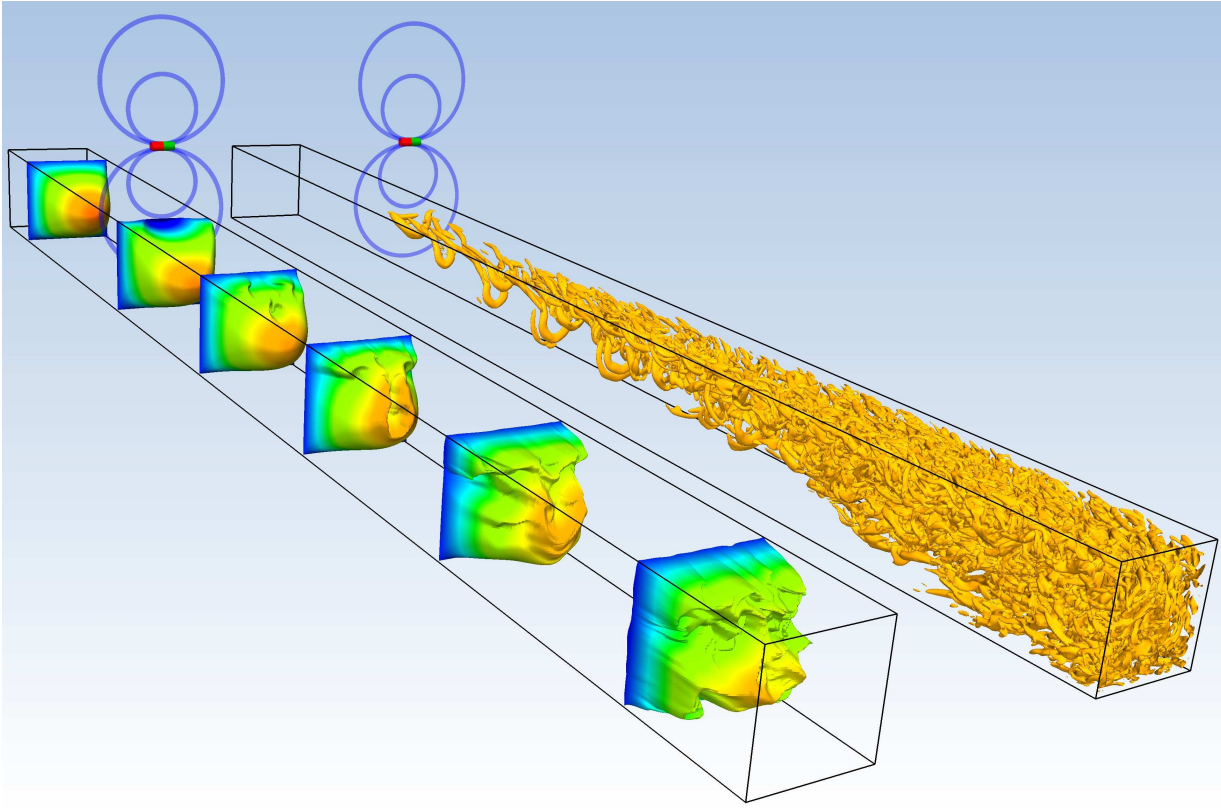
Figure 6.4.: Vortex shedding for a spanwise oriented dipole. Both ducts show the same snapshot for Reynolds number of $Re = 2000$, Hartmann number of $Ha = 100$ and distance $h = 1.6$. The left duct displays instantaneous velocity profiles taken at 6 locations between $x = -10$ and 40. The right figure shows the isocontours of $\lambda_2 = -1$.

loops close here, the resulting Lorentz force accelerates the flow. Thus, the local Hartmann layers are created. These layers are of interest when the influence of the Hartmann number is investigated in section 6.3. In the subsequent paragraph, our concern is on the time-dependent behavior of the vortex, i. e. the vortex shedding, and the resulting structures in the wake.

The vortex shedding generates a turbulent wake which is displayed in figure 6.4. In parallel to several cross sections of the streamwise velocity along the duct isocontours of $\lambda_2 = -1$ are shown where λ_2 is the second largest eigenvalue ($\lambda_1 \geq \lambda_2 \geq \lambda_3$) of the symmetric matrix

$$\Lambda_{ij} = S_{ik}S_{kj} + \Omega_{ik}\Omega_{kj}\,, \tag{6.3}$$

which is composed of the rate of strain and vorticity tensors, respectively, i. e.

$$S_{ij} = \frac{1}{2}\left(\frac{\partial u_i}{\partial x_j} + \frac{\partial u_j}{\partial x_i}\right) \quad \text{and} \quad \Omega_{ij} = \frac{1}{2}\left(\frac{\partial u_i}{\partial x_j} - \frac{\partial u_j}{\partial x_i}\right). \tag{6.4}$$

Negative values, $\lambda_2 < 0$, denote vortex cores (Jeong & Hussain, 1995) which can be clearly

identified as so-called hairpin structures in the figure. They are found close to the top wall in the beginning of the wake before the whole duct is filled with turbulent flow patterns further downstream.

Alternatively, the vortex shedding can be observed by the time signal of the Lorentz force itself. Both, the drag force component F_x and the lift force component F_z, show a periodic sinusoidal time dependence. The temporal modulation of the signal is weak compared to the absolute magnitude (cf. figure 6.8a on page 66). For example, it is $F_x = -3.28 \cdot 10^{-1} \pm 9.39 \cdot 10^{-4}$ and $F_z = 3.98 \cdot 10^{-2} \pm 1.35 \cdot 10^{-3}$ for $Re = 2000$ and $Ha = 100$. Both forces oscillate with a frequency of $3.15 \cdot 10^{-1}$ inverse time units.

The time-dependent structures are shown in figure 6.5 for $Re = 2000$ in four snapshots in time intervals of approximately a quarter of the oscillation time. The figure shows the top view of the duct with the position of the dipole marked as a small black dot. The line of separation marks the region of locally reversed flow, i.e. points with $\partial_z u = 0$. Along this line the flow detaches from the surface. This criterion was also used by Mistrangelo (2011b) to determine the size of the vortex that occurs in a duct with sudden expansion in dependence on the applied homogeneous magnetic field. There, the magnetic field damped the vortex, in contrary to our investigation with the magnetic field being the source of the vortex.

In addition, figure 6.5 displays the structures in the wake. Here, the presented top surface is colored with $\partial_z u$. This gradient reaches its maximal value in the Hartmann layers. It should be marked here, that the Hartmann layers and the vortex are not completely independent of each other. However, the mechanism that describes the interaction of both – and maybe drives the vortex shedding – has still to be determined.

To characterize the three-dimensional structure of the vortices, the λ_2-criterion is used. The pictures on the right-hand side in figure 6.5 show the isocontours of $\lambda_2 = -0.5$. Each period a hairpin vortex structure is produced. It starts at time $t = 0$ with a small vortex that rotates around y in positive direction, i.e. $(\nabla \times \boldsymbol{u})_y > 0$. This vortex is then advected further and surrounded by reversed flow until it is in the position of the dipole at $x = 0$ in time $t = 1/4\,T$, T being the oscillation time. The vortex increases the width of the area of reversed flow as the back flow has to circumvent the vortex. Close to the corners of the duct, the Hartmann layer accelerate the flow. The accelerated fluid is blocked by the thickening of the width of the reversed flow. This creates two extension to the vortex at the sides, that are placed at $x = 0$ in time $t = 1/2\,T$. The vortex then dives below the top surface (time $t = 3/4\,T$). This way, the backflow can move freely and obtains high magnitude at the beginning of the area of reversed flow. This creates then a new vortex at time $t = T$ (which is same as $t = 0$).

The vortices are transported into the wake and are stretched due to inertia and the shear at the top wall. Thereby, their shape forms into a hairpins like structure (Davidson, 2004). After the hairpin is moved into the wake a new vortex is created by the Lorentz force. Hairpins are well known to appear in vortical shear layers at walls (Jeong *et al.*, 1997) and occur in the transition to turbulence in the boundary layer. The development of the wake
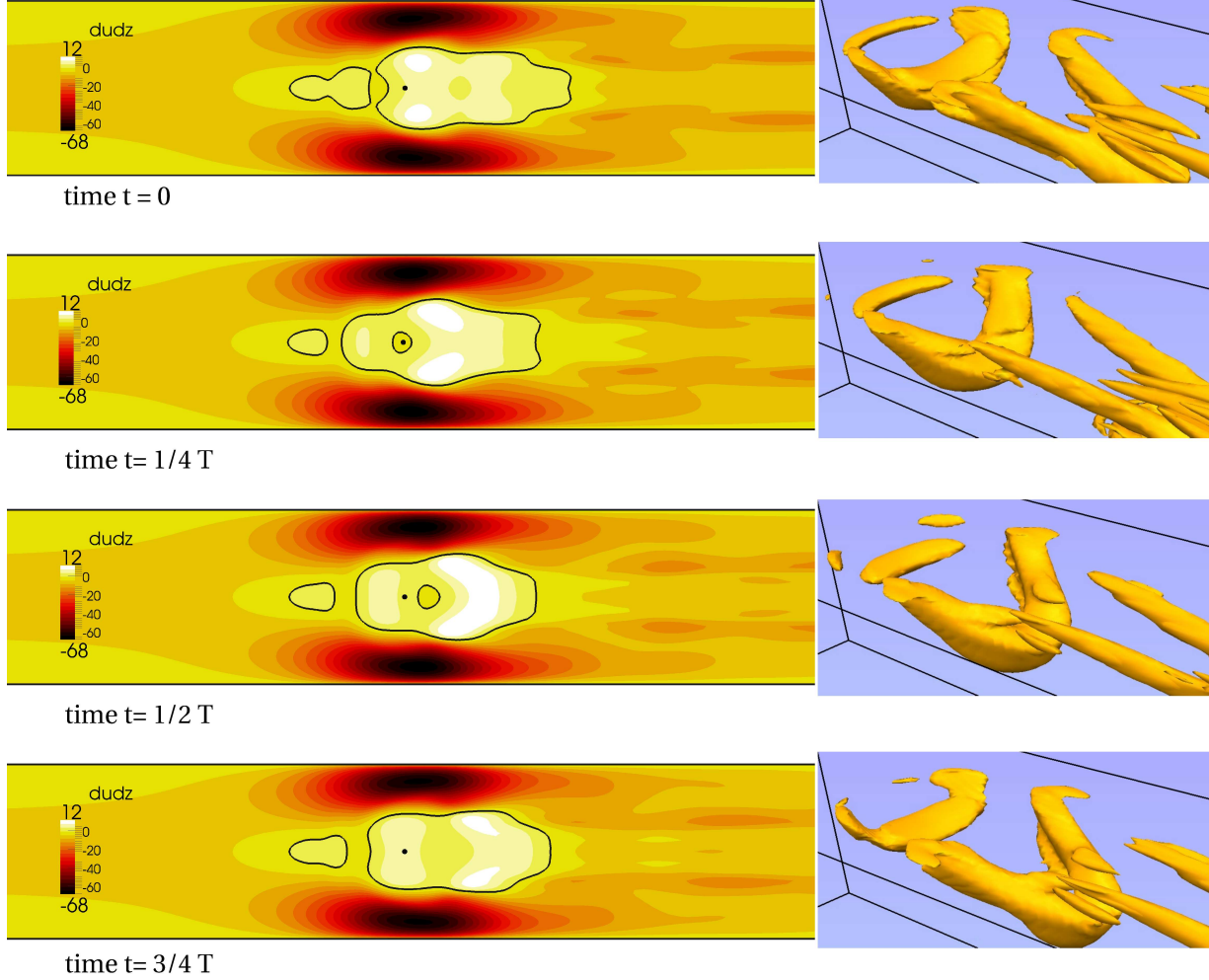
Figure 6.5.: Visualization of the time-dependent structures for $Re = 2000$, $Ha = 100$, $h = 1.6$ and spanwise magnetic moment. Four snapshots are shown every 0.8 convective time units. One oscillation time is 3.168 time units. Left: Top surface with velocity gradient $\partial_z u$. Position of the dipole is indicated with a black dot. The black solid line indicates the line of separation $\partial_z u = 0$. Right: isocontours of $\lambda_2 = -0.5$ at same time. Direction of view in the picture is the same as in figure 6.7.

is determined in the time average with the help of the momentum balance (5.1) in figure 6.6. This figure gives an average over one period, i. e., it shows the mean of 3168 snapshots at intervals of 0.001 time units, for $Re = 2000$ and $Ha = 100$. The well pronounced area of distortion with high Lorentz forces in the interval $-5 < x < 5$ is followed by the region of the vortex shedding $5 < x < 20$. In this region, the flow is periodic in time with the same frequency as in the area of distortion. Here, the time averaged momentum balance resembles the laminar flow as the pressure balances the wall stresses and the contribution of the Lorentz force as well as of the nonlinear term are negligibly small. For $x > 25$ this
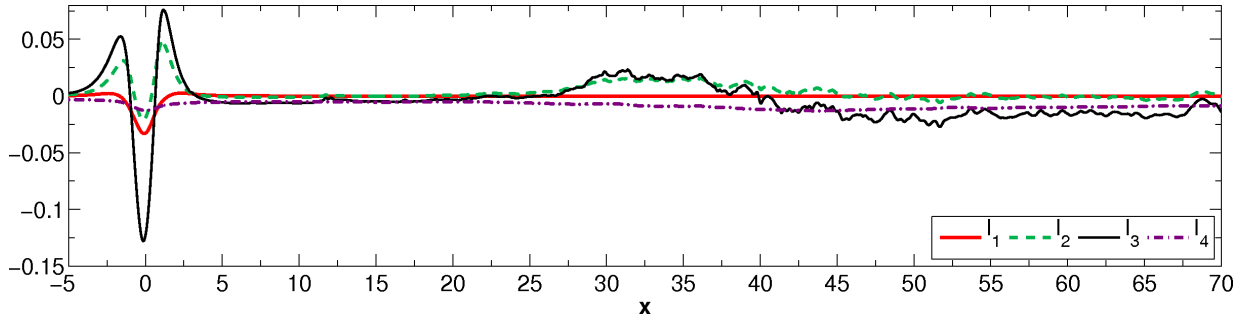
Figure 6.6.: Streamwise variation of the different terms of the cross-section averaged momentum balance (5.1) at $Re = 2000$, $Ha = 100$, $h = 1.6$ for spanwise orientation of the dipole. The data is time-averaged over one period as in figure 6.1b.

changes to a transitional flow, where the nonlinear forces dominate and the wall stresses increase up to a higher constant value as known from turbulent flow. In the beginning of the transitional range, the velocity profiles are found to resemble a turbulent flow but possess a symmetry plane in $y = 0$. The flow is not time-periodic anymore. The time average is not sufficient in the sense that the momentum balance (5.1) that assumes a stationary flow is not fulfilled here. In this region, large scale vortices fill the whole cross-section that break up further downstream. Although the computational domain and the calculation time are too short to obtain statical values for the wake, one may expect a fully turbulent flow after a certain transition length. The calculation for $Re = 3000$ indicates that this length decreases for increasing Reynolds number.

A full parameter study for the Reynolds number dependence cannot be performed due to the limitations in computational resources. Therefore, we restrict the study to three exemplary Reynolds numbers: $Re = 1000, 2000$ and 3000 are examined for fixed Hartmann number of $Ha = 100$. The usage of higher Reynolds numbers would raise the question whether a laminar inflow is still reasonable. The streamlines for the three cases are shown in figure 6.7 (left). The duct flow is stationary for $Re = 1000$, the wake remains laminar. As in the case of $Re = 2000$, that was discussed above, the wake performs a transition for $Re = 3000$. The vortex structure below the dipole position remains similar for all three cases. The λ_2-criterion reveals here the subtle distinctions (see right-hand side of figure 6.7). For $Re = 1000$ only one vortex is pronounced. As described above in case of $Re = 2000$, additional vortices are produced in front of the dipole position, at $x < 0$, and during the vortex shedding. The amount and the strength of these vortical structures is enhanced at $Re = 3000$. This is caused by an increased magnitude of the velocity in the area of reversed flow due to the decreased viscous forces. The principle mechanism of the vortex shedding stays the same as the one explained above. The higher Reynolds number also produces shorter hairpin structures in the wake. Next to the differences in the shape of the flow, the oscillation time is longer. For $Re = 2000$ a oscillation time of 3.168 was calculated, while for $Re = 3000$ it is 3.636 non-dimensional time units.

We conclude from this section that the vortex shedding is a complex mechanism initiated
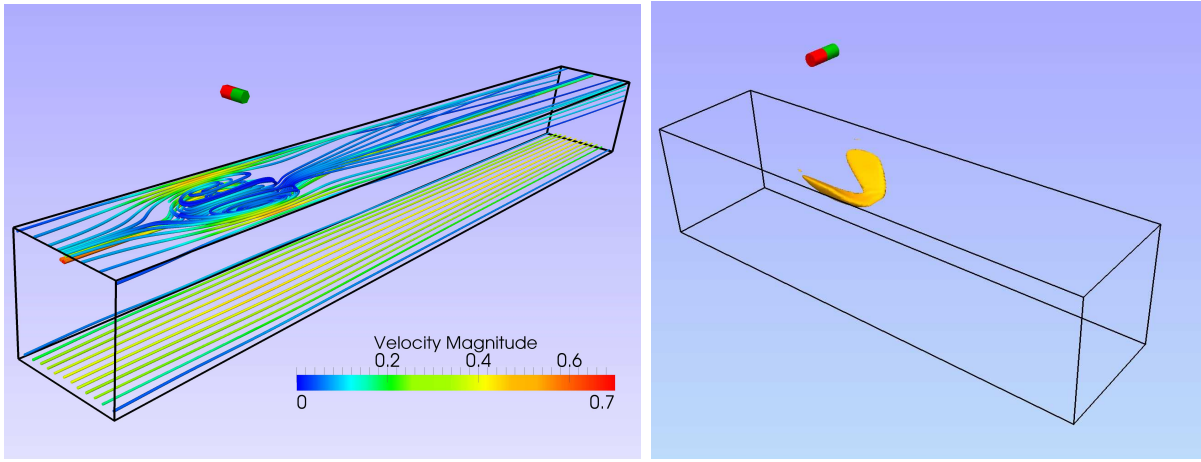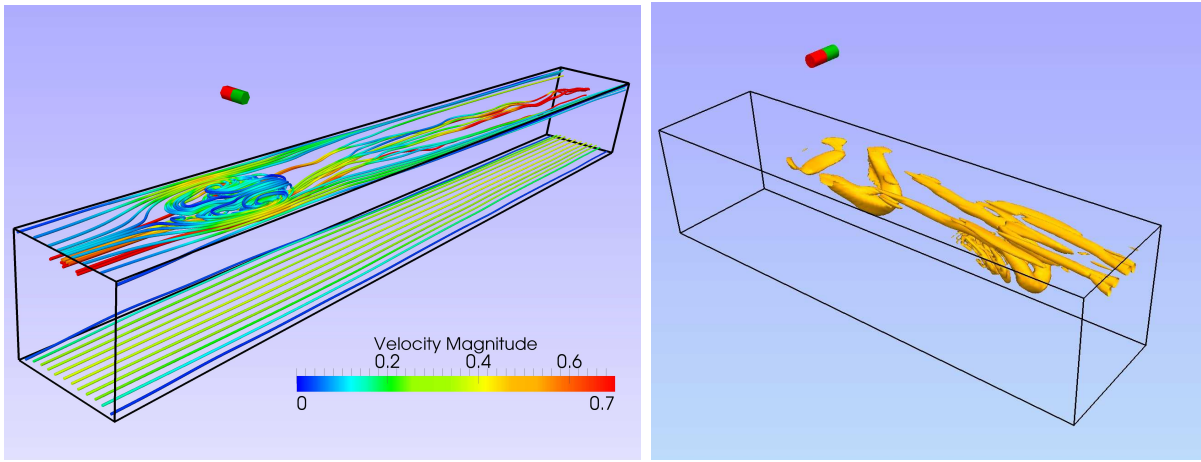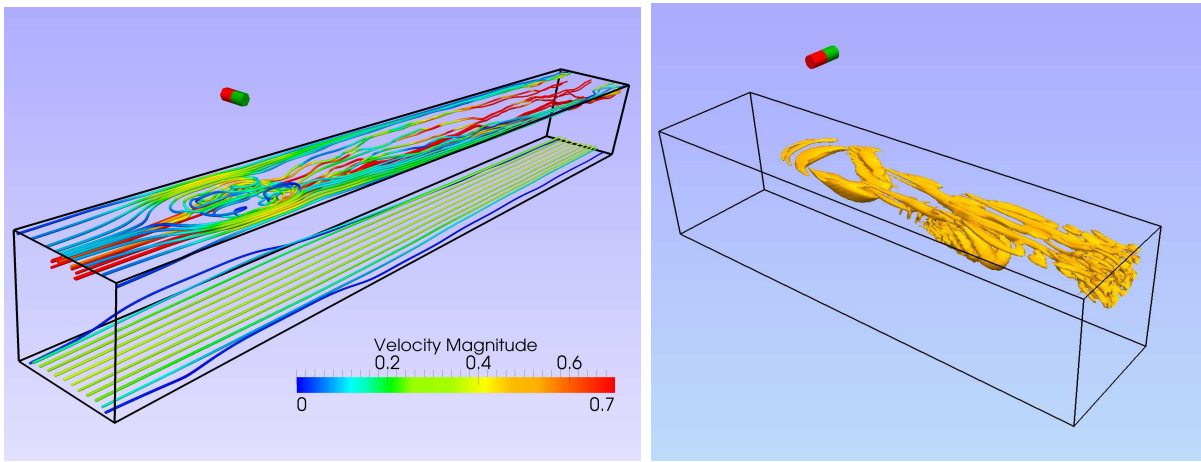
(a) $Re = 1000$

(b) $Re = 2000$

(c) $Re = 3000$

Figure 6.7.: Snapshots of streamlines (left) and isocontours of $\lambda_2 = -0.5$ (right) at different Reynolds numbers for $Ha = 100$ and $h = 1.6$. The dipole is oriented in spanwise direction.

(a) Lorentz force per time

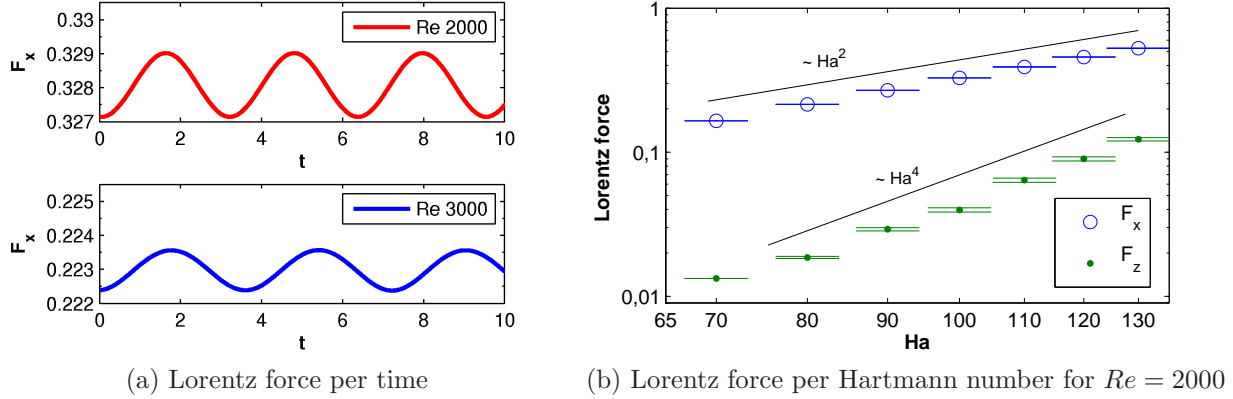(b) Lorentz force per Hartmann number for $Re = 2000$

Figure 6.8.: Time-dependent behavior of the force. (a) Sinusoidal time signal for $Re = 2000$ and $Re = 3000$ with $Ha = 100$ and spanwise dipole in a distance of $h = 1.6$. (b) Lift and drag forces follow approximately the same power laws as in low Reynolds case (figure 5.6). Points are given at the mean value while the vertical bars indicate the range of the variation of the time signal.

by the Lorentz force. The Reynolds number determines, how likely it is that the flow forms vortical structures and transforms the wake into a turbulent flow. As a final step to this parameter study, it remains to investigate the influence of the Hartmann number on the created vortex.

6.3. Hartmann number dependence

To investigate the influence of the Hartmann number, we consider Reynolds number of 2000 and vary the Hartmann number between 25 and 130. For very small Hartmann number, there is almost no deformation of the flow visible. Figure 6.9 shows examples of the streamlines for several Hartmann numbers. For $Ha = 25$, one may already observe the local Hartmann layers, but the Lorentz force is not strong enough to create a flow reversal. Such reversed flow is indicated by the streamlines from $Ha = 50$ and higher. A turbulent wake is observed for $Ha \geq 80$.

The dependence of the Lorentz force on the Hartmann number is shown in figure 6.8b. Here, the mean value of the forces are displayed with points and the range of the variation due to the vortex shedding is marked with tow bars. Similar to the investigations in section 5, one finds the same power laws for the total forces, i.e. $F_x \sim Ha^2$ and $F_z \sim Ha^4$. The vortex shedding does not influence the power law as the oscillations of F_x and F_z are in the order of 1% and 10% of the forces, respectively.

As an additional characteristic the frequency of the vortex shedding can be obtained from the time signal of the force. Regarding the dipole as a magnetic obstacle, allows to compare

(a) $Ha = 25$

(b) $Ha = 50$

(c) $Ha = 70$

(d) $Ha = 80$
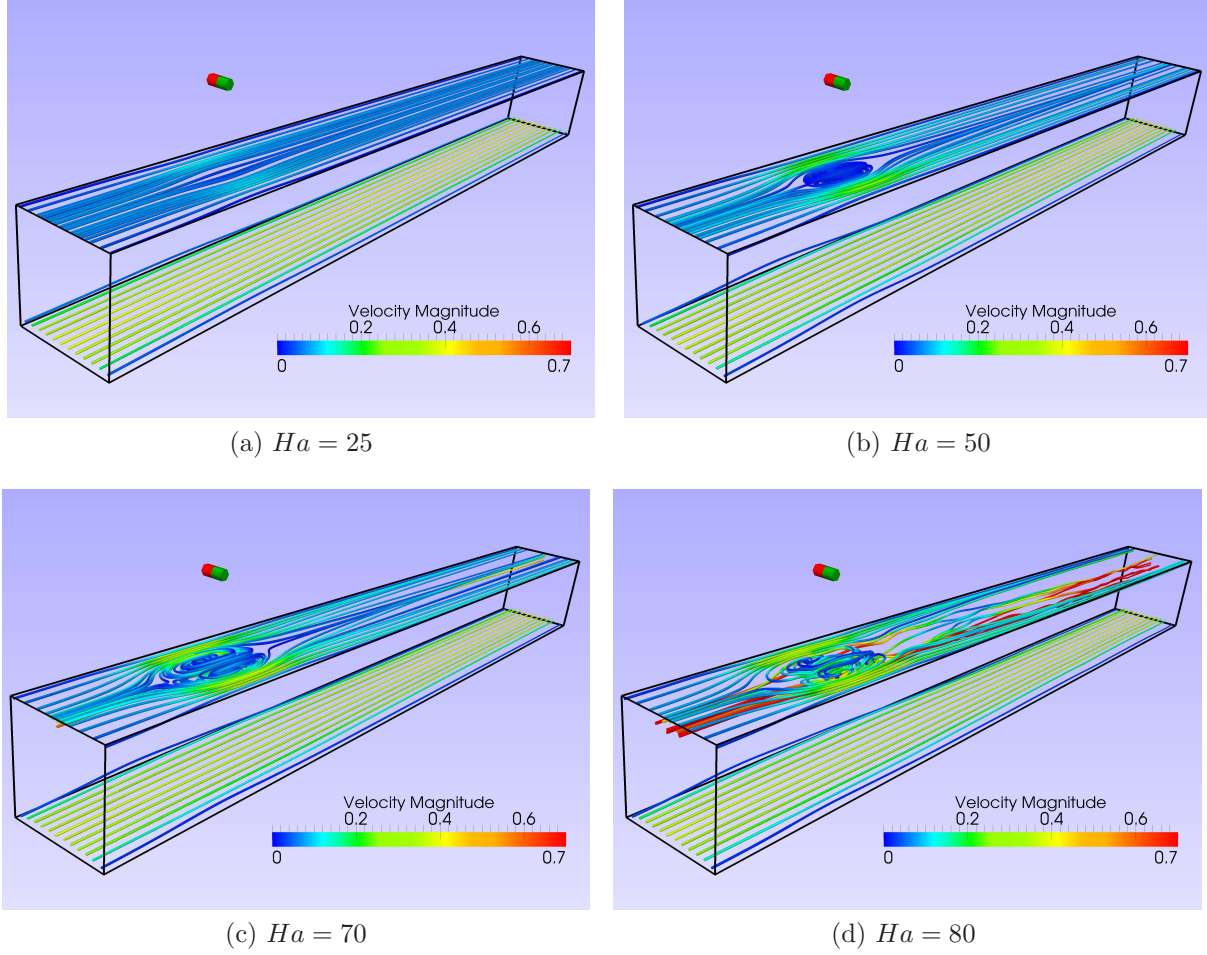
Figure 6.9.: Streamlines for different Hartmann numbers and spanwise dipole orientation at $Re = 2000$, $h = 1.6$.

this with frequency of vortex shedding behind a solid cylinder (Cuevas *et al.*, 2006*b*). The non-dimensional parameter for comparison would be then the Strouhal number

$$St = \frac{fD}{\overline{u}}. \tag{6.5}$$

Here, f denoted the frequency, $\overline{u}$ the mean velocity and D the characteristic length of the obstacle, e. g. the radius of the cylinder. Whereas the frequency and the velocity are known in our setting, it is not obvious how to determine the characteristic length of the mangetic obstacle. A good estimate for the size of the magnetic obstacle is the area in which the flow is detached from the wall, that was already discussed above (cf. figure 6.5). This region is stretched along the streamwise direction and the shape may change in time due to the vortex shedding. We define the characteristic length D of the magnetic obstacle as the maximal spanwise width of the area that is enclosed by $\partial_z u_x = 0$ at $z = 1$.

(a) width of the magnetic obstacle

(b) Strouhal number

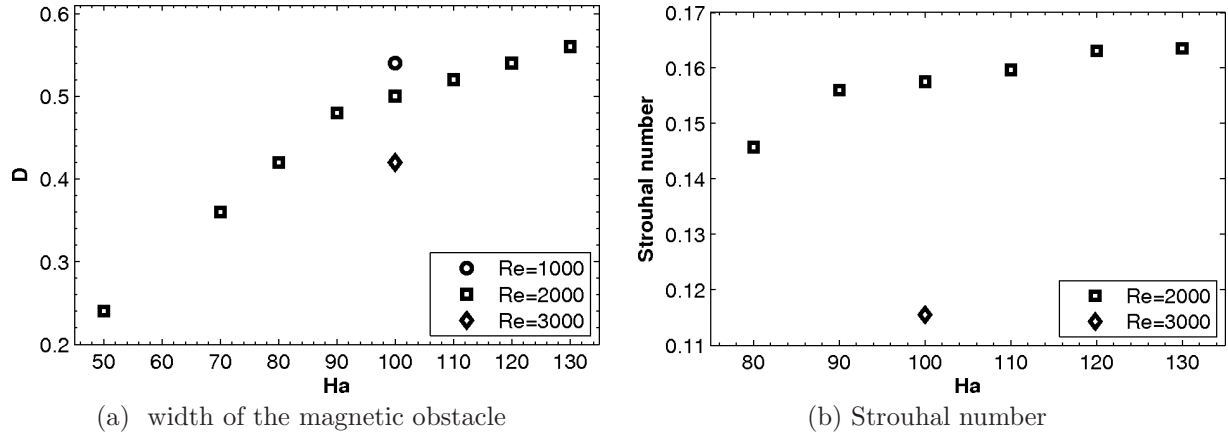Figure 6.10.: Characteristics of the vortex shedding. (a) The width of the magnetic obstacle increases linearly for small Hartmann numbers and comes to a saturation for higher Ha, where the vortex shedding appears. Increasing the Reynolds number leads to decreased width. (b) The Strouhal number increases slightly with increasing Hartmann number and decreases with increasing Reynolds number.

The obtained widths increase with increasing Hartmann number as displayed in figure 6.10a. In addition the width is decreased with increasing Reynolds number. It is worth to note the influence of the interaction parameter $N = Ha^2/Re$ in the following example. The width is approximately the same for the simulations with $Re = 2000$ plus $Ha = 80$ and $Re = 3000$ plus $Ha = 100$. Both cases have similar interaction parameter of $N = 3.2$ and $3.\overline{3}$, respectively. This estimate does not hold for the regime without vortex shedding.

Furthermore, the frequency is found to decrease with increasing Hartmann number. This behavior was also observed for the two-dimensional flow with a small magnetic obstacle (Cuevas *et al.*, 2006*b*). The Strouhal number in Cuevas *et al.* (2006*b*) was obtained with a characteristic length that was fixed by the size of the small magnet. Therefore, they describe a decrease of the Strouhal number in the dependence on the Hartmann number with values around $St \sim 0.1$. In the present work, the width of the area of reversed flow is used as a characteristic length of the magnetic obstacle. The resulting Strouhal number increases with a gentle slope and reaches a saturation around $St \sim 0.16$ (see figure 6.10b).

The result can be compared to the flow around solid cylinders. There, the Strouhal number is of the order $St \sim 0.2$ (Williamson, 1996). Dousset & Pothérat (2008) investigated the influence of a homogeneous magnetic field on the flow around a cylinder. In the regime of high Reynolds number, the Strouhal number was found to decrease with increasing Hartmann number. Thus, the homogeneous magnetic field damps the vortical structures. In our case, the inhomogeneous localized magnetic gives rise to the vortex formation and subsequent shedding.

The Strouhal number gives a quantitative description for the wake. It is desired to have an additional quantitative presentation for deflection of the flow that is caused by the dipole.
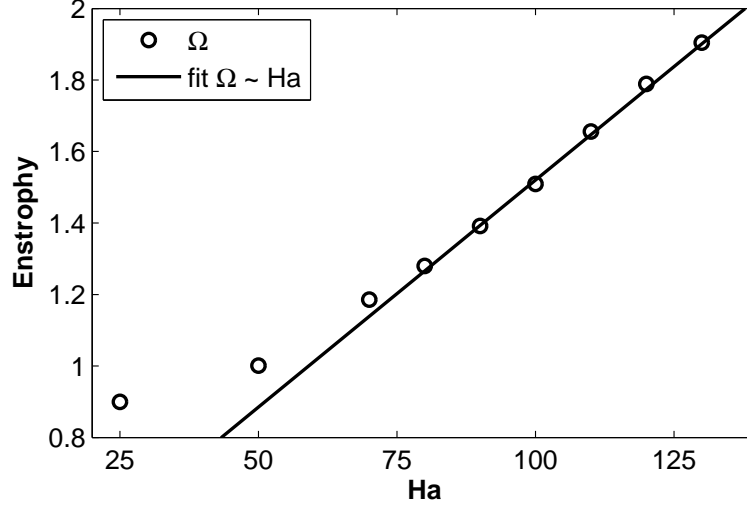
Figure 6.11.: The total enstrophy is linear dependent on the Hartmann number. This behavior is originated in the local Hartmann layers. Data is given for $Re = 2000$, $h = 1.6$ and spanwise oriented dipole.

The aim is therefore, to describe the structures in figure 6.9. A possible approach is to measure the vorticity, $\boldsymbol{\omega} = \nabla \times \boldsymbol{u}$, of the flow. For this, we consider the enstrophy over a cube below the dipole, i. e.

$$\Omega = \int_{[-1,1]^3} \frac{1}{2} |\nabla \times \boldsymbol{u}|^2 dV. \tag{6.6}$$

As the wake contains turbulent vortices, the integral is not applied to the whole domain. Thus we focus on the area, that is directly influenced by the dipole. Figure 6.11 shows that the enstrophy increases linearly with the Hartmann number, which is originated in the increase of the vorticity $\boldsymbol{\omega} = \nabla \times \boldsymbol{u}$ in the vortex as well as the Hartmann layers. The strongest contribution comes from the derivative $\partial_z u_x$, which reaches maximal magnitudes in the Hartmann layer, as already mentioned above (cf. figure 6.5). An integration shows that the integral $\int_{[-1,1]^3} \frac{1}{2} |\partial_z u_x|^2 dV$ gives already about 80% of the magnitude of the total enstrophy Ω.

To explain the linear dependence, we recall the properties of the Hartmann layers in homogeneous magnetic fields. It is known from the analytic solution of the Hartmann flow (Müller & Bühler, 2001), that $u_x \sim \cosh(Ha\, z)$. We can therefore estimate $(\partial_z u_x)^2 \sim (Ha \sinh(Ha\, z))^2$ in the Hartmann layer. The width of the Hartmann layer is given with $\delta \sim 1/Ha$. Therefore, the integration of the enstrophy leads to $\Omega \sim \int_0^\delta |(\partial_z u_x)^2| dz \sim Ha$.

It has to be marked here, that this explanation is not valid for the total enstrophy of Hartmann flow. Here, the Lorentz forces in the bulk of the flow produces an additional factor, that depends on the Hartmann number. Thus, only local Hartmann layers produced by a localized magnetic field reveal the linear dependence of the total enstrophy on the Hartmann number. Therefore, the qualitative presentation of the flow structures in terms

of the enstrophy (6.6) fails to provides details on the reversed flow an the vortex structures. Nevertheless, it gives a good criterion for the strength of the local Hartmann layers.

In this chapter the time-dependent flow structures were investigated for high Reynolds numbers. It was shown that the spanwise oriented dipole in a distance of $h = 1.6$ triggers vortex shedding in case of sufficient high Hartmann number. Comparing the magnetic obstacle with solid one, we determined a Strouhal number about 0.16. In addition, it was found that the enstrophy in the zone that is influenced by the Lorentz force increases linear with the Hartmann number. An effect that is caused by the local Hartmann layers.

7. Conclusion and Outlook

The aim of this work was to describe the influence of a magnetic point dipole on liquid metal flow in a square duct. The magnetic field of a dipole represents the simplest localized field, that can be described analytically. Due to the strong inhomogeneity it leads to a complex deflection of the flow, even if the geometry is chosen to be as basic as a square duct.

To cover all possible aspects in the investigation, direct numerical simulations with an in-house finite difference code were performed. A detailed verification of the calculations and a validation with laboratory experiments showed the reliability of the obtained results.

In the beginning of thesis work, five question were raised for the present investigation.

1. How strong is the total force that acts on this system? What is the influence of the strength and the shape of the magnetic field? What is the influence of the state of the flow on the total force?

To estimate the total Lorentz force, the kinematic regime was considered, where the flow is assumed to be not influenced by the force. Through this approximation, it is possible to describe the drag force for a fixed dipole orientation in dependence of only three non-dimensional parameters: The distance h of the dipole to the surface of the liquid, the Hartmann number Ha based on the maximum magnetic field inside the duct and the hydrodynamic Reynolds number Re. The first two parameters describe the shape and the strength of the magnetic field. The Hartmann number gives the prefactor Ha^2 to the Lorentz force. Two power laws were observed in a parameter study on the distance h. For very small distances the Lorentz force is proportional to h^{-2}, while for large distances, it behaves as h^{-7}. Both cases are explained with analytical expressions. The Reynolds number gives a prefactor of $1/Re$ to the Lorentz force, but also shows an additional effect, when the flow is turbulent. Here, the enhanced slope in the boundary layer increases the Lorentz forces.

2. What kind of deflection occurs? What is the physical mechanism driving such a phenomenon?

The basic mechanism of the deformation of the flow profile was then explained in the case of very low Reynolds number. The study was restricted to three orientations of the magnetic moment of the dipole: streamwise, spanwise and wall-normal vertical. Depending on the local distribution of the magnetic field, the flow is either accelerated or decelerated. Thus, local Hartmann layers are formed as well as regions of strong back flow, that lead to vortices.

3. What is the difference in the total force between the case of an undeflected and a

Distance dependence	Ha dependence	Re dependence
kinematic regime		
$F_x \sim h^{-2}$ for $h \ll 1$	$F_x \sim Ha^2$	$F_x \sim Re^{-1}$
$F_x \sim h^{-7}$ for $h \gg 1$		
	$F_z = 0$	
	$T_y \sim Ha^2$	$T_y \sim Re^{-1}$
dynamic regime		
distance	$F_x \sim Ha^2$	$F_x \sim Re^{-1}$
defines	$F_z \sim Ha^4$	$F_z \sim Re^0$ for $Re < 1$
deflected	$T_y \sim Ha^2$	$T_y \sim Re^{-1}$
area	$F_{dyn} \equiv F_{kin}$ for $Ha < 20$	exponential wake decay
	$< \Delta u > \sim Ha$	with decay rate $\sim Re^{-1}$
for $h > 1$		
vortex shedding	for $Re = 2000$:	Re influences
with $Ha = 100$	$\Omega \sim Ha$	wake instability
and $Re = 2000$	$St \approx 0.16$	

Table 7.1.: Overview of obtained power laws and dependencies.

deflected flow? Is there a certain range within which the flow can be approximated by an unaffected hydrodynamic profile?

The undeflected flow was considered in the kinematic regime and may be regarded as the limiting case of $Ha \to 0$. It was studied, how the increasing Hartmann number leads to an amplification in the flow deformation. The total drag force and the torque are found to be proportional to Ha^2. This is the same power law as in the kinematic case. In the range from $Ha = 0 \ldots 20$, the flow can be approximated by an undeflected profile. In the kinematic setting, there is only a force in streamwise direction. This changes with the distortion of the profile. Through the deflection, a lift force is induced. The total lift force is proportional to Ha^4 due to the contribution of the non-linear advection term.

4. How are the forces affected when the flow changes from the creeping to the transitional regime?

The strongest effect is observed for the lift force. It is independent of the Reynolds number for the creeping flow regime and decays steeper than $1/Re$ for higher Reynolds numbers. The drag force and the torque behaves like $1/Re$ in the whole range of $Re = 0.1 \ldots 3000$. When the Reynolds number is increased, we observe that the length of wake is increased. It was also shown why the spatial decay rate is proportional to $1/Re$.

5. Can the dipole trigger turbulence in the originally laminar flow? Is there a threshold in the strength of the magnetic field for the transition to occur?

Finally, it was investigated under which conditions the magnetic field of the dipole triggers turbulence. As the Reynolds number is increased to 2000, the vortex formation process

changes, and for the spanwise oriented dipole with $Ha = 100$ in a distance above $h = 1$, vortex shedding occurs. The structures are advected into the wake and further secondary instabilities lead to turbulence. The time-dependent flow structures were then investigated for high Reynolds numbers. The occurrence of the vortex shedding was found for Hartmann numbers above 80 with the spanwise oriented dipole at for $h = 1.6$ and $Re = 2000$. Below this threshold no vortex shedding was observed.

The total forces and the total torque still obey approximately the same power law, but the values are time-dependent. The time signal of the Lorentz force reveals the frequency of the vortex shedding. Comparing the magnetic obstacle with a solid one, we determined a Strouhal number of about 0.16. In addition, it was found that the enstrophy in the zone that is influenced by the Lorentz force increases linearly with the Hartmann number. An effect that is caused by the local Hartmann layers.

To answer the five questions, direct numerical simulations were provided to describe the Lorentz force on the magnet and the deformation of the flow for a wide parameter range. For three different dipole orientations the distance was varied between 10^{-3} and 500, Hartmann number was up to 130 and Reynolds number was in the range of $0.1 < Re < 3000$. Although the present work provides a detailed study on the interaction of a duct flow and magnetic dipole, the subject is far from being completed.

One might remark, that the considered Reynolds numbers are lower than the ones in industrial applications. In the same manner, the laminar inflow is not given in many applications. Simulations for those setting request an enhanced version of the code that is capable to apply inflow/outflow conditions. With this, it would be appropriate to investigate the influence of the turbulence on the deflection of the flow. Preliminary tests with fully turbulent flow show that it is quite hard to distinguish between the turbulent fluctuations and deflection by the dipole in a given snapshot, if the interaction parameter Ha^2/Re is too small. Here, time averaged values are necessary taken for long time series calculated with very fine mesh. In short, the computational resources have to be increased.

However, further extentions of the analysis are also possible for the laminar inflow. The present setting offers more parameters, especially geometrical variables. So far, the dipole is positioned in the centerline of the duct. An offset in spanwise direction would break the symmetry of the problem and lead to different structures in the wake. Thus the transition to turbulence can be affected. This opens perspectives for the flow manipulation and thus also for the flow control.

According to the orientation of the dipole, it would be interesting to investigate intermediate orientations. One question to answer would be for which orientations the vortex shedding is feasible. In addition, new structures in the wake may appear. A preliminary example is shown in figure 7.1 for a orientation of $\boldsymbol{m} = 1/\sqrt{2}(\boldsymbol{e}_x + \boldsymbol{e}_y)$.

A further extension of this work would be the inclusion of finite magnetic Reynolds numbers. This requires the solution of the magnetic induction equation inside and outside the computational domain, because secondary magnetic field is induced in the whole space and has to be continuous. This can be possibly solved by means of boundary element methods.
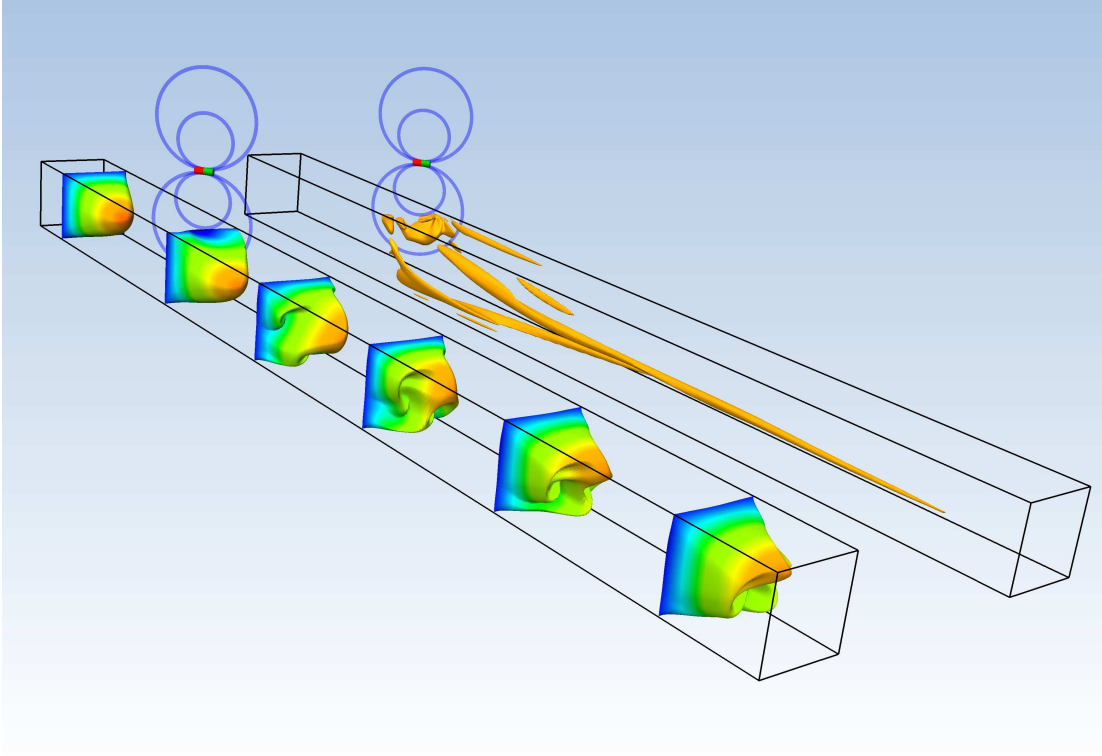
Figure 7.1.: Oblique orientations lead to a swirl in the flow. Data is obtained with the same setting as in figure 6.4 besides that dipole orientation is $\boldsymbol{m} = 1/\sqrt{2}(\boldsymbol{e}_x + \boldsymbol{e}_y)$.

A project of this size would (and will) provide sufficient material for further thesis.

Having these future perspectives in mind, the presented work provides a appropriate foundation to further studies on the magnetohydrodynamic duct flow in the presence of a magnetic point dipole.

A. Power law for large distances

We assume that the dipole is placed in the symmetry plane $y = 0$ but allow for arbitrary dipole orientation. In this situation, the leading order terms of the non-dimensional magnetic field components are

$$B_x^0(\hat{x}) = \frac{1}{4\pi h^3} \frac{k_x(2\hat{x}^2 - 1) + 3k_z\hat{x}}{(\hat{x}^2 + 1)^{5/2}} \ ,$$

$$B_y^0(\hat{x}) = \frac{1}{4\pi h^3} \frac{-k_y}{(\hat{x}^2 + 1)^{3/2}} \ ,$$

$$B_z^0(\hat{x}) = \frac{1}{4\pi h^3} \frac{-3k_x\hat{x} + k_z(2 - \hat{x}^2)}{(\hat{x}^2 + 1)^{5/2}} \ .$$

They depend only on $\hat{x}$. The y-component of the magnetic field vanishes to leading order for dipoles with orientations $\boldsymbol{m} = (0,0,1)$ and $\boldsymbol{m} = (1,0,0)$, while B_z^0 vanishes for $\boldsymbol{m} = (0,1,0)$.

To obtain the electric currents $\boldsymbol{j}^0$, $\boldsymbol{j}^1$ and $\boldsymbol{j}^2$ one has to solve the Poisson equation (2.7) for the electrical potential up to the required order of approximation. We find the corresponding equations and boundary conditions for the electric potential at the different orders by substitution of the expansions and grouping terms of different orders. For the expansion of derivatives we note that the Nabla operator takes the form

$$\nabla = \left(\varepsilon \frac{\partial}{\partial \hat{x}} , \frac{\partial}{\partial \hat{y}} , \frac{\partial}{\partial \hat{z}} \right). \tag{A.1}$$

For the zero-order approximation the appropriate Laplace equation becomes

$$\frac{\partial^2 \varphi^0}{\partial \hat{y}^2} + \frac{\partial^2 \varphi^0}{\partial \hat{z}^2} = 0.$$

There is no normal current at insulating walls and

$$\left. \frac{\partial \varphi^0}{\partial \hat{y}} \right|_{\hat{y} = \pm 0.5} = -B_z^0,$$

$$\left. \frac{\partial \varphi^0}{\partial \hat{z}} \right|_{\hat{z} = \pm 0.5} = B_y^0.$$

The solution for the potential is then given by

$$\varphi^0 = \hat{z} B_y^0 - \hat{y} B_z^0 + const,$$

which gives the currents $\boldsymbol{j}^0 \equiv 0$. Hence, the integral (4.9) vanishes, $F_x^0 \equiv 0$. Also, all the integrands involving $\boldsymbol{j}^0$ in equations (4.10) and (4.11) are zero.

The currents in the bar have to fulfill the continuity equation $\nabla \cdot \boldsymbol{j} = 0$. Because of the result (A.1) we have

$$\frac{\partial j_x^0}{\partial \hat{x}} + \frac{\partial j_y^1}{\partial \hat{y}} + \frac{\partial j_z^1}{\partial \hat{z}} = 0.$$

This equation can be automatically satisfied for $j_x^0 = 0$ if a stream function $\psi = \psi(\hat{x}, \hat{y}, \hat{z})$ is introduced, i. e. $j_y^1 = \partial\psi/\partial\hat{z}$ and $j_z^1 = -\partial\psi/\partial\hat{y}$. We choose ψ to vanish at the walls and automatically satisfy boundary conditions for currents $\boldsymbol{j} \cdot \boldsymbol{n} = 0$ because the boundary is a streamline of electric current.

To obtain an equation for the stream function ψ, we consider the x component of the current curl,

$$\left(\nabla \times \boldsymbol{j}^1\right)_x = \frac{\partial j_z^1}{\partial \hat{y}} - \frac{\partial j_y^1}{\partial \hat{z}} = -\frac{\partial^2 \psi}{\partial \hat{y}^2} - \frac{\partial^2 \psi}{\partial \hat{z}^2}.$$

Ohm's law, $\boldsymbol{j} = -\nabla\varphi + \boldsymbol{u} \times \boldsymbol{B}$, gives

$$\left(\nabla \times \boldsymbol{j}^1\right)_x = \frac{\partial}{\partial \hat{y}}\left(-\frac{\partial\varphi^1}{\partial\hat{z}} + B_y^1\right) - \frac{\partial}{\partial\hat{z}}\left(-\frac{\partial\varphi^1}{\partial\hat{y}} - B_z^1\right)$$
$$= -\frac{\partial B_x^0}{\partial\hat{x}}.$$

The above result is obtained remembering that the magnetic field of the dipole is solenoidal and therefore

$$\frac{\partial B_x^0}{\partial\hat{x}} + \frac{\partial B_y^1}{\partial\hat{y}} + \frac{\partial B_z^1}{\partial\hat{z}} = 0.$$

Hence, we have to solve the following Poisson equation for the stream function

$$\frac{\partial^2 \psi}{\partial \hat{y}^2} + \frac{\partial^2 \psi}{\partial \hat{z}^2} = \frac{\partial B_x^0}{\partial \hat{x}}, \tag{A.2}$$

where $\psi|_{\text{wall}} = 0$. Equation (A.2) also governs the laminar flow profile in a rectangular duct (Pozrikidis, 1997). It can be solved using an infinite series expansion, whereby one finds

$$\int\limits_{-0.5}^{0.5} \int\limits_{-0.5}^{0.5} \psi \, d\hat{y} \, d\hat{z} = \frac{2.253}{64} \frac{\partial B_x^0}{\partial \hat{x}}. \tag{A.3}$$

This identity is used to calculate the x component of the first term from integral (4.10) which also vanishes:

$$\int (\boldsymbol{j}^1 \times \boldsymbol{B}^0)_x \, dV = -\frac{2.253}{64} \int\limits_{-\infty}^{\infty} B_x^0 \frac{\partial B_x^0}{\partial \hat{x}} h \, d\hat{x} \equiv 0.$$

The second order terms (4.11) should be evaluated to obtain a non-vanishing F_x. There are two such terms: $\int (\boldsymbol{j}^2 \times \boldsymbol{B}^0)_x \, dV$ and $\int (\boldsymbol{j}^1 \times \boldsymbol{B}^1)_x \, dV$. The latter integral can be solved using the stream function ψ by taking into account that

$$\int (\boldsymbol{j}^1 \times \boldsymbol{B}^1)_x \, dV = \frac{\partial}{\partial \hat{y}}(\psi B_y^1) + \frac{\partial}{\partial \hat{z}}(\psi B_z^1) + \psi \frac{\partial B_x^0}{\partial \hat{x}}.$$

By using Stokes' theorem we see that the first two terms do not contribute:

$$\int\limits_{-0.5}^{0.5} \int\limits_{-0.5}^{0.5} \left(\frac{\partial}{\partial \hat{y}}(\psi B_y^1) + \frac{\partial}{\partial \hat{z}}(\psi B_z^1) \right) d\hat{y} \, d\hat{z}$$

$$= \oint \left(\underbrace{\psi}_{=0} B_y^1 \, d\hat{z} - \underbrace{\psi}_{=0} B_z^1 \, d\hat{y} \right) = 0.$$

Then the integral can be transformed as

$$\int (\boldsymbol{j}^1 \times \boldsymbol{B}^1)_x \, dV = \iiint \psi(\hat{x}, \hat{y}, \hat{z}) \, d\hat{y} \, d\hat{z} \frac{\partial B_x^0}{\partial \hat{x}} h \, d\hat{x}.$$

Using equation (A.3), it integrates to

$$\int (\boldsymbol{j}^1 \times \boldsymbol{B}^1)_x \, dV = -\frac{15^2 \cdot 2.253}{2^{20} \pi h^5} \left(5k_x^2 + 7k_z^2 \right).$$

The integral $\int (\boldsymbol{j}^2 \times \boldsymbol{B}^0)_x \, dV$ contains $\boldsymbol{j}^2$. To compute the current at second order, we again use the continuity equation in the following form

$$\frac{\partial j_y^2}{\partial \hat{y}} + \frac{\partial j_z^2}{\partial \hat{z}} = -\frac{\partial j_x^1}{\partial \hat{x}} = -\frac{\partial^2 \varphi^0}{\partial \hat{x}^2}.$$

We can use this equation to obtain

$$j_x^1 = \hat{z} \frac{\partial B_y^0}{\partial \hat{x}} - \hat{y} \frac{\partial B_z^0}{\partial \hat{x}},$$

$$j_y^2 = \frac{1}{2} \left(\hat{y}^2 - \frac{1}{4} \right) \frac{\partial^2 B_z^0}{\partial \hat{x}^2},$$

$$j_z^2 = -\frac{1}{2} \left(\hat{z}^2 - \frac{1}{4} \right) \frac{\partial^2 B_y^0}{\partial \hat{x}^2},$$

which satisfy the boundary conditions for the current. The x component of the first term of F_x^2 (4.11) is then given by

$$\int (\boldsymbol{j}^2 \times \boldsymbol{B}^0)_x \, dV = \int \left(j_y^2 B_z^0 - j_z^2 B_y^0 \right) \, dV,$$

which can be computed analytically by integration by parts and variable substitution. We thereby obtain the expression

$$\int (\boldsymbol{j}^2 \times \boldsymbol{B}^0)_x \, dV = -\frac{15}{2^{16} \pi h^5} \left(35k_x^2 + 8k_y^2 + 57k_z^2 \right). \tag{A.4}$$

B. Power law for small distances

A semi-analytic expression for the electromagnetic drag of a magnetic point dipole on a Couette flow is derived in this appendix. Here, we do not restrict us to special case of vertical orientated dipole, but consider a the more general case of arbitrary orientation. Therefore, the analytic expression if the magnetic flux density for the dipole is given by

$$\boldsymbol{B}(\boldsymbol{x}) = \frac{1}{\kappa}\left(\frac{3\boldsymbol{m}\cdot\boldsymbol{r}}{r^5}\boldsymbol{r} - \frac{\boldsymbol{m}}{r^3}\right),$$

where $\boldsymbol{m} = k_x\boldsymbol{e}_x + k_y\boldsymbol{e}_y + k_z\boldsymbol{e}_z$ is the orientation of the magnetic moment with $k_x^2 + k_y^2 + k_z^2 = 1$, $\kappa \equiv \sqrt{k_x^2 + k_y^2 + 4k_z^2}$ and $\boldsymbol{r} = \boldsymbol{x} - \boldsymbol{r}_0$, with the dipole position $\boldsymbol{r}_0 = (0, 0, h)$. The formula is normalized such that the maximum of the magnetic flux density equals to 1 inside the fluid. Accordingly, we get

$$Ha = \frac{M\kappa}{4\pi h^3}.$$

The parameter M is the intrinsic Hartmann number, that we introduced in equation (4.3). For the velocity field, we consider a Couette flow with the velocity field $\boldsymbol{u} = -z\boldsymbol{e}_x$ for $z < 0$. The aim is to calculate the Lorentz force, i. e.

$$F_x = \frac{Ha^2}{Re}\int\left((-\nabla\varphi + \boldsymbol{u}\times\boldsymbol{B})\times\boldsymbol{B}\right)\cdot\boldsymbol{e}_x\,dV.$$

The most difficult part is to find a solution for the Poisson equation for the electric potential, i. e.

$$\Delta\varphi(\boldsymbol{r}) = -\left(\frac{3k_xxy + 3k_yy^2 + 3k_z(z-h)y}{\sqrt{x^2+y^2+(z-h)^2}^5} - \frac{k_y}{\sqrt{x^2+y^2+(z-h)^2}^3}\right).$$

This Poisson equation is similar to the one that has to be solved in case of rotary flowmeter, which can be solved analytically (Priede *et al.*, 2011*b*). To solve this Poisson equation for the electric potential, one can apply the Green function in free space. We define an analytic continuation of φ its reflection through the surface ($z = 0$), i. e.

$$\Delta\varphi(x, y, z) = -B_y(x, y, -z) \text{ for } z > 0.$$

In $\mathbb{R}^3$ the Poisson equation can now the written as

$$\Delta\varphi(x, y, z) = -B_y(x, y, -|z|)$$

with

$$B_y(x, y, -|z|) = \frac{3k_x xy + 3k_y y^2 + 3k_z(|z| + h)y}{\sqrt{x^2 + y^2 + (|z| + h)^2}^5} - \frac{k_y}{\sqrt{x^2 + y^2 + (|z| + h\backslash)^2}^3}$$

Using the Greens function $G(\boldsymbol{x}, \boldsymbol{x}') = \frac{1}{4\pi} \frac{1}{|\boldsymbol{x}-\boldsymbol{x}'|}$, we can write

$$\varphi(\boldsymbol{x}) = -\int_{\mathbb{R}^3} G(\boldsymbol{x}, \boldsymbol{x}') B_y(x', y', -|z'|) \, dV'.$$

The magnetic flux density is solenoidal, i.e. $\nabla\varphi \times \boldsymbol{B} = \nabla \times (\varphi\boldsymbol{B})$, thus, we can calculate the contribution of the potential to the total Lorentz force by

$$\begin{aligned}
\boldsymbol{F}_\varphi &= -\frac{1}{2}\frac{Ha^2}{Re} \int_{z<0} -\nabla\varphi \times \boldsymbol{B} \, dV \\
&= -\frac{1}{2}\frac{Ha^2}{Re} \int_{z=0} \boldsymbol{n} \times \varphi\boldsymbol{B} \, dxdy \\
&= -\frac{1}{2}\frac{Ha^2}{Re} \int_{z=0} \varphi(-B_y\boldsymbol{e}_x + B_x\boldsymbol{e}_y) \, dxdy,
\end{aligned}$$

where $\boldsymbol{n} = (0, 0, 1)$ is the normal vector on the surface. We find with the solution for the electric potential that

$$\boldsymbol{F}_\varphi = \frac{1}{2}\frac{Ha^2}{Re} \int_{z=0} \left[\int_{\mathbb{R}^3} G(\boldsymbol{x}, \boldsymbol{x}') B_y(x', y', -|z'|) \, dV'\right] (-B_y\boldsymbol{e}_x + B_x\boldsymbol{e}_y) \, dxdy.$$

In a similar way, we calculate the contribution from the velocity by

$$\begin{aligned}
\boldsymbol{F}_{\boldsymbol{u}\times\boldsymbol{B}} &= \frac{1}{2}\frac{Ha^2}{Re} \int_{z<0} (\boldsymbol{u} \times \boldsymbol{B}) \times \boldsymbol{B} \, dV \\
&= \frac{1}{2}\frac{Ha^2}{Re} \int_{z<0} (-z\boldsymbol{e}_x \times \boldsymbol{B}) \times \boldsymbol{B} \, dV \\
&= -\frac{1}{2}\frac{Ha^2}{Re} \int_{z<0} z(-B_z^2\boldsymbol{e}_x - B_y^2\boldsymbol{e}_x + B_yB_x\boldsymbol{e}_y + B_zB_x\boldsymbol{e}_z) \, dV.
\end{aligned}$$

The total Lorentz force is therefore

$$\begin{aligned}
\boldsymbol{F} &= \frac{1}{2}\frac{Ha^2}{Re}(\boldsymbol{F}_\varphi + \boldsymbol{F}_{\boldsymbol{u}\times\boldsymbol{B}}) \\
&= \frac{1}{2}\frac{Ha^2}{Re} \left(\int_{z=0} \left[\int_{\mathbb{R}^3} G(\boldsymbol{x}, \boldsymbol{x}') B_y(x', y', -|z'|) \, dV'\right] (-B_y\boldsymbol{e}_x + B_x\boldsymbol{e}_y) \, dxdy \right. \\
&\quad \left. + \int_{z<0} z(-B_z^2\boldsymbol{e}_x - B_y^2\boldsymbol{e}_x + B_yB_x\boldsymbol{e}_y + B_zB_x\boldsymbol{e}_z) \, dV\right).
\end{aligned}$$

dipole	fitted to	DNS data		numerical	integration[1]	
orientation	α_u	α_φ	α	α_u	α_φ	α
vertical	-0.5954	0.3970	-0.1920	-0.589	0.393	-0.195
streamwise	-0.2501	0.1002	-0.1499	-0.245	0.097	-0.148
spanwise	-0.3450	0.2967	-0.0482	-0.343	0.294	-0.050

Table B.1.: Coefficient for small distance approximation from equation (4.15), that were obtained by fitting the power law to the data, that are calculated by DNS and by a numerical integration of the derived formulas for the coefficients[1]. Here, α_u determines the velocity distribution and α_φ the distribution of the electric potential to the streamwise Lorentz force. The total coefficient is given by $\alpha = \alpha_u + \alpha_\varphi$.

To show explicitly the dependence of the force on the distance h in the formula above, we rescale the coordinates by $\boldsymbol{x} = h\hat{\boldsymbol{x}}$. With this rescaling we get $Ha = M\kappa/2\pi$, $\boldsymbol{B} \sim h^{-3}$ and $G \sim h^{-1}$. This result may now be written for the drag component of the Lorentz force as

$$F_x = -\frac{M^2}{Re}\frac{\kappa^2(\alpha_\varphi + \alpha_u)}{(4\pi)^2 h^2}. \tag{B.1}$$

The constants α_φ and α_u represent the integrals as defined in equations (4.16) and (4.17). The obtained result (B.1) is used for the comparison with the numerical results from the laminar duct flow with a point dipole in small distances. Details on the results of this comparison are shown in table B.1. Note that for a duct the definition of the shear rate as $\Omega = \overline{u}/L$ is not valid any more. For the results in table B.1, the shear rate was evaluated numerically.

It has to be emphasized, that the used method above may be used for every arbitrary velocity distribution $\boldsymbol{u}(x, y, z)$ and arbitrary mangetic flux density, respectively. The only requirement is $\partial_z\varphi = (\boldsymbol{u} \times \boldsymbol{B})_z = 0$ at $z = 0$, which ensures the smoothness of the analytic continuation along the plane of reflection. This condition is automatically fullfilled for flows with no-slip boundary conditions.

---

[1]Courtesy to Thomas Boeck for providing these data.

Bibliography

ADAMS, J. C. 1991 Mudpack: Multigrid software for elliptic partial differential equations. *Tech. Rep.* NCAR/TN-357+STR. NCAR TECHNICAL NOTE, http://nldr.library.ucar.edu/repository/assets/technotes/asset-000-000-000-167.pdf.

ADAMS, J. C., SWARZTRAUBER, P. & WEET, R. 1999 Efficient fortran subprograms for the solution of separable elliptic partial differential equations. http://www.cisl.ucar.edu/css/software/fishpack/.

ALBRECHT, T. 2010 Zur Transition an einer ebenen Platte und deren Beeinflussung durch elektromagnetische Kräfte. PhD thesis, Technische Universität Dresden.

ALBRECHT, T., GRUNDMANN, R., MUTSCHKE, G. & GERBETH, G. 2006 On the stability of the boundary layer subject to a wall-parallel Lorentz force. *Phys. Fluids* **18**, 098103.

ALBRECHT, T., METZKES, H., GRUNDMANN, R., MUTSCHKE, G. & GERBETH, G. 2008 Tollmin-Schlichting wave damping by a streamwise oscillating Lorentz force. *Magnetohydrodynamics* **44** (3), 205–222.

ALFVÉN, H. 1946 On the cosmogony of the solar system III. *Stockholms Observatoriums Annaler* **4** (9), 1–29.

ALPHER, A., HURWITZ, H., JOHNSON, R. H. & WHITE, D. R 1960 Some studies of free-surface mercury magnetohydrodynamics. *Rev. Mod. Phys.* **32**, 758–769.

ANDREEV, O., KOLESNIKOV, Y. & THESS, A. 2006 Experimental study of liquid metal channel flow under the influence of a nonuniform magnetic field. *Phys. Fluids* **18**, 065108.

ARGYROPOULOS, S. A. 2000 Measuring velocity in high-temperature liquid metals: A review. *Scand. J. Metall.* **30(5)**, 273–285.

BAKER, R. C. 2004 *An Introductory Guide to Flow Measurement*. American Society of Mechanical Engineers.

BATCHELOR, G. K. 1951 Pressure fluctuations in isotropic turbulence. *Proc. Cambridge Philos. Soc.* **47**, 359–374.

BAUMGARTL, J., HUBERT, A. & MÜLLER, G. 1993 The use of magnetohydrodynamic effects to investigate fluid flow in electrically conducting melts. *Phys. Fluids A* **5** (12), 3280–3289.

BEDDOES, J. & BIBBY, M. 1999 *Principles of Metal Manufacturing Processes*. Butterworth-Heinemann.

BEVIR, M. K. 1970 The theory of induced voltage electromagnetic flowmeters. *J. Fluid Mech.* **43** (3), 577–590.

BHUSHAN, S. & WALTERS, D. K. 2012 A dynamic hybrid Reynolds-averaged Navier Stokes-Large Eddy Simulation modeling framework. *Phys. Fluids* **24**, 015103.

BIAU, D., SOUEID, H. & BOTTARO, A. 2008 Transition to turbulence in duct flow. *J. Fluid Mech.* **596**, 133–142.

BINI, DARIO A. & MEINI, BEATRICE 2009 The cyclic reduction algorithm: From Poisson equation to stochastic processes and beyond. *Numer. Algor.* **51**, 23–60.

BISKAMP, D. 1993 *Nonlinear Magnetohydrodynamics*. Cambridge University Press.

BOTTARO, ALESSANDRO, SOUEID, HOUSSAM & GALLETTI, BERNARDO 2006 Formation of secondary vortices in turbulent square-duct flow. *AIAA Journal* **44** (4), 803–811.

BROWN, DAVID L., CORTEZ, RICARDO & MINION, MICHAEL L. 2001 Accurate projection methods for the incompressible Navier-Stokes equations. *J. Comp. Phys.* **168** (2), 464–499.

BUCENIEKS, I. 2000 Perspectives of using rotating permanent magnets in the design of electromagnetic induction pumps. *Magnetohydrodynamics* **36** (2).

BÜHLER, L. 1996 Instabilities in quasi-two-dimensional magnetohydrodynamic flows. *J. Fluid Mech.* **326**, 125–150.

BÜHLER, L., HORANYI, S. & ARBOGAST, E. 2007 Experimental investigation of liquid-metal flows through a sudden expansion at fusion-relevant Hartmann numbers. *Fusion Eng. Des.* **82** (15-24), 2239 – 2245.

CHORIN, A. J. 1968 Numerical solution of the Navier-Stokes equations. *Math. Comp.* **22** (104), 745762.

CHORIN, A. J. 1969 On the convergence of discrete approximations to the Navier-Stokes equations. *Math. Comp.* **23**, 341–353.

CIERPKA, C., WEIER, T., GERBETH, G., UHLEMANN, M. & ECKERT, K. 2007 Copper deposition and dissolution in seemingly parallel electric and magnetic fields: Lorentz force distributions and flow configurations. *J. Solid State Electrochem.* **11** (6), 687–701.

CUEVAS, S., SMOLENTSEV, S. & ABDOU, M. 2006*a* Vorticity generation in creeping flow past a magnetic obstacle. *Phys. Rev. E* **74** (5), 1–10.

CUEVAS, S., SMOLENTSEV, S. & ABDOU, M. A. 2006*b* On the flow past a magnetic obstacle. *J. Fluid Mech.* **553**, 227–252.

DAVIDSON, P. A. 2004 *Turbulence: An introduction for scientists and engineers*. Oxford University Press.

DAVIDSON, P. A., ed. 2006 *An Introduction to Magnetohydrodynamics*. Cambridge University Press.

DAVIDSON, P. A. 1999 Magnetohydrodynamics in material processing. *Annu. Rev. Fluid Mech.* **31**, 273–300.

DOUSSET, V. & POTHÉRAT, A. 2008 Numerical simulations of a cylinder wake under a strong axial magnetic field. *Phys. Fluids* **20**, 017104.

E, W. & LIU, J.-G. 1995 Projection Method I: Convergence and Numerical Boundary Layers. *SIAM J. Numer. Anal.* **32** (4), 1017–1057.

E, W. & LIU, J.-G. 1996 Projection method II: Godunov-Ryabenki analysis. *SIAM J. Numer. Anal.* **33** (4), 1597–1621.

E, W. & LIU, J.-G. 2001 Projection method III: Spatial discretization on the staggered grid. *Math. Comput.* **71** (237), 27–48.

ECKERT, S., GERBETH, G. & MELNIKOV, V. I. 2003 Velocity measurements at high temperatures by ultrasound Doppler velocimetry using an acoustic wave guide. *Exp. Fluids* **35**, 381–388.

FARADAY, M. 1832 Experimental researches in electricity. *Phil. Trans.* **122**, 175.

FENG, C. C., DEEDS, W. E. & DODD, C. V. 1975 Analysis of eddy-current flowmeters. *J. Appl. Phys.* **46** (7), 2935–2940.

FERZIGER, J. & PERIC, M. 2002 *Computational Methods for Fluid Dynamics*. Springer Berlin Heidelberg.

GAVRILAKIS, S. 1992 Numerical simulation of low-Reynolds-number turbulent flow through a straight square duct. *J. Fluid Mech.* **244**, 101–129.

GELFGAT, Y. M. & OLSHANSKII, S. V. 1978 Velocity structure of flows in non-uniform constant magnetic fields II. Experimental results. *Magnetohydrodynamics* **14**, 151–154.

GELFGAT, Y. M., PETERSON, D. E. & SHCHERBININ, E. V. 1978 Velocity structure of flows in nonuniform constant magnetic fields I. Numerical calculation. *Magnetohydrodynamics* **14**, 55–61.

GERARD-VARET, D. 2002 Amplification of small perturbations in a Hartmann layer. *Phys. Fluids* **14** (4), 1458–1467.

GRESHO, P. M. & SANI, R. L. 1987 On pressure boundary conditions for the incompressible Navier-Stokes equations. *Int. J. Numer. Meth. Fl.* **7**, 1111–1145.

HARTMANN, J. 1937 Hg-dynamics I. Theory of the laminar flow of an electrically conductive liquid in a homogeneous magnetic field. *K. Dan. Vidensk. Selsk. Mat. Fys. Medd.* **15** (6), 1–28.

HARTMANN, J. & LAZARUS, F. 1937 Hg-dynamics II. Experimental investigations on the flow of mercury in a homogeneous magnetic field. *K. Dan. Vidensk. Selsk. Mat. Fys. Medd.* **15** (7), 1–45.

HEINICKE, C. 2012 Local Lorentz Force Velocimetry for Liquid Metal Duct Flows. PhD thesis, Technische Universität Ilmenau.

HEINICKE, C., TYMPEL, S., PULUGUNDLA, G., RAHNEBERG, I., BOECK, T. & THESS, A. 2013 Interaction of a small permanent magnet with a liquid metal duct flow. *J. Appl. Phys.* Accepted for publication.

HUNT, J. C. R. 1965 Magnetohydrodynamic flow in rectangular ducts. *J. Fluid Mech.* **21** (4), 577–590.

HUNT, J. C. R. 1966 On the stability of parallel flows with parallel magnetic fields. *P. Roy. Soc. Lond. A Math.* **293** (1434), 342–358.

HUNT, J. C. R. & SHERCLIFF, J. A. 1971 Magnetohydrodynamics at high Hartmann number. *Annu. Rev. Fluid Mech.* **3**, 37–62.

HUNT, J. C. R. & STEWARTSON, K. 1965 Magnetohydrodynamic flow in rectangular ducts. II. *J. Fluid Mech.* **23** (3), 563–581.

HUSER, A. & BIRINGEN, S. 1993 Direct numerical simulation of turbulent flow in a square duct. *J. Fluid Mech.* **257**, 65–95.

JACKSON, J. D. 1998 *Classical Electrodynamics*, 3rd edn. New York: Wiley.

JEONG, J & HUSSAIN, F 1995 On the identification of a vortex. *J. Fluid Mech.* **285**, 69–94.

JEONG, J., HUSSAIN, F., SCHOPPA, W. & KIM, J. 1997 Coherent structures near the wall in a turbulent channel flow. *J. Fluid Mech.* **332**, 185–214.

KAWAHARA, G., AYUKAWA, K., OCHI, J., ONO, F. & KAMADA, E. 2000 Wall shear stress and Reynolds stresses in a low-Reynolds-number turbulent square-duct flow. *Trans. JSME* **66B**, 95–102, *(in Japanese)*.

KAWAHARA, G. & KAMADA, E. 2000 Vortical structures in the corner region of a turbulent square-duct flow. *Trans. JSME B* **66** (643), 89–97.

KAWAI, S. & LARSSON, J. 2012 Wall-modeling in Large Eddy Simulation: Length scales, grid resolution, and accuracy. *Phys. Fluids* **24**, 1–11.

KENJERES, S. 2008 Numerical analysis of blood flow in realistic arteries subjected to strong non-uniform magnetic fields. *Int. J. Heat Fluid Fl.* **29** (3), 752–764.

Kenjeres, S., ten Cate, S. & Voesenek, C. J. 2010 Vortical structures behind magnetic obstacles in transitional flow regimes. pp. 1–6. Proceedings of the 8th International ERCOFTAC Symposium on Engineering Turbulence Modelling and Measurements, Marseille, 9-11 June 2010.

Kenjeres, S. & Hanjalić, K. 2007*a* Numerical insights into magnetic dynamo action in a turbulent regime. *New J. Phys.* **9** (306).

Kenjeres, S. & Hanjalić, K. 2007*b* Numerical simulation of a turbulent magnetic dynamo. *Phys. Rev. Lett.* **98**, 104501.

Khripchenko, S., Khalilov, R., Kolesnichenko, I., Denisov, S., Galindo, V. & Gerbeth, G. 2010 Numerical and experimental modelling of various MHD induction pumps. *Magnetohydrodynamics* **46** (1), 85–97.

Kinet, M., Knaepen, B. & Molokov, S. 2009 Instabilities and transition in magnetohydrodynamic flows in ducts with electrically conducting walls. *Phys. Rev. Lett.* **103**, 15501.

Kirkpatrick, R. J. 1975 Crystal growth from the melt: A review. *American Mineralogist* **60**, 798–814.

Kirpo, M., Tympel, S., Boeck, T., Krasnov, D. & Thess, A. 2011 Electromagnetic drag on a magnetic dipole near a translating conducting bar. *J. Appl. Phys.* **109** (11).

Knaepen, B., Debliquy, O. & Carati, D. 2005 Large-Eddy Simulation without filter. *J. Comp. Phys.* **205** (1), 98–107.

Knaepen, B. & Moreau, R. 2008 Magnetohydrodynamic turbulence at low magnetic Reynolds number. *Annu. Rev. Fluid Mech.* **40** (1), 25–45.

Kobayashi, H. 2008 Large Eddy Simulation of magnetohydrodynamic turbulent duct flows. *Phys. Fluids* **20**, 1–13.

Kolesnikov, Y., Karcher, C. & Thess, A. 2011 Lorentz force flowmeter for liquid aluminum: Laboratory experiments and plant tests. *Metall. Mater. Trans. B* **42** (3), 691–700.

Korjenevsky, A., Cherepenin, V. & Sapetsky, S. 2000 Magnetic induction tomography: Experimental realization. *Physiol. Meas.* **21** (89).

Krasnov, D., Zikanov, O. & Boeck, T. 2011 Comparative study of finite difference approaches in simulation of magnetohydrodynamic turbulence at low magnetic Reynolds number. *Comput. Fluids* **50** (1), 46–59.

Krasnov, D., Zikanov, O., Rossi, M. & Boeck, T. 2010 Optimal linear growth in magnetohydrodynamic duct flow. *J. Fluid Mech.* **653**, 273–299.

Langlois, W. E. 1985 Buoyancy-driven flows in crystal-growth melts. *Annu. Rev. Fluid Mech.* **17**, 191–215.

LANTZSCH, R., GALINDO, V., GRANTS, I., ZHANG, C., PÄTZOLD, O., GERBETH, G. & STELTER, M. 2007 Experimental and numerical results on the fluid flow driven by a traveling magnetic field. *J. Cryst. Growth* **305** (1), 249–256.

LINGWOOD, R. J. & ALBOUSSIERE, T. 1999 On the stability of the Hartmann layer. *Phys. Fluids* **11** (8), 2058–2068.

MISTRANGELO, C. 2005 Three-dimesional MHD flow in sudden expansions. PhD thesis, Universität Karlsruhe.

MISTRANGELO, C. 2011*a* Topological analysis of separation phenomena in liquid metal flow in sudden expansions. Part 1. Hydrodynamic flow. *J. Fluid Mech.* **674**, 120–131.

MISTRANGELO, C. 2011*b* Topological analysis of separation phenomena in liquid metal flow in sudden expansions. Part 2. Magnetohydrodynamic flow. *J. Fluid Mech.* **674**, 132–162.

MOREAU, R. J. 1990 *Magnetohydrodynamics*. Kluwer Academic Publishers.

MORESCO, P. & ALBOUSSIERE, T. 2003 Experimental study of the instability of the Hartmann layer. *J. Fluid Mech.* **504**, 167–181.

MORINISHI, Y., LUND, T. S., VASILYEV, O. V. & MOIN, P. 1998 Fully conservative higher order finite difference scheme for incompressible flow. *J. Comp. Phys.* **143** (1), 90–124.

MÜLLER, U. & BÜHLER, L. 2001 *Magnetohydrodynamics in Channels and Containers*. Springer-Verlag.

NI, M.-J., MUNIPALLI, R., MORLEY, N. B., HUANG, P. & ABDOU, M. A. 2007 A current density conservative scheme for incompressible MHD flows at low magnetic Reynolds number. Part I: On a rectangular collocated grid system. *J. Comp. Phys.* **227**, 174–204.

NITSCHE, W. M. & BRUNN, A. 2006 *Strömungsmesstechnik*. Springer Berlin Heidelberg.

NIU, K. 1989 *Nuclear fusion*. Cambridge University Press.

NORDSTRÖM, J., NORDIN, N. & HENNINGSON, D. 1999 The fringe region technique and the Fourier method used in the Direct Numerical Simulation of spatially evolving viscous flows. *SIAM J. Sci. Comput.* **20** (4), 1365–1393.

PALMER, B. S. 2004 Current density and forces for a current loop moving parallel over a thin conducting sheet. *Eur. J. Phys.* **25** (655), 655–666.

PETTERSON REIF, B. A. & ANDERSSON, H. I. 2002 Prediction of turbulence-generated secondary mean flow in a square duct. *Flow Turbul. Combust.* **68**, 41–61.

PINELLI, A., UHLMANN, M., SEKIMOTO, A. & KAWAHARA, G. 2010 Reynolds number dependence of mean flow structure in square duct turbulence. *J. Fluid Mech.* **644**, 107–122.

POZRIKIDIS, C., ed. 1997 *Introduction to Theoretical and Computational Fluid Dynamics*. Oxford University Press.

PRIEDE, J., BUCHENAU, D. & GERBETH, G. 2009 Force-free and contactless sensor for electromagnetic flowrate measurements. *Magnetohydrodynamics* **45** (3), 451–458.

PRIEDE, J., BUCHENAU, D. & GERBETH, G. 2011*a* Contactless electromagnetic phase-shift flowmeter for liquid metals. *Meas. Sci. Technol.* **22** (5).

PRIEDE, J., BUCHENAU, D. & GERBETH, G. 2011*b* Single-magnet rotary flowmeter for liquid metals. *J. Appl. Phys.* **110** (3).

PULUGUNDLA, G. 2012 Numerical modelling of liquid metal flows interacting with strongly inhomogeneous magnetic fields. PhD thesis, Technische Universität Ilmenau.

PULUGUNDLA, G., HEINICKE, C., KARCHER, C. & THESS, A. submitted Lorentz force velocimetry with a small permanent magnet. Submitted to Eur. J. Mech. B Fluid.

REITZ, J. 1970 Forces on moving magnets due to eddy currents. *J. Appl. Phys.* **41** (5), 2067–2071.

RICOU, R. & VIVES, C. 1982 Local velocity and mass transfer measurements in molten metals using an incorporated magnet probe. *Int. J. of Heat Mass Transfer* **25**, 1579–1588.

RÜDIGER, G. & HOLLERBACH, R. 2004 *The Magnetic Universe: Geophysical and Astrophysical Dynamo Theory*. Wiley-VCH Verlag GmbH & Co. KGaA.

SAGAUT, PIERRE 1998 *Large Eddy Simulation for Incompressible Flows: An Introduction*. Springer Berlin Heidelberg.

SANI, R. L., SHEN, J., PIRONNEAU, O. & GRESHO, P. M. 2006 Pressure boundary condition for the time-dependent incompressible Navier-Stokes equations. *Int. J. Numer. Meth. Fluids* **50**, 673–682.

SCHLATTER, P. & ÖRLÜ, R. 2010 Assessment of direct numerical simulation data of turbulent boundary layers. *J. Fluid Mech.* **659**, 116–126.

SCHNACK, D. D. 2009 *Lecture in Magnetohydrodynamics: With an Appendix on Extended MHD*. Lect. Notes Phys. 780. Springer Berlin Heidelberg.

SCHREWE, H. F., ed. 1989 *Continuous Casting of Steel: Fundamental Principles and Practice*. Verlag Stahleisen mbH.

SHATROV, V. & GERBETH, G. 2006 On magnetohydrodynamic drag reduction and its efficiency. *Magnetohydrodynamics* **42** (2-3), 181–186.

SHATROV, V. & GERBETH, G. 2010 Marginal turbulent magnetohydrodynamic flow in a square duct. *Phys. Fluids* **22**, 08101.

SHERCLIFF, J. A., ed. 1962 *The Theory of Electromagnetic Flow Measurement*. Cambridge University Press.

SHERCLIFF, J. A. 1956 The flow of conducting fluids in circular pipes under transverse magnetic fields. *J. Fluid Mech.* **1** (6), 644–666.

SHERCLIFF, J. A. 1965 Magnetohydrodynamics, A film produced by Educational Services Inc., Watertown, Massachusetts, USA.

STEFANI, F., GIESECKE, A. & GERBETH, G. 2009 Numerical simulations of liquid metal experiments on cosmic magnetic fields. *Theor. Comput. Fluid Dyn.* **23**, 405–429.

STEFANI, F., GUNDRUM, T. & GERBETH, G. 2004 Contactless inductive flow tomography. *Phys. Rev. E* **70** (5), 056306.

STERL, A. 1990 Numerical simulation of liquid-metal MHD flows in rectangular ducts. *J. Fluid Mech.* **216**, 161–191.

SZEKELY, J., CHANG, C. W. & RYAN, R. E. 1977 The measurement and prediction of the melt velocities in a turbulent, electromagnetically driven recirculating low melting alloy system. *Metall. Mater. Trans. B* **8**, 333–338.

TAKEDA, Y. 1987 Measurement of velocity profile of mercury flow by ultrasound Doppler shift method. *Nucl. Technol.* **79**, 120–124.

TATSUMI, T. & YOSHIMURA, T. 1990 Stability of the laminar flow in a rectangular duct. *J. Fluid Mech.* **212**, 437–449.

TEMAM, R. 1969 Sur l'approximation de la solution des équations de Navier-Stokes par la méthode des pas fractionnaires (II). *Archive for Rational Mechanics and Analysis* **33**, 377–385.

TEN CATE, S. 2009 Numerical simulations of MHD flow in the wake of a magnetic obstacle in laminar and turbulent flow regimes. PhD thesis, University of Amsterdam.

TERZIJA, N., YIN, W., GERBETH, G., STEFANI, F., TIMMEL, K., WONDRAK, T. & PEYTON, A. J. 2011 Use of electromagnetic induction tomography for monitoring liquid metal/gas flow regimes on a model of an industrial steel caster. *Meas. Sci. Technol.* **22**, 015501.

THESS, A., VOTYAKOV, E., KNAEPEN, B. & ZIKANOV, O. 2007 Theory of the Lorentz force flowmeter. *New J. Phys.* **9** (8), 299.

THESS, A., VOTYAKOV, E. & KOLESNIKOV, Y. 2006 Lorentz force velocimetry. *Phys. Rev. Lett.* **96** (16), 164501.

THOMAS, B. & CHAUDHARY, R. 2009 State of the art in electromagnetic flow control in continuous casting of steel slabs: Modeling and plant validation. In *6th International Conference on Electromagnetic Processing of Materials EPM*. Dresden.

TIMMEL, K., ECKERT, S., GERBETH, G., STEFANI, F. & WONDRAK, T. 2010 Experimental modeling of the continuous casting process of steel using low melting point metal alloys—the LIMMCAST program. *ISIJ International* **50** (8), 1134–1141.

UHLMANN, M., KAWAHARA, G. & PINELLI, A. 2010 Traveling-waves consistent with turbulence-driven secondary flow in a square duct. *Phys. Fluids* **22**.

UHLMANN, M. & NAGATA, M. 2006 Linear stability of flow in an internally heated rectangular duct. *J. Fluid Mech.* **551**, 387–404.

UHLMANN, M., PINELL, A., KAWAHARA, G. & SEKIMOTO, A. 2007 Marginally turbulent flow in a square duct. *J. Fluid Mech.* **588**, 153–162.

UHLMANN, M. & PINELLI, A. 2007 Characterisation of Marginally Turbulent Square Duct Flow. *Advances in Turbulence XI* **117**, 41–43.

VANTIEGHEM, S. 2011 Numerical simulations of quasi-static magnetohydrodynamics using an unstructured finite volume solver: development and applications. PhD thesis, Université Libre de Bruxelles.

VANTIEGHEM, S., ALBETS-CHICO, X. & KNAEPEN, B. 2009 The velocity profile of laminar MHD flows in circular conducting pipes. *Theoretical and Computational Fluid Dynamics* **23** (6), 525–533.

VASILYEV, OLEG V 1998 On the construction of high order finite difference schemes on non-uniform meshes with good conservation properties. *Center for Turbulence Research Annual Research Briefs* pp. 311–324.

VIRÉ, A. & KNAEPEN, B. 2009 On discretization errors and subgrid scale model implementations in large eddy simulations. *J. Comp. Phys.* **228** (22), 8203–8213.

VIRÉ, A., KRASNOV, D., BOECK, T. & KNAEPEN, B. 2011 Modeling and discretization errors in large eddy simulations of hydrodynamic and magnetohydrodynamic channel flows. *J. Comp. Phys.* **230**, 1903–1922.

VOTYAKOV, E., KOLESNIKOV, Y., ANDREEV, O., ZIENICKE, E. & THESS, A. 2007 Structure of the wake of a magnetic obstacle. *Phys. Rev. Lett.* **98**, 144504.

VOTYAKOV, E. & THESS, A. 2012 Interaction of a magnetic dipole with a slowly moving electrically conducting plate. *J. Engin. Math.* Online first.

VOTYAKOV, E., ZIENICKE, E. & KOLESNIKOV, Y. 2008 Constrained flow around a magnetic obstacle. *J. Fluid Mech.* **610**, 131–156.

WALKER, J. S., LUDFORD, G. S. S. & HUNT, J. C. R. 1972 Three-dimensional MHD duct flows with strong transverse magnetic fields. Part 3. Variable-area rectangular ducts with insulating walls. *J. Fluid Mech.* **56** (1), 121–141.

WALKER, J. S. & PICOLOGLOU, B. F. 1995 Liquid-metal flow in an insulated rectangular expansion with a strong transverse magnetic field. *J. Fluid Mech.* **309**, 111–126.

WEDIN, H., BIAU, D., BOTTARO, A. & NAGATA, M. 2008 Coherent flow states in a square duct. *Phys. Fluids* **20** (9), 1–12.

WEGFRASS, A. 2012 Experimentelle Untersuchungen zur Anwendbarkeit der Lorentzkraft-Anemometrie auf schwach leitfähige Fluide. PhD thesis, Technische Universität Ilmenau.

WEGFRASS, A., DIETHOLD, C., WERNER, M., RESAGK, C., FRÖHLICH, T., HALBEDEL, B. & THESS, A. 2012 Flow rate measurement od weakly conducting fuids using lorentz force velocimetry. *Meas. Sci. Technol.* **23**, 105307.

WIDLUND, OLA 2000 Modelling of magnetohydrodynamic turbulence. PhD thesis, Royal Institute of Technology Stockholm.

WILLIAMSON, C. K. H. 1996 Vortex dynamics in the cylinder wake. *Annu. Rev. Fluid Mech.* **28**, 477–539.

WOLLASTON, C. 1881 Tidally induced emf's in cables. *J. Soc. Tel. Engrs.* **10**, 50.

ZHANG, L. & THOMAS, B. G. 2003 State of the art in evaluation and control of steel cleanliness. *ISIJ International* **43** (3), 271–291.

Acknowledgments

I am deeply indebted to Thomas Boeck who patiently assisted me and provided me with scientific guidance during my PhD. His help and support was indispensable. He never hesitated to take the time to explain me the physical side of the computational modelling and shared his passion of this discipline with me.

I would like to express my perfect appreciation to Jörg Schumacher, who helped, supported, and guided me through the course of my PhD study. The door to his office was always open for me to come and ask any questions. His contributions were instrumental in my finishing this thesis.

I wish to extend my thanks to André Thess. His management expertise and scientific knowledge were of great benefit to me. He shared his knowledge by directing me to scientific publications which helped me in my work.

My special thanks go to Dmitry Krasnov, whose long discussions and patient explanations enriched my understanding of programming. It can be said with no exaggeration that he has introduced me into the world of scientific computing.

I owe sincere gratitude to Bernard Knaepen, who hosted me in ULB for almost two month. He and his group helped me a lot by providing a favourable working atmosphere.

I would like to thank Henning Schwanbeck for being the administrator of the TU Ilmenau. His substantial support helped me overcome numerous technical problems.

My appreciation also goes to my colleagues, Christiane Heinicke and Gautam Pulugundla, for numerous fruitful discussions and collaboration. I would also like to thank my other colleagues of mine from the Institute of Thermo- and Magnetohydrodymaics and the RTG Lorentz force and Lorentz force eddy current testing. The congenial working environment they provided helped me greatly.

Last but not least I wish to record my gratitude to Jens Tympel, Thomas Weidauer, Thomas Köllner, Fatoumata Santara, Andre Wegfraß, Gautam Pulugundla and Christiane Heinicke for the comments and suggestions they made while reading different parts of this manuscript.

I would like to address thanks to my family, in particular to my parents and my brother, for their constant support. A special thanks goes to my husband, Jens Tympel, who supported me patiently and never complained about my moods. To him I dedicate this thesis.

Erklärung

Ich versichere, dass ich die vorliegende Arbeit ohne unzulässige Hilfe Dritter und ohne Benutzung anderer als der angegebenen Hilfsmittel angefertigt habe. Die aus anderen Quellen direkt oder indirekt übernommenen Daten und Konzepte sind unter Angabe der Quelle gekennzeichnet. Bei der Auswahl und Auswertung folgenden Materials haben mir die nachstehend aufgeführten Personen in der jeweils beschriebenen Weise unentgeltlich geholfen.

1. Die fachliche Betreuung der Arbeit erfolgte durch Prof. Dr. Jörg Schumacher, Dr. habil. Thomas Boeck und Prof. Dr. André Thess.

Weitere Personen waren an der inhaltlich-materiellen Erstellung der vorliegenden Arbeit nicht beteiligt. Insbesondere habe ich hierfür nicht die entgeltliche Hilfe von Vermittlungs- bzw. Beratungsdiensten (Promotionsberater oder anderer Personen) in Anspruch genommen. Niemand hat von mir unmittelbar oder mittelbar geldwerte Leistungen für Arbeiten erhalten, die im Zusammenhang mit dem Inhalte der vorgelegten Dissertation stehen. Die Arbeit wurde bisher weder im In- noch im Ausland in gleicher oder ähnlicher Form einer Prüfungsbehörde vorgelegt.

Ich bin darauf hingewiesen worden, dass die Unrichtigkeit der vorstehenden Erklärung als Täuschungsversuch bewertet wird und gemäß § 7 Abs. 10 der Promotionsordnung den Abbruch des Promotionsverfahrens zur Folge hat.

Ilmenau, den 24.11.2012

Saskia Tympel